

Cardiff University
School of Earth and Ocean Sciences

Nanoparticulate Nickel Sulfide

By
Shanshan Huang

Thesis submitted for the Degree of Philosophiae Doctor

July 2008

UMI Number: U585143

All rights reserved

INFORMATION TO ALL USERS

The quality of this reproduction is dependent upon the quality of the copy submitted.

In the unlikely event that the author did not send a complete manuscript and there are missing pages, these will be noted. Also, if material had to be removed, a note will indicate the deletion.



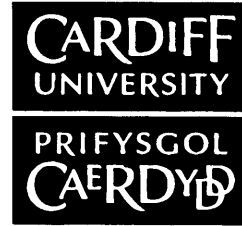
UMI U585143

Published by ProQuest LLC 2013. Copyright in the Dissertation held by the Author.
Microform Edition © ProQuest LLC.

All rights reserved. This work is protected against
unauthorized copying under Title 17, United States Code.



ProQuest LLC
789 East Eisenhower Parkway
P.O. Box 1346
Ann Arbor, MI 48106-1346



DECLARATION

This work has not previously been accepted in substance for any degree and is not concurrently submitted in candidature for any degree.

Signed *Shanshan Huang*..... (candidate) Date *24/09/08*.....

STATEMENT 1

This thesis is being submitted in partial fulfillment of the requirements for the degree of *Ph.D*.....(insert MCh, MD, MPhil, PhD etc, as appropriate)

Signed *Shanshan Huang*..... (candidate) Date *24/09/08*.....

STATEMENT 2

This thesis is the result of my own independent work/investigation, except where otherwise stated.

Other sources are acknowledged by explicit references.

Signed *Shanshan Huang*..... (candidate) Date *24/09/08*.....

STATEMENT 3

I hereby give consent for my thesis, if accepted, to be available for photocopying and for inter-library loan, and for the title and summary to be made available to outside organisations.

Signed *Shanshan Huang*..... (candidate) Date *24/09/08*.....

STATEMENT 4: PREVIOUSLY APPROVED BAR ON ACCESS

I hereby give consent for my thesis, if accepted, to be available for photocopying and for inter-library loans **after expiry of a bar on access previously approved by the Graduate Development Committee.**

Signed *Shanshan Huang*..... (candidate) Date *24/09/08*.....

Abstract

Nickel sulfide possesses a variety of typical structures and stoichiometries that distinguish itself from iron sulfide and exhibits unique roles in the prebiotic reactions which are proposed to be involved in the origin of life. Nickel sulfide precipitate is hydrated and nanocrystalline, modelled as a 4 nm sphere with a 1 nm crystalline and anhydrous NiS (millerite) core, surrounded by a hydrated and defective mantle phase. It is a metastable but fairly robust structural configuration. It may be formulated as $\text{NiS}_x\text{H}_2\text{O}$; x approximates to 1.5 and decreases on heating.

The fresh nanoparticulate nickel sulfide precipitates undergo structural transformation from the initial millerite-like NiS to the more crystalline polydymite-like Ni_3S_4 . This reaction is accompanied by the formation of a less crystalline Ni_3S_2 (heazlewoodite) phase. The reaction, happening in ambient conditions, occurs more readily for the solids precipitated from acidic environments (i.e., pH 3) and may be facilitated by the hydrogen and water bonding contained in this material.

The performance of nickel sulfide and iron sulfide precipitates is investigated in the formaldehyde world under ambient and sulfidic environments which mimic the ambient ancient Earth environments to some extent. The catalytic capacity of the metal sulfides is not obvious in these experiments. An interesting finding is that, trithiane, the cyclic $(\text{SCH}_2)_3$, also suppresses the pyrite formation and thus promotes the greigite formation in the reaction between FeS and H_2S . This provides another cause for the greigite formation in the Earth sedimentary systems and adds information to the origin-of-life theory in the iron sulfur world.

Voltammetry experiments reveal that the nickel-cysteine complex lowers the overpotential for molecular H_2 evolution in sea water to -1.53 V under ambient conditions. This catalytic property of the abiotic nickel-cysteine complex apparently mimics the Ni-S core in some hydrogenase enzymes functioning in physiological conditions. This bridges the abiotic and biotic worlds and supports the idea that life originated in the prebiotic ancient ocean.

Acknowledgements

I thank my supervisor David Rickard for his support, encouragement and care, and Anthony Oldroyd for his help and friendship. I thank Kenneth Harris who helped me out at a low point and provided generous support on my project. I appreciate the support from my pastoral supervisor Carrie Lear. My second supervisor was Simon Wakefield. The work was funded by the Dorothy Hodgkin Foundation.

I am grateful to Ian Butler for his kind help and Andrew Griffiths for technical support. George Luther and Katherine Mullaugh at the University of Delaware supervised the voltammetric work in the US. Hiroaki Ohfuji assisted with the TEM work at Ehime University, Japan. Joachim Rinna, Michael O'Reilly, Carsten Müller, David Knight, Damian Dunford, Robert Jenkins, Elisa Lopez-Capel, David Manning, David Morgan and Albert Carley helped with the GC, NMR, TGA and XPS experiments. Kind help from Zhongfu Zhou and Zhigang Pan in Prof. Harris' group and Zhongwen Yao at the University of Oxford on the solid state chemistry experiments is appreciated. I thank my friend Qi Wang at UCLA for writing a PYTHON program which enabled me to process the XRPD data.

Many thanks to my friends in Cardiff, especially Min, Siyuan and Eezhuan for sharing my joys, as well as listening to the grumbles. I value the friendship with the fellow students in the School: Sarah, Paivi, Julia, Wendy, Anna, Bryan, Alan, Martin, Cathal and Dave. They brought me much happiness outside of work. Special thanks to my flatmates at Talybont South, Miao and Xurui for teaching me to shop and cook.

Finally, I greatly thank my parents Fubin Huang and Fengzhen Ding, who went through this course with me all the time and who give me a warm home in Wuhan where I can always return.

献给我的爸爸妈妈

Contents

Abstract.....	i
Acknowledgements.....	ii
Contents.....	iv
Chapter 1 Introduction	1
1.1 Background.....	2
1.2 Project aims	5
1.3 Thesis summary.....	5
Chapter 2 Nickel Sulfide: Mineralogy and Chemistry.....	7
Figures and tables	8
Abstract.....	9
2.1 Introduction	9
2.1.1 Overview	9
2.1.2 Nickel sulfides	10
2.1.3 Nomenclature.....	13
2.2 Nickel monosulfide: millerite.....	14
2.2.1. Millerite structure	14
2.2.2 Millerite composition	14
2.2.3 Millerite formation	15
2.2.4 Electronic and other properties.....	16
2.3 NiAs-type NiS	16
2.3.1 NiAs-type NiS structure	20
2.3.2 NiAs-type NiS composition.....	21
2.3.3 NiAs-type NiS formation.....	21
2.3.4 Electronic properties.....	22
2.4 Nickel thiospinel, polydymite.....	22
2.4.1 Polydymite structure.....	22
2.4.2 Polydymite composition	23
2.4.3 Polydymite formation	23
2.5 Nickel disulfide, vaesite	24
2.5.1 Vaesite structure	24
2.5.2 Vaesite composition	24

2.5.3 Vaesite formation	24
2.5.4 Electronic properties.....	25
2.6 Heazlewoodite	25
2.6.1 Heazlewoodite structure	25
2.6.2 Heazlewoodite composition	26
2.6.3 Heazlewoodite formation	26
2.6.4 Electronic properties.....	27
2.7 Godlevskite.....	27
2.7.1 Godlevskite structure	27
2.7.2 Godlevskite composition	28
2.7.3 Godlevskite formation	28
2.8 “Amorphous NiS”.....	28
2.9 Solubility of nickel sulfides.....	30
2.10 Stability of nickel sulfides	34
2.11 Concluding remarks.....	35
Acknowledgements	36
Chapter 3 The Composition of the Nanoparticulate Nickel Sulfide	37
Figures and tables	38
Abstract.....	39
3.1 Introduction	39
3.2 Methods	41
3.2.1 Sample preparation	41
3.2.2 Ion chromatography (IC).....	41
3.2.3 Ni and S analyses.....	42
3.2.4 Inductively coupled plasma-optical emission spectrometer (ICP-OES) analysis	42
3.2.5 Energy dispersive X-ray (EDX) analyses.....	43
3.2.6 Thermogravimetric analysis (TGA)	43
3.2.7 Thermogravimetric-mass spectrometry (TGA-MS).....	43
3.2.8 Powder X-ray diffraction (XRPD) experiments.....	44
3.2.9 Analytical uncertainties	44
3.3 Results	45
3.3.1 IC analysis	45
3.3.2 Ni and S analysis	45

3.3.3 EDX analysis	46
3.3.4 TGA analysis	46
3.3.5 TGA-MS analysis	47
3.3.6 XRPD experiment.....	49
3.4 Discussion.....	49
3.5 Conclusions	52
Acknowledgements	53

Chapter 4 Structural Characterization of Nanoparticulate NiS using X-ray Scattering Techniques.....	54
Figures and tables	55
Abstract.....	56
4.1 Introduction	56
4.2 Methods	59
4.2.1 Sample preparation	59
4.2.2 Data collection	59
4.2.3 Data processing.....	60
4.2.4 Models used	60
4.3 Results	61
4.3.1 Conventional XRPD of samples at 4 days old	61
4.3.2 XRPD simulations for samples at 4 days old	63
4.3.3 Synchrotron XRPD of samples at 16 - 17 days old	65
4.3.4 Crystal growth	68
4.3.5 PDF analyses	71
4.4 Discussion.....	76
4.4.1 Phase identification and transformation	76
4.4.2 Hydrated NiS	78
4.4.3 Particle size.....	79
4.5 Conclusions	79
Appendix: XRPD Repeatability and Calibration Test.....	81
4A.1 Introduction.....	81
4A.2 Methods	81
4A.3 Results.....	82
4A.4 Conclusions.....	83
Acknowledgements	85

Chapter 5	Electron Microscopic Study of “Amorphous” Nickel Sulfide	86
	Figures and tables	87
	Abstract.....	88
	5.1 Introduction	88
	5.2 Methods	89
	5.2.1 Basics of the analytical methods	89
	5.2.2 Sample preparation	91
	5.2.3 Transmission electron microscopy (TEM)	92
	5.2.4 Scanning electron microscopy (SEM).....	92
	5.3 Results	92
	5.3.1 Particle size, shape and polydiversity.....	92
	5.3.2 Fingerprints in the HRTEM images	95
	5.3.3 Specific surface area (SSA) estimation	96
	5.3.4 SAED structural characterization	96
	5.3.5 SEM observations.....	103
	5.3.6 Chemical analyses	105
	5.4 Discussion.....	105
	5.5 Conclusions	107
	Acknowledgements	107
Chapter 6	Prebiotic Carbon Fixation by FeS/NiS in the Formaldehyde World.....	108
	Figures and tables	109
	Abstract.....	110
	6.1 Introduction	110
	6.2 Methods	114
	6.2.1 Metal sulfides preparation	114
	6.2.2 Source of other reagents used.....	115
	6.2.3 Reaction procedure	116
	6.2.4 Products characterization.....	116
	6.3 Results	117
	6.4 Discussion.....	125
	6.5 Conclusions	126
	Acknowledgements	127
Chapter 7	Catalytic Hydrogen Evolution in the Presence of Ni(II) and Cysteine in Sea Water	128

Figures and tables	129
Abstract.....	130
7.1 Introduction	130
7.2 Methods	132
7.3 Results	133
7.3.1 Basic electrochemical behavior of Ni ²⁺ and cysteine	133
7.3.2 Characteristic SWV patterns of Ni(II)-cysteine in sea water	135
7.3.3 Characteristics of the catalytic Ni and H waves	136
7.3.4 Occurrence of the catalytic waves	139
7.4 Discussion.....	140
7.5 Conclusions	143
Acknowledgements	143
Chapter 8 Discussion and Conclusions.....	144
Tables.....	145
8.1 Characterization of nanoparticulate NiS.....	146
8.1.1 Composition.....	146
8.1.2 Structure.....	147
8.1.3 Structural comparison of sulfides of Fe, Co and Ni	149
8.2 Formaldehyde world.....	151
8.2.1 H ₂ CO carbon fixation reaction	151
8.2.2 Trithiane prebiotic reaction	156
8.3 Catalytic hydrogen evolution.....	156
8.4 List of conclusions.....	157
8.5 Future work.....	158
References.....	160

Chapter 1

Introduction

1.1 Background

In the last 3 decades, knowledge has been accumulated from the evidence of the fossils that life evolved during the infant planet Earth (Schopf 1999). However, the development of the earliest metabolism that bridges the gap between the abiologic world to the biologic one remains unknown. Based on our understanding of the early geochemical Earth and biochemical pathways, theories on the emergence of life from the possible early geological environments have been proposed.

One of the first modern theories about origins of life is the Oparin-Haldane theory. Oparin suggested in 1924 that life began in an ocean under a reducing atmosphere composed of CH_4 , NH_3 , H_2 and H_2O . At one stage through the action of sunlight, these simple compounds reacted to form coacervates that grew and reproduced by fusion as a primitive metabolism (Oparin 1953). Independently, Haldane (1929) developed a similar but different theory on the origin of life that, also in the ocean under a reducing atmosphere in which CO_2 acted as the carbon source and it underwent a series of increasingly complex reactions with ultraviolet as the energy source that led to the first life forms. The idea in Oparin-Haldane theory is frequently referred to as the “prebiotic soup” in the origin-of-life discussions.

The first experimental approach to the origin of life quest was conducted by Miller (1953) supervised by Urey. They simulated the scenario in Oparin’s theory by introducing CH_4 , NH_3 , H_2 and H_2O vapour in a 5-liter flask and passed an electrical discharge. They found several types of amino acids formed within a week, as well as sugars and other organic compounds. However, their model was later questioned as to its geochemical relevance since most current models suggest a weakly reducing or neutral early Earth atmosphere. In particular, the implications of a CH_4 and NH_3 dominated atmosphere has been questioned (e.g. Levine et al. 1982). Recently, Cleaves et al. (2008) demonstrated the formation of a series of amino acids by electric discharge in a Haldane-type CO_2 , N_2 and H_2O atmosphere.

There are two problems for the organosynthesis in the “prebiotic soup”: the too dilute organics in the “soup” and the thermodynamically-unfavourable bonding for polarization (Lambert 2008). The concentration problem was demonstrated by Sillen (1965) who showed that the amino acids concentration that could be formed in the “prebiotic soup” is less than 10^{-6} M, the concentration being too low for polymeric reactions for the evolution of more

advanced living materials. The thermodynamic problem of the peptide bond formation is addressed by the fact that the ΔG°_r (Gibbs free energy of reaction) for two amino acids to form a peptide in aqueous solutions is positive, thus thermodynamically unfavoured.

To resolve the above two problems, the role of minerals, particularly clay minerals that could have been involved in prebiotic synthesis was proposed by Bernal (1949) who stated that the adsorption on mud or estuarine clay could serve to concentrate the simple organics and allow the polymerization reactions to proceed. The clay theory has been supported and developed by Cairns-Smith (1982) and Ferris (2006). Cairns-Smith (1982) developed the idea that the self-replicate clay surface could serve as the adsorbent, catalyst and the replication vehicle for the emergence of living materials. When a certain form of organic molecules were selectively trapped onto the surface of clay in an aqueous environment, it was catalysed by the surface properties of the mineral, adopted the replication fashion of the clay substrates and was finally capable of replicating independently of the “mother” clays as a result of the evolutionary process. Ferris (2006) reported that montmorillonite, a common clay present on the Earth, catalysed the formation of RNA containing monomer units from 2 to 30 - 50.

In addition to clays, other minerals that may have promoted the prebiotic reactions have received much attention. Schoonen et al. (2004) made a general review on the subject of the role of minerals on the prebiotic reactions and Lambert (2008) recently reviewed the adsorption and polymerization of amino acids on the oxide and sulfide mineral surfaces.

The current Iron-Sulfur World hypothesis, as one of the more popular, current theories about the origin of life arose following the discovery of the ecosystem surrounding the hydrothermal vents of the mid-ocean ridges in 1970s (Corliss et al. 1979) and the idea of the catalytic metabolism for the origin of life (e.g. Ycas 1955). This theory was advanced by Wächtershauser (1988a, b, 1990, 1991, 1992, 1993, 2000, 2007), modified by Russell and co-workers (1997; 1998; 2003; 2004; 2005; 2006) and has aroused much attention, reviews (Cody et al. 2004; Hatton 2007), criticisms (Deduve and Miller 1991), theoretical (Schoonen et al. 1999) and experimental (Huber and Wächtershauser 1997, 1998) analyses being published.

In the Iron Sulfur World hypothesis, it is postulated that the transition metal sulfides, especially iron, nickel and cobalt sulfides species that usually exist in the submarine

hydrothermal vents, have promoted the carbon fixation reaction which is critical for the emergence of proto-metabolism from inorganic starting materials before life emerged.

The hypothesis critically involves iron and nickel sulfides and, although iron sulfides have been characterized in some detail (e.g. Rickard and Luther 2007), the nature of the nickel sulfides precipitated in low temperature aqueous solutions is still little understood. The structure, composition and catalytic properties of nickel sulfides precipitated from low temperature aqueous solutions are the subject of this thesis.

The pioneer studies on precipitated nickel sulfides of Thiel and Gessner (1914) showed that the material is a mixture of several phases with undefined structure and they are probably hydrated. The material apparently undergoes transformation with time and the structure is subject to pH and the buffer composition in the aqueous solution. More recently, a systematic study on nickel sulfide aqueous precipitates by Jeong and Manthiram (2001) suggested that the material formed at pH 3 crystallizes with a polydymite structure and the products from higher pH environments tend to be amorphous.

A more comprehensive review on the chemistry and mineralogy of nickel sulfide is in Chapter 2 of this thesis. Following it, I show that the nickel sulfide precipitates are hydrated and closely stoichiometric by chemical analysis (Chapter 3). I demonstrate that they are not amorphous but nanocrystalline by X-ray scattering techniques (Chapter 4) and transmission electron microscopic techniques (Chapter 5).

Experimentally, within the presence of a slurry of undefined iron and nickel sulfides, all the steps for the conversion from carbon monoxide to peptide have been demonstrated, although under widely-varying conditions (Wächtershauser 2000). Some remarkable carbon fixation or reduction experiments were reported starting with carbon monoxide (Cody et al. 2000; Huber and Wächtershauser 1997, 1998) or carbon dioxide (Heinen and Lauwers 1996) as carbon sources.

Formaldehyde, a reduced form of carbon oxides, could be also a starting compound in the abiotic organosynthetic reactions. Formaldehyde have been formed naturally in the prebiotic Hadean atmosphere (Pinto et al. 1980). It interacts with iron sulfide to suppress the formation of pyrite in the presence of hydrogen sulfide (Rickard et al. 2001). In addition, formaldehyde is a pre-requisite for Strecker synthesis of amino acids and undergoes condensation in

calcium hydroxide suspensions at strong alkaline condition (Zubay 2000, p 211). An investigation of formaldehyde reactions with hydrogen sulfide and transition metal sulfides is reported in Chapter 6.

While Wachtershauser (1988a) emphasized the surface catalysis of the mineral pyrite for the proto-metabolism, the FeS membrane in Russell's model (Russell et al. 1998) would enable the homogenous catalysis inside the membrane by soluble complex reaction. Metal sulfide clusters are the intermediates of the metal sulfide mineral precipitation (Luther et al. 1999) and are abundant in natural aqueous systems (Davison et al. 1999; Rickard et al. 1999). They may have facilitated the availability of metals to early organisms. Cody et al. (2000) reported the formation of FeS-carbonyl clusters in the presence of CO at elevated temperatures. The interaction between transition metal ions and sulfur-containing compounds is of interest. The complex behaviour in the sea water media may have played a critical role in the aqueous site where life originated such as inside the Russell's FeS membrane. In Chapter 7, I report a voltammetric study of the reactions between nickel ion and cysteine.

1.2 Project aims

The aim of the PhD project is:

- 1) To characterize the nickel sulfide precipitates prepared in standard conditions at different pH's (Chapter 3, 4 and 5);
- 2) to investigate the prebiotic formaldehyde reaction with hydrogen sulfide and iron and nickel sulfides (Chapter 6) and;
- 3) to examine the nickel-cysteine system in the media of sea water (Chapter 7).

1.3 Thesis summary

Chapter 1: Introduction

Background information, project aims and thesis summary.

Chapter 2: Nickel sulfide: mineralogy and chemistry

A review on the low temperature forms of nickel sulfides about their mineralogy and chemistry with an emphasis on the properties in aqueous environments.

Chapter 3: The composition of nickel sulfide precipitates

Compositional studies on the nickel sulfide precipitate with wet chemistry methods, ICP-OES, TGA-MS, TGA, EDX and XPS techniques.

Chapter 4: Structural characterization of nanoparticulate nickel sulfides using X-ray scattering techniques

Conventional and synchrotron X-ray powder diffraction, diffraction pattern simulations and pair distribution function analysis are employed to probe the average structural features of nanoparticulate nickel sulfides.

Chapter 5: Electron microscopic study of “amorphous” nickel sulfide

High resolution transmission electron microscope imaging and selected area electron diffraction techniques are used to characterize the local structure of nickel sulfides nanoparticles.

Chapter 6: Prebiotic carbon fixation by FeS/NiS in the formaldehyde world

An investigation into the H₂CO-H₂S-Fe/NiS low temperature system to understand the role of formaldehyde in greigite formation and to see whether carbon fixation happens under these conditions.

Chapter 7: Catalytic hydrogen evolution in the presence of Ni(II) and cysteine in sea water

An exploration of the nickel-cysteine system in sea water by voltammetry.

Chapter 8: Discussion and conclusions

Discussion and conclusions of the thesis, including remarks on future work.

Chapter 2

Nickel Sulfide: Mineralogy and Chemistry

Figures

Figure 2.1 Structures of nickel sulfides.

Tables

Table 2.1 Low temperature forms of nickel sulfide phases.

Table 2.2 Syntheses of nickel sulfides from aqueous solutions.

Abstract

Nickel sulfides are of geological, environmental, physical and catalytic interests. The mineralogy and chemistry of nickel sulfides are reviewed with an emphasis on low temperature phases. These includes millerite, (hexagonal NiS), NiAs-type NiS (hexagonal Ni_{1-x}S), polydymite (cubic Ni₃S₄), vaesite (cubic NiS₂), heazlewoodite (hexagonal Ni₃S₂) and godlevskite (tetragonal Ni₉S₈). Nickel sulfides develop a range of unique structures and stoichiometries even compared to their close transition metal neighbours. This review emphasises on their behaviour associating with the aqueous environments because of its connection with the origin of life hypothesis. The solubilities of nickel sulfides are not well constrained. The nature of the aqueous precipitates of nickel sulfides has been poorly understood previously.

2.1 Introduction

2.1.1 Overview

Nickel sulfide minerals constitute important nickel ore deposits. They are usually associated with mafic and ultramafic rocks separated from silicate magmas or, precipitated in aqueous sulfidic environments. Knowledge of the nickel sulfide chemistry is essential for mining process and to meet the new technical challenge of extracting metals from low concentration of rocks.

Nickel sulfides have aroused much interest because of their novel physical and catalytic properties. For example, they are common catalysts for hydrogenation (Topsoe et al. 1996) and carbon liquefaction reactions. They are used as a storage electrode in photoelectrochemical storage devices (Licht et al. 1987). NiAs-type NiS, a phase that has not been found in nature, exhibits a novel change from paramagnetic metal to antiferromagnetic semiconductor at 265 °C (Barthelmy et al. 1973). Environmentally, acid mine drainage (AMD) generated by weathering of sulfide minerals has engendered very much concern. In addition, nickel sulfide chemistry is used to solve the associated environmental problems, such as radioactive waste disposal (Thoenen 1999). The carcinogenic effect of nickel sulfide has been intensively investigated (Jaramillo and Sonnenfeld 1989).

Transition metal sulfur centres in metalloproteins are of great biological importance (Stiefel and Matsumoto 1996). Following the discovery of “black smokers” in the deep ocean in 1970s, a number of people hypothesised that transition metal sulfides, particularly iron, nickel and cobalt sulfides could have precipitated 4 billion years ago at the bottom of Hadean sea and were involved in the prebiotic organic reactions that led to the origins of life (e.g. Corliss et al. 1979; Russell and Hall 1997; Wächtershauser 1992). A deeper understanding of the chemistry of the metal sulfide precipitates is needed to verify the hypothesis.

So far five nickel sulfide minerals are well known. They are hexagonal millerite NiS, cubic polydymite Ni₃S₄, cubic vaesite NiS₂, hexagonal heazlewoodite Ni₃S₂, and orthorhombic godlevskite Ni₉S₈. Among them, millerite is the most common nickel sulfide mineral and it is also an ore mineral for nickel. Godlevskite is only rarely found in nature.

In addition to the minerals of nickel sulfide, synthetic phases such as NiAs-type NiS and a group of dissolved nickel sulfide complexes and clusters has been reported by several authors (Al-Farawati and van den Berg 1999; Chadwell et al. 1999; Luther et al. 1996; Zhang and Millero 1994). Aqueous nickel sulfides transport nickel in anoxic natural water systems and makes Ni accessible to organisms in such environment.

This review mainly concerns the low temperature forms of nickel sulfides. They are summarised in Table 2.1 and their structures are shown in Fig. 2.1.

2.1.2 Nickel sulfides

Nickel sulfides, as transition metal sulfides, have peculiar structures and stoichiometries. Sulfides tend to be more covalent than oxides; therefore the ionic radii are not as accurate for nickel sulfides as for oxides. On the other hand, sulfides are structurally closer to selenides and tellurides (Genin and Ibers 1998). Transition metal sulfides generally have complex structures, several polymorphs and non-stoichiometry being a common apparent attribute. It is often apparent, since natural minerals commonly contain significant amounts of various transition metals, sometimes with varying oxidation numbers, which leads to an apparent deviation from stoichiometry. This is often compounded by a lack of total analyses of phases so that only metal:sulfur ratios are reported.

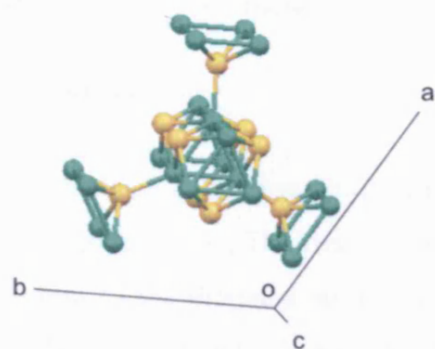
In the group of transition metal sulfides, Fe, Ni, and Co sulfides tend to be dissimilar, each having its own special structures. Still they adopt a few common overarching structure types

such as the NiAs structure, pyrite structure and thiospinel structure. Solid solution of sulfides with the other two metals is often limited, except for thiospinel where a complete solid solution of $(\text{Fe, Ni})_3\text{S}_4$ exists (Vaughan and Craig 1985).

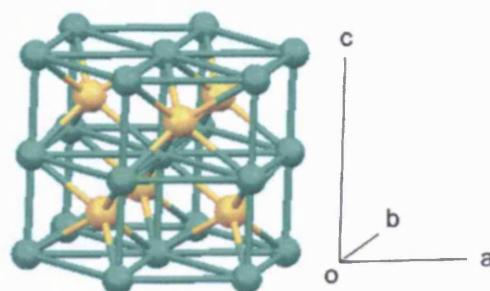
The classical coordination number of Ni in its sulfide compounds ranges from four-fold tetrahedral in heazlewoodite, to fivefold square-pyramidal in millerite and godlevskite and 6 distorted octahedral in vaesite. Some nickel sulfides, for example, heazlewoodite and millerite, are distinguished by the presence of a number of short Ni-Ni bonds (2.50 Å for heazlewoodite and 2.53 Å for millerite). These short Ni-Ni bonds are comparable to those in nickel metal (2.50 Å) (Gibbs et al. 2005) and they contribute to their special electronic properties.

Table 2.1 Low temperature forms of nickel sulfide phases

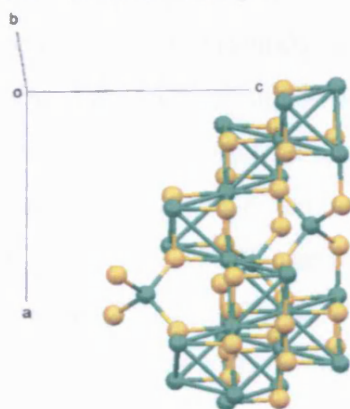
<i>Name</i>	<i>Formula</i>	<i>Structure</i>	<i>Similar structure</i>	<i>References</i>
millerite (β -NiS)	NiS	trigonal R3m	γ -NiSe	(Grice and Ferguson 1974; Rajamani and Prewitt 1974; Sowa et al. 2004)
NiAs-type (α -NiS)	NiS	hexagonal P63/mmc and P63mc	Fe_{1-x}S (pyrrhotite)	(Huang et al. 2006; McWhan et al. 1972; Sowa et al. 2004)
polydymite	Ni_3S_4	cubic Fd3m	Fe_3S_4 (greigite)	(Lundqvist 1947)
vaesite	NiS_2	cubic Pa3	FeS_2 (pyrite)	(Elliott 1960; Furuseth and Kjekshus 1969; Lundqvist 1947; Will et al. 1984)
heazlewoodite	$\text{NiS}_{1.97}$ Ni_3S_2	hexagonal R32	Ni_3SSe , Ni_3Se_2 $(\text{Ni,Co})_3\text{S}_2$	(Nowack et al. 1989) (Parise 1980)
godlevskite	Ni_9S_8	tetragonal C222	-	(Fleet 1987)



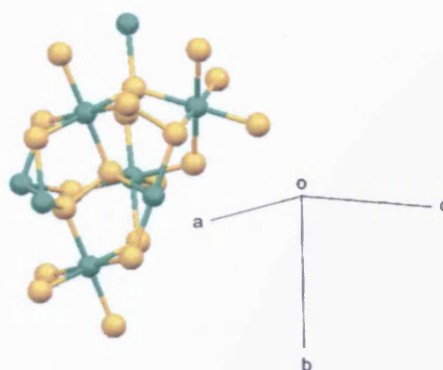
a. Millerite structure
(NiS, $R3m$, $a = 9.607$, $c = 3.143$)



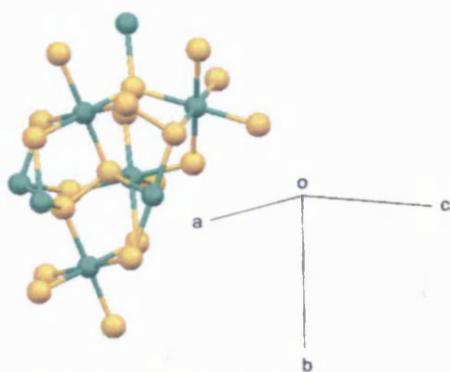
b. NiAs-type NiS structure
(NiS, $P63/mmc$, $a = 3.4395$, $c = 5.3514$)



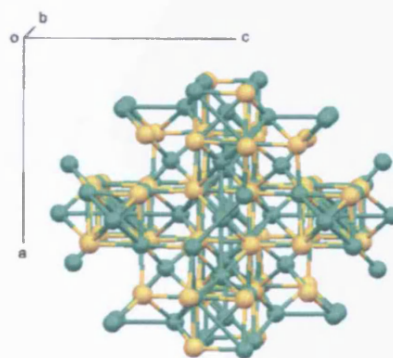
c. Polydymite structure
(Ni_3S_4 , $Fd3m$, $a = 9.457$)



d. Vaesite structure
(NiS_2 , $Pa\bar{3}$, $a = 5.69$)



e. Heazlewoodite structure
(Ni_3S_2 , $R32$, $a = 4.0718 \text{ \AA}$, $\alpha = 89.459^\circ$)



f. Godlevskite structure
(Ni_9S_8 , $C222$, $a = 9.3359$, $b = 11.2185$, $c = 9.4300$)

Figure 2.1 Structures of nickel sulfides. Green balls represent Ni atoms and yellow balls represent S atoms. The sizes of the balls are not in proportion of the real atoms. The structures are generated with MERCURY 1.4.2 (Macrae et al. 2006).

The composition of nickel sulfides vary, including a number of sulfide-rich species (such as NiS_2 , Ni_3S_4), a complex group of nickel-rich species (such as Ni_3S_2 , Ni_7S_8 , Ni_9S_8), nickel monosulfide (millerite NiS and NiAs-type NiS) and non-stoichiometric nickel sulfide (such as Ni_{1-x}S with NiAs structure).

2.1.3 Nomenclature

There has been confusion about the use of three Greek letters (α , β , and γ) as prefixes in nickel sulfide names. The first set of α , β , and γ NiS were used by Thiel and Gessner (1914) according to the different solubilities of three phases. Later characterization work showed that α - NiS , β - NiS and γ - NiS in their work correspond to nanoparticulate NiS , NiAs-type NiS and millerite-structure NiS respectively. Another set of α and β prefixes are used to designate the polymorphs of compounds stable at different temperatures. For example, α NiS is the high temperature dimorph of NiS and β NiS is the low temperature phase, millerite. Similarly α Ni_3S_2 is frequently referred to as the high temperature phase and β Ni_3S_2 as the low temperature one. However, the nomenclature of nickel sulfides in the literature varies. For example, Saito et al. (2003) used the solubility of “amorphous NiS ” determined in Dyrssen and Kremling (1990) as the solubility of millerite. Rickard and Luther (2006) designated millerite α - NiS . Fleet (1977) called the synthetic low temperature heazlewoodite, α Ni_3S_2 . Understandably, Gamsjager et al. (2005) discriminated the use of the original terms of α - NiS , β - NiS and γ - NiS in Thiel and Gessner (1914) and renamed them I- NiS , II- NiS and III- NiS instead to avoid the conflict with their use of α - NiS and β - NiS for different polymorphs. In addition, the term “amorphous NiS ” is frequently used in literature to describe the nickel sulfide materials that do not crystallize in a size large enough to generate discrete X-ray powder diffraction (XRPD) peaks (e. g. Jaramillo and Sonnenfeld 1989; Wang et al. 1997). However, under transmission electron microscopy (TEM), some if not all the “amorphous” NiS mentioned in the past literature is crystalline (Chapter 4 and 5). The reason the material appears amorphous on XRPD is caused by its nanoparticulate form.

In this thesis, I discriminate the use of the terms α - NiS , β - NiS γ - NiS and amorphous NiS . The synthetic phases of nickel sulfides are called as their equivalent mineral names or the structure such as NiAs-type NiS . I refer to the NiS materials that do not generate distinguished powder X-ray diffraction peaks as nanoparticulate NiS .

2.2 Nickel monosulfide: millerite

It is well known that nickel monosulfide exists in two forms. They are millerite, (also known as β -NiS) and its high temperature dimorph, NiAs-type NiS (also known as α -NiS). Millerite, as the low temperature form (< 652 K), is the most common nickel sulfide mineral and an ore mineral for nickel. In nature, it usually occurs as needle-like crystals with metallic lustre, (hence, also called "hair pyrite"). It is commonly associated with other important nickel-iron or copper-iron ores (Hubli et al. 1995; Legrand et al. 1998).

2.2.1. Millerite structure

The structure of millerite was first investigated by Alsen (1925) and Kolkmeijer and Moesveld (1931) (cited in Grice and Ferguson (1974)). More recently it was remeasured by Sowa et al. (2004). The generally accepted structure was characterized by Grice and Ferguson (1974) and Rajamani and Prewitt (1974). Millerite belongs to the hexagonal crystal system in space group $R\bar{3}m$ with unit cell $a = 9.607(1)\text{\AA}$ and $c = 3.143(1)\text{\AA}$ (Grice and Ferguson 1974). It has an unusual five-fold coordination of Ni atoms by S atoms forming a square pyramid NiS_5 and also a five-fold coordination of S atoms by Ni. The local structure of Ni pyramid coordination is similar to BaNiS_2 (Krishnakumar et al. 2002). The pyramids connect with three edges and form columns along $[110]$. The thus formed Ni triangles generate the shortest Ni-Ni bond of 2.53\AA . In the pyramid, the nickel atom is slightly closer to the apical sulfide atom ($\text{Ni-S} = 2.25\text{\AA}$) than those on the basal plane ($\text{Ni-S} = 2.37\text{\AA}$) (Fig. 2.1a). The S centred polyhedra, SNi_5 and the Ni centred NiS_5 polyhedra share the same motifs. It is noted that, although millerite is the most common natural nickel sulfide, no other iron or cobalt sulfide exists with a similar structure to millerite. The only other known compound with this structure type is γ -NiSe (Vuorelainen et al. 1964).

According to Kullerud and Yund (1962), Lundqvist (1947) reported a slight variation of the unit cell according to the variation of the composition of synthetic millerite. The structural parameters of the synthetic millerite agree with the values of the natural ones within 1%.

2.2.2 Millerite composition

It seems generally believed that the composition of millerite is stoichiometric (Grønvold and Stolen 1995; Wang 2005). However, only three measurements of the composition of

millerite are found in the literature. No high quality total analysis of millerite has been reported recently.

Biltz et al. (1936) examined two natural millerite crystals from mines in Pennsylvania and Westfalen (cited in Kullerud and Yund (1962)). They determined the millerite composition by differential thermal analysis and found that the sample from Pennsylvania has a stoichiometry of $\text{Ni}_{0.998}\text{S}$ and the sample from Westfalen showed a Ni deficiency of $\text{Ni}_{0.971}\text{S}_1$. Taken into account of the precision of S determination, the result of the Pennsylvania sample indicate a stoichiometric 1:1 atomic ratio, but the Westfalen sample may be Ni deficient. The problem with natural materials is that small amounts of other elements in the minerals may lead to apparent non-stoichiometry in terms of the Ni:S ratio. Lundqvist (1947) synthesized and analysed millerite and gave a small variation of less than 0.1 atomic percent variation against ideal 1:1 ratio. This suggests millerite is probably ideally stoichiometric. Lundqvist also found a slight change in unit cell according to the composition. The result of energy dispersive X-ray microanalysis (EDX) of millerite synthesized by elemental reaction shows $\text{Ni}_{1.02}\text{S}_1$, which is within the analytical error of the analysis and suggests a stoichiometric 1:1 ratio between nickel and sulfur in the synthetic millerite (Mulak et al. 2002).

2.2.3 Millerite formation

Natural millerite was discovered in 1845 in the coal field in Wales. It usually forms through low temperature alteration or produced by weathering of Ni-rich sulfides (Thoenen 1999) or hydrothermal fluids in various geodynamic settings in the ocean (Bortnikov and Vikent'ev 2005). Authigenic millerite was reported in lacustrine sediments contaminated with metals from mine-tailing ponds (Ferris et al. 1987). Some reports suggest that some natural millerites may originate from the high temperature dimorph, NiAs-type NiS (Kullerud and Yund 1962).

Levi and Baroni (1935) reported the coprecipitation of millerite with NiAs-type NiS from nickel acetate and hydrogen sulfide solutions. They also reported that adding acetic acid to fresh precipitate of nickel salt and sulfide made the material transform to a mixture of NiAs-type NiS and millerite. Millerite was also found to be the intermediate product formed during the dissolution of heazlewoodite (Mulak 1985). It was also formed during the leaching of nickel sulfide mattes with ferric chloride (Ghali and Girard 1978). Jeong and Manthiram (2001) reported the formation of millerite at pH 3 when the solid was precipitated from nickel chloride and sodium thionite solutions mixed at 1:24 molar ratio and treated with

H₂S/H₂ gas. Bezverkhyy et al. (2003) obtained millerite by treating the fresh NiS precipitate with H₂S/H₂. Zhang et al. (2007) synthesized millerite by reacting nickel metal with thiourea. Several authors reported the aqueous precipitation of millerite with microemulsion or organic solvent (Chen et al. 2002; Chen et al. 2003; Chen and Gao 2004; Khiew et al. 2004; Li et al. 2007; Meng et al. 2002; Wang et al. 2004). I report that nanocrystalline millerite is the first solid form from the precipitation of solutions of nickel salt and sulfide at mole ratio of 1:1 at pH 3 to pH 9 environments (Chapter 3, 4 and 5). See Table 2.2 for a summary of nickel sulfide synthesis in aqueous systems.

2.2.4 Electronic and other properties

Theoretical electron density distributions revealed the existence of bond path between the shortest Ni-Ni atoms. From this point of view, Ni atoms in millerite are each bonded to two S atoms and five Ni atoms for a coordination of seven. Besides the comparable Ni-Ni distance (2.53Å) in millerite with that in metallic nickel (2.49Å), the characteristics of bond critical points (bcp's) of the Ni-Ni interaction in millerite are very similar to metallic nickel. The Ni-Ni bond paths in millerite are restricted to localize in a three-membered Ni₃ in a Ni₃S₉ cluster. The conductive Ni₃ rings are not connected to the adjacent Ni₃ rings and this results in the limit of metallic conductivity of millerite (see the case of heazlewoodite below for comparison) (Gibbs et al. 2005).

Although the volume of high temperature dimorph, NiAs-type NiS is smaller than that of millerite, no phase change was observed on the single crystal millerite under pressure up to 26.8 GPa (Sowa et al. 2004).

2.3 NiAs-type NiS

NiAs-type NiS is the high temperature dimorph of nickel monosulfide. However, I synthesised it at ambient temperatures in aqueous solutions (Chapter 4). The formation of this under these conditions is analogous to the formation of the high temperature dimorph of ZnS, wurtzite, in low temperature aqueous solutions (Luther et al. 1999). In this case, the formation of the metastable phase is formed kinetically due to the structural homology of precursor aqueous ZnS clusters. NiAs-type NiS has not been found in nature but the report of Huang (Chapter 4) suggests that it is likely to occur naturally.

Table 2.2 Syntheses of nickel sulfides from aqueous solutions.

Product structure	Characteristics	Methods	References
millerite	Not specified	Precipitation of nickel salt and sulfide with acetic acid.	(Donges 1947; Levi and Baroni 1935; Thiel and Gessner 1914)
NiAs-type			
“amorphous NiS”		Precipitation of nickel salt and sulfide with uncontrolled pH.	
“amorphous NiS”	Uncharacterized NiS in 5-10 nm size	Double jet precipitation of nickel salt and Na ₂ S·9H ₂ O solutions.	(Wang et al. 1997)
vaesite	180 ± 12 nm in size	Aging the above precursor at 80°C for weeks at pH 3 - 3.5.	
polydymite	Different crystallinity depending on	Homogeneous precipitation of NiCl ₂ ·6H ₂ O and Na ₂ S ₂ O ₄ solutions at 1:16 pH 3 under ambient condition.	(Jeong and Manthiram 2001)
heazlewoodite	temperature, duration of sulfidation and	Homogeneous precipitation of NiCl ₂ ·6H ₂ O and Na ₂ S ₂ O ₄ solutions at 1:16 pH 6 under ambient condition; or at pH 8 followed by H ₂ S/H ₂ treatment.	
NiAs-type	reduction procedures	Homogeneous precipitation of NiCl ₂ ·6H ₂ O and Na ₂ S ₂ O ₄ solutions at 1:12 pH 3 under ambient condition, followed by H ₂ S/H ₂ treatment.	
millerite		Homogeneous precipitation of NiCl ₂ ·6H ₂ O and Na ₂ S ₂ O ₄ solutions at 1:24 pH 3 under ambient condition, followed by H ₂ S/H ₂ treatment.	
“amorphous NiS”		Homogeneous precipitation of NiCl ₂ ·6H ₂ O and Na ₂ S ₂ O ₄ solutions at neutral or alkaline pH ambient condition.	

millerite	4 nm crystals	Homogeneous precipitation of $\text{NiSO}_4 \cdot 6\text{H}_2\text{O}$ and $\text{Na}_2\text{S} \cdot 9\text{H}_2\text{O}$ at 1:1 molar ratio in pH 3 - 7 aqueous solutions at ambient anoxic environment.	(Chapter 4 and 5)
polydymite	100 nm crystals	Transformed from the initially precipitated millerite phase. The precipitates from pH 3 transforms to polydymite within 16 days. The materials precipitated at higher pH show less tendency towards this transformation.	
heazlewoodite	Nanoparticulate	Formed accompanying with polydymite formation under ambient conditions from the initial hydrated NiS precipitates.	
NiAs-type	>100 nm crystals	Homogeneous precipitation of $\text{NiSO}_4 \cdot 6\text{H}_2\text{O}$ and $\text{Na}_2\text{S} \cdot 9\text{H}_2\text{O}$ at 1:2 molar ratio in aqueous solutions at ambient anoxic environment.	
NiAs-type	Nanoparticulate	Aqueous precipitation of $\text{Ni}(\text{CH}_3\text{CO}_2)_2$ and H_2NCSNH_2 , sealed and stirred for 4 hours at 200 °C	(Sun 2003)
NiAs-type	Bulk crystalline	Homogeneous precipitation of $\text{Ni}(\text{NO}_3)_2 \cdot 6\text{H}_2\text{O}$ and $(\text{NH}_4)_2\text{S}$ solutions,	(Olivas et al. 1999;
Polydymite		followed by $\text{H}_2\text{S}/\text{H}_2$ treatment	Olivas et al. 1998)
α - Ni_7S_6			
heazlewoodite			
Ni_9S_8			
NiAs-type	Bulk crystalline	Homogeneous precipitation of $\text{NiSO}_4 \cdot 6\text{H}_2\text{O}$ and $\text{Na}_2\text{S} \cdot 9\text{H}_2\text{O}$, followed by	(Bezverkhyy et al. 2003)
millerite		$\text{H}_2\text{S}/\text{H}_2$ treatment	

heazlewoodite			
heazlewoodite	Nanothread-based porous and spongelike crystals	Hydrothermal treatment of Ni foil and L-cysteine	(Zhang et al. 2006)
millerrite	Rod-like or spherical nanoparticles	Solvent (hydro-) thermal reaction of $\text{NiCl}_2 \cdot 6\text{H}_2\text{O}$ and sulfur at 170 °C.	(Chen et al. 2002)
NiAs-type	5 μm long rolled layers	$\text{NiCl}_2 \cdot 6\text{H}_2\text{O}$ reaction with CS_2 in ammonia solution at 60 °C	(Jiang et al. 2001)
NiAs-type millerrite	Nanosheets and nanoneedles	Microemulsion assisted hydrothermal precipitation of $\text{Ni}(\text{NO}_3)_2 \cdot 6\text{H}_2\text{O}$ and CS_2 .	(Chen et al. 2003; Chen and Gao 2004)
millerrite	3 - 12 nm nanoparticles	Microemulsion assisted precipitation of $\text{Ni}(\text{NO}_3)_2$ and Na_2S at 37 °C	(Khiew et al. 2004)
NiAs-type	Submicrometre-sized hollow spheres	PMMA- CS_2 -ethanol-aqueous system reacts with $\text{NiSO}_4 \cdot 6\text{H}_2\text{O}$ using γ -irradiation at room temperature	(Hu et al. 2003)
NiAs-type	Single-crystal nickel sulfide nanorods	Microemulsion [(CTAB)/water/hexane/n-pentanol] assisted hydrothermal precipitation with $\text{CO}(\text{NH}_2)_2$ and CS_2 .	(Luo et al. 2007)
millerrite	3D flowerlike architectures 2 - 4 μm in size	Hydrothermal synthesis in the presence of ammonia and trisodium citrate.	(Li et al. 2007)

Conventionally, NiAs-type NiS is obtained by heating millerite to about 650 K (Wang 2005). It can be easily quenched and remains metastable under ambient conditions, which is consistent with its formation in ambient temperature aqueous solutions. It has engendered much interest because of its novel electrical properties. Under ambient conditions, NiAs-type NiS is paramagnetic metal and it changes to antiferromagnetic semiconductor at 265 °C (T_c) accompanied with a small structural change (Trahan et al. 1970). NiAs-type NiS is structurally related to troilite FeS and considered to be the Ni end member of the nickeliferous pyrrhotites, $(\text{Ni,Fe})_{1-x}\text{S}$ (Nesbitt and Reinke 1999).

2.3.1 NiAs-type NiS structure

In NiAs-type NiS, the sulfur atoms are in a hexagonal close packing and nickel atoms occupy the octahedral sites (Fig. 2.1b). Trahan et al. (1970) determined the space group $P6_3/mmc$ for the metallic phase and in $P6_3mc$ for the semiconducting phase. They gave the unit cell $a = 3.4395 \text{ \AA}$ and $c = 5.3514 \text{ \AA}$ which is consistent with the recent characterization of Sowa et al. (2004) at room temperature. Sowa et al. also reported a minor increase in a and c parameters for the material heated from 20 to 450 °C. NiAs-type NiS has smaller volume per formula unit at room temperature than millerite but no phase transition was observed for single crystal millerite up to 26.8 GPa pressure (Sowa et al. 2004).

Although in X-ray diffraction results the material is homogeneous, electron microscopic studies revealed three different structural regions in the non-stoichiometric NiAs-type NiS. They are superstructure 3a3a3c, a disordered phase (Noda et al. 1979) and superstructure 2a2a3c (Black et al. 1984). The ordered phase was proposed to be $\text{Ni}_{17}\text{S}_{18}$. Colline and Chavant (1983) refined the structure of $\text{Ni}_{17}\text{S}_{18}$ by single crystal XRD work. Lioutas et al. (1993) confirmed the existence of the two superstructures and proposed that the NiAs-type Ni_{1-x}S structure is built by the insertion of periodic stacking faults and ordering of Ni vacancies in alternate Ni layers. The 3a3a3c superstructure is stable at 1023 K and it transforms to disordered phase that contains vacancies in all nickel layers at lower temperature. The phase is briefly reviewed in Grønvold and Stolen (1995).

2.3.2 NiAs-type NiS composition

As mentioned above, NiAs-type NiS tends to be a Ni deficient phase in the range of NiS and Ni_{0.90}S. It is frequently referred to as Ni_{1-x}S or NiS_{1.03}. At high temperature (797 °C), NiAs-type NiS becomes Ni deficient with the exsolution of Ni₃S₂ or Ni₇S₆ (Kullerud and Yund 1962). Rau (1975) performed a detailed study on the homogeneity range of the Ni-deficient phase in the temperature range from 800 K to 1250 K. He found that the homogeneity range of Ni_{1-x}S is about half as large as its Fe counterpart Fe_{1-x}S. He explained that the free energy of formation of nickel vacancies is higher than that of iron vacancies in Fe_{1-x}S. Arnold and Kullerud (1956) showed that the non-stoichiometry is due to omission of nickel atoms in the structure cited in Kullerud and Yund (1962). Morozowa and Pavlinova (1972) suggested that the omission of Ni atoms may be compromised by the S-S bonds in Ni_{1-x}S phases. At low temperature, Borisenko et al. (2003) showed a linear dependence of unit cell parameters, T_c and the composition of Ni_{1-x}S in the interval ($0 \leq x \leq 0.04$).

2.3.3 NiAs-type NiS formation

A detailed study on the transition temperature of millerite ↔ NiAs-type NiS involving different stoichiometric and non-stoichiometric compounds was reported in Wang (2005). The transition temperature decreases drastically with increasing pressure (Sowa et al. 2004). Campbell and Heinz (1993) performed high pressure experiments on NiAs-type NiS at room temperature and did not observe phase transition at pressure up to 50 GPa.

Huang (Chapter 4) shows that NiAs-type NiS can be also prepared by precipitation of nickel sulfate and sodium sulfide solutions at mole ratio of 1:2 at ambient conditions in anoxic environment. A few authors obtained it by treating the fresh precipitate of nickel salt and sulfur compound solutions with H₂/H₂S (Bezverkhyy et al. 2003; Jeong and Manthiram 2001; Olivas et al. 1998), or by heating the precipitate at 80 °C for 4 hours. Some employed microemulsion or solvent assisted aqueous precipitation (Chen et al. 2003; Chen and Gao 2004; Hu et al. 2003; Zhang et al. 1999) or with ammonia solution to obtain this material (Jiang et al. 2001) (See Table 2.2).

2.3.4 Electronic properties

The core electron binding energies of millerite and NiAs-type NiS were found to be very similar according to the results of photoelectron spectra obtained in X-ray photoelectron spectra (XPS) experiments (Goh et al. 2006). They suggested that it may be due to the very similar Ni-S bonds between these two phases. However, the possibility of the reconstruction of the surface structure compared with the bulk phase cannot be ruled out. A slight difference between the two structures is shown on their near-edge X-ray absorption fine structure (NEXAFS) spectroscopy experiments.

2.4 Nickel thiospinel, polydymite

Polydymite Ni_3S_4 belongs to the group of thiospinels AB_2S_4 . It is the structural analogue of oxide spinels AB_2O_4 . It is the Ni end member of the violarites, $(\text{Fe,Ni})_3\text{S}_4$.

2.4.1 Polydymite structure

The structure of natural and synthetic polydymite has been investigated by several authors (e.g. Kesler et al. 1991; Lundqvist 1947; Menzer 1926; Vaughan and Craig 1985). The results of their studies are reasonably close and report a 0.6% variation in the unit cell size. Lundqvist (1947) measured natural and synthetic polydymites and obtained identical results with space group $\text{Fd}\bar{3}m$, $a = 9.457\text{\AA}$. The structure is based on cubic close packed sulfur atoms with half the octahedral sites and one-eighth of the tetrahedral sites occupied by nickel. The unit cell contains eight Ni_3S_4 formula units with one tetrahedral (A) site and two octahedral (B) site occupied by Ni atoms. The tetrahedral (A) site is regular but the octahedral (B) site is slightly distorted. Each sulfur atom is coordinated by three octahedral (B) nickel and one tetrahedral (A) nickel (Fig. 2.1c).

2.4.2 Polydymite composition

Polydymite is classified as a Ni end member of the linnaeite series (Co_3S_4). It appears that no total analysis of polydymite has been made since 1910. So whether the composition can vary appreciably from the stoichiometric 3:4 is unknown.

There may be a small substitution of Fe for Ni in natural mineral (An et al. 2006). Vaughan and Craig (1985) showed that complete Ni_3S_4 - FeNi_2S_4 solid solution exists below 629 K. Above this temperature, polydymite decomposes. They also showed that there is a linear increase in cell parameter in the series $\text{Ni}_3\text{S}_4 \rightarrow \text{FeNi}_2\text{S}_4$.

2.4.3 Polydymite formation

Natural polydymite, is an uncommon mineral and occurs primarily in hydrothermal vents (Vaughan and Craig 1985). The aqueous precipitates of nickel sulfides at pH 3 partly transform from the millerite structure to polydymite structure within 16 days in solid state under anoxic environments. The precipitates at higher pH also have a tendency to this transformation but at a slower rate (Chapter 4). At pH 3, Jeong and Manthiram (2001) reported the polydymite formation by mixing nickel salt and sodium dithionite solutions. Similarly, Olivas et al. (1998) reported the polydymite formation by sulfidation treatment of fresh precipitate of nickel salt and sulfide solutions (See Table 2.2). However, I think they were probably analysing the secondary phase of the precipitation product. As discussed in Chapter 4, it is unlikely on the mechanistic grounds that a mixed valence 3:4 of Ni:S salt precipitates directly from aqueous solution unless a similar moiety exists as a cluster or complex in solution. By analogy with the FeS system (Rickard and Luther 2007), the first-formed phase is likely to be a simple Ni monosulfide which converts to the more stable Ni_3S_4 .

2.5 Nickel disulfide, vaesite

2.5.1 Vaesite structure

Vaesite, NiS_2 , is the nickel analogue of pyrite FeS_2 with the space group $\text{Pa}\bar{3}$ which is related to the NaCl structure. The unit cell is c. $a = 5.69\text{\AA}$ according to several authors with natural and synthetic vaesite samples (Elliott 1960; Furuseth and Kjekshus 1969; Lundqvist 1947; Will et al. 1984). As the other members in this group, the structure of the mineral is characterised by its covalent S-S bond. Ni atoms occupy the Na sites and the S_2 pairs are at Cl sites. The axis of the four S_2 pairs in the unit cell are along four [001] directions. Each Ni atom is surrounded by six nearest S which form a distorted octahedron. Each S is coordinated to three Ni and one S, generating a distorted tetrahedron (Fig. 2.1d).

High pressure studies on synthetic single crystal NiS_2 revealed the pressure dependence of a dimension to be linear over the pressure up to 60 K bar in the experimental range (Fujii et al. 1987). Fujii et al. (1987) confirmed that the Ni-S bond length reduces with increasing pressure whereas the S-S length is almost constant.

2.5.2 Vaesite composition

The composition of natural vaesite was reported by Kerr (1945). One of his two analyses suggested the vaesite composition is close to NiS_2 and the other result showed more than 10% of Fe and Co impurities. This analysis using natural minerals does not demonstrate the variation possibility of nickel to sulfur ratio in vaesite. Nowack et al. (1989) reported a composition of vaesite phase as $\text{NiS}_{1.97}$ by remote X-ray diffraction analysis. However, the reliability of this method is doubtful. It is probable that pure vaesite is stoichiometric NiS_2 by analogy with pyrite.

2.5.3 Vaesite formation

Vaesite occurs as a weathering product of Ni skutterudite (cited by Thoenen 1999). Vaesite has been synthesised by heating NiS with mixture of molten sulfur (de Jong and Willems

1927). Wang (1997) found the formation of vaesite after aging the precipitate of nickel salt and sodium sulfide at pH 3 - 3.5 80 °C for a period of several weeks (See Table 2.2).

2.5.4 Electronic properties

Vaesite is an insulator at low temperature. This is explained by the low volume of Ni presence in the composition and large Ni-Ni distance of 4.02 \AA , compared with 2.53 \AA in millerite. No bond path is generated in the structure according to the calculation of theoretical electron density distributions (Gibbs et al. 2005). Nowack et al. (1991) studied the electron density distributions of synthetic vaesite. They confirmed that the metal atoms are in low spin state. In NiS_2 , all electron density features are within a sphere of radius of 0.65 around the nucleus of Ni atoms. Densities near S atoms are very low.

2.6 Heazlewoodite

Heazlewoodite is a low temperature modification of Ni_3S_2 (also referred to as $\beta \text{ Ni}_3\text{S}_2$). Above 823 K, it changes to a high temperature phase (Rosenqvist 1954). Heazlewoodite is found intergrown with magnetite, Fe_3O_4 at Heazlewood, Tasmania. It is the main nickel sulfide of nickel-copper mattes. It is an effective nickel sulfide catalyst (Kirkpatrick 1951) and a carcinogenetic substance (NTP 1996), which may be related to its non-classical stoichiometry.

2.6.1 Heazlewoodite structure

The pseudocubic hexagonal structure of heazlewoodite is in space group R32 ($a = 4.0718(6)$, $\alpha = 89.459(9)^\circ$ (Parise 1980). The structure is characterized by four short Ni-Ni bonds for each nickel atoms. Two of the Ni-Ni bonds (2.53 \AA) are perpendicular to the c axis and form a part of a Ni_3 triangle that are stacked in a rhombohedral arrangement in Ni spirals parallel to $[110]$ ($\text{Ni-Ni} = 2.50$). Ni atom is in tetrahedral coordination by S at $2 \times 2.25 \text{ \AA}$ and $2 \times 2.29 \text{ \AA}$. Three tetrahedra share an edge and, along $[001]$, each of them shares another two edges (Fig. 2.1e). Ni_3SSe , Ni_3Se_2 , $(\text{Ni,Co})_3\text{S}_2$ share the heazlewoodite structure.

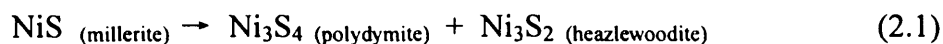
2.6.2 Heazlewoodite composition

Kullerud and Yund (1962) reported that Peacock (1947) analyzed the composition of natural heazlewoodite as $\text{Ni}_{3.04}\text{Fe}_{0.02}\text{S}_2$. It has been reported to contain 0.56 wt% Fe (Metcalf et al. 1994). Mulak (1985) synthesized heazlewoodite from elemental reaction of nickel and sulfur at 900 °C – 1100 °C and analysed the product with gravimetric determination of nickel as dimethylglyoximate and sulfur as barium sulfate. He found a composition of $\text{Ni}_{2.99}\text{S}_2$ which, considering the method, is indistinguishable from Ni_3S_2 .

The metal-rich composition of heazlewoodite, with 50 at% more Ni than S, is an extreme example of a number of metal-rich sulfides, such as the pentlandites $(\text{Ni,Fe})_9\text{S}_8$ and Co_9S_8 . Heazlewoodite is a metallic conductor with Ni-Ni bonds forming a contiguous network throughout the material (Gibbs et al. 2005). In classical terms, Gibbs et al (2005) envisaged the material as having a branching network of atomic sized Ni^0 wires permeating the structure. Sulfur atoms locate at the apices of the nickel triangles.

2.6.3 Heazlewoodite formation

Natural heazlewoodite is almost formed exclusively by serpentinization of pentlandite $(\text{Ni,Fe})_9\text{S}_8$ (Thoenen 1999). In aqueous system, heazlewoodite is reported to be formed by homogeneous precipitation of nickel salt and sodium dithionite solutions at pH 6 (Jeong and Manthiram 2001); or sulfidation of the above precipitate at pH 8 with $\text{H}_2\text{S}/\text{H}_2$ (Bezverkhyy et al. 2003; Jeong and Manthiram 2001). It can also be obtained by the hydrothermal treatment of Ni foil and L-cysteine (Zhang et al. 2006). I found that heazlewoodite is probably produced accompanying with the solid state transformation from millerite to polydymite. The reaction is



Ni_3S_2 (heazlewoodite) is detected by selected area electron diffraction experiments on the nickel sulfide precipitated at pH 3 at 241 days age (Chapter 5). In Chapter 3, I also report

that the NiS precipitate transformed to crystalline heazlewoodite structure after being heated to 700 °C (See Table 2.2).

2.6.4 Electronic properties

Heazlewoodite develops four Ni-Ni bond paths for each Ni atoms in the structure that radiate to connect all Ni atoms in a highly branched circuit of bond paths. The nature of the Ni-Ni bond in heazlewoodite is considered to be the very similar to those in metallic nickel. In nickel metal, each atom has twelve Ni-Ni bond paths radiating to other nickel atoms forming the network, whereas in heazlewoodite, the Ni-Ni coordination number is 4. This seems to explain the conductivity of heazlewoodite as one third that of nickel metal (Gibbs et al. 2005). The electronic and magnetic properties of heazlewoodite are reviewed in Metcalf et al. (1994) and Lu et al. (1996).

2.7 Godlevskite

Although there are many nickel sulfide phases existing in the sulfur range of 30 to 33 wt% such as Ni₆S₅, Ni₇S₆ and Ni₉S₈, only godlevskite is recognized as a low temperature mineral with excess Ni. The others are the high temperature solid solutions. Godlevskite is a very rare primary ore mineral that is only known in six localities.

2.7.1 Godlevskite structure

Godlevskite is orthorhombic in space group C222 ($a = 9.3359$, $b = 11.2185$, $c = 9.4300$). The structure is based on a distorted cubic close-packed 32 S atoms per unit cell, with 20 Ni atoms in tetrahedral coordination and 16 in square-pyramidal coordination. NiS₄ tetrahedrons form clusters of three-membered chains and five-membered crosses. NiS₅ square pyramids form fourfold clusters and chains (Fleet 1987) (Fig. 2.1f). The godlevskite structure is thought to be the hybrid of millerite, pentlandite and α Ni₇S₆ (Fleet 1987).

2.7.2 Godlevskite composition

Fleet (1988) analysed both mineral and synthetic godlevskite with electron microprobe at 9:8 atomic ratio and argued that the analysis excludes the possibility of Ni₇S₆ stoichiometry as suggested previously.

2.7.3 Godlevskite formation

Godlevskite is reported to be synthesized by annealing crushed product of α Ni₇S₆ at 297 °C for 49 days. α Ni₇S₆ was prepared by reacting elemental nickel and sulfur with hydrogen at 900 °C (Fleet 1988). Olivas et al. (1998) reported the formation of godlevskite together with millerite as the main product by sulfidation of fresh precipitate of nickel salt and sulfide (See Table 2.2).

2.8 “Amorphous NiS”

“Amorphous NiS” is reported to be formed by mixing nickel salts and sulfide solutions. However, Huang (Chapter 4 and 5) shows that the material is in fact crystalline and forms as nanoparticles. Selected area electron diffraction (SAED) patterns and pair distribution function (PDF) refinement suggest that the majority of the materials have a millerite structure and with decreasing pH, it tends to undergo solid state transformation to a polydymite-like material (Chapter 4) accompanied by heazlewoodite production (Chapter 5). The nanoparticulate nature of this first precipitate is responsible for the apparent “amorphous” appearance of the material in XRPD analyses. The nanoparticles cause extreme broadening of the XRP diffraction peaks.

Thiel and Gessner (1914) first reported that these precipitates consisted of three fractions. Levi and Baroni (1935) confirmed that the most soluble phase in the mixture is X-ray powder amorphous and the other two are in millerite and NiAs-type NiS structures. Likewise, Donges (1947) obtained similar results for the precipitate mixtures and confirmed that they consisted of “amorphous NiS” and NiAs-type NiS. Thiel and Gessner (1914) commented

that the “amorphous NiS” changes to the more stable phases in pure water at an extremely slow rate. They also commented that the proportion of the three polymorphs in the precipitate seemed to be balanced under different synthetic conditions. They were actually observing the crystal growth of the nanoparticles. Nicholls (1973) noted that the precipitate mixture gradually crystallized to millerite structure at low pH and to NiAs structure at high pH. Actually, NiAs-type NiS is found to be immediately produced by mixing nickel salt and sodium sulfide at pH 11.83 (Chapter 4).

Thiel and Gessner (1914) suspected that the precipitates are hydrated. According to Mellor (1936), Mickwitz found that the fresh precipitates of nickel salt and ammonia sulfide consisted of amorphous Ni(OH)(HS) or Ni(SH·OH)₂ depending on the amount of hydrogen sulfide participated in the reaction. I mixed equal molar of nickel salt and sodium sulfide solutions at pH 9 and found that (1) the atomic ratio between Ni and S is close to 1 and (2) the precipitate consists of c. 22 wt% water species. Thus the formula is proposed as NiS·xH₂O, where x approximates to 1.5 for samples aged for < 60 days at room temperature in an anoxic environment (Chapter 3).

The effect of pH on the precipitation process has not been well constrained. At pH 3 polydymite is reported to be formed from reaction of nickel chloride and sodium dithionite (Jeong and Manthiram 2001). Levi and Baroni (1935) reported that the presence of acetic acid promoted the formation of millerite and NiAs-type NiS phases. The precipitates formed at pH > 3 appear to be XRPD amorphous. Hence, it is a common practice to treat these materials with sulfidation and reduction procedures to obtain more crystalline materials (Bezverkhyy et al. 2003; Jeong and Manthiram 2001; Olivas et al. 1998). They are probably the same as the “amorphous” component described by Thiel and Gessner (1914) in their mixed precipitate from a pH-uncontrolled system. This material may represent the initial structure of the first formed nickel sulfide in ambient aqueous environment. The characterization results presented in Chapter 4 of this thesis suggest that the precipitates from pH 3 to 9 aqueous solutions initially display a millerite-like structure. The solids formed in acid conditions tend to transform to polydymite structure, accompanied by production of a less crystalline heazlewoodite phase (Chapter 4 and 5).

In the analogous aqueous FeS system, the first formed nanoparticulate material is iron (II) monosulfide with a tetragonal mackinawite structure (Rickard 1969). It transforms to the thiospinel greigite, Fe_3S_4 , through a solid state reaction facilitated by structural homology of the sulfur lattices in both phases (Lennie et al. 1997). Although in the equivalent NiS system, this structural homology is not apparent, XRPD results indicate a similar transformation for nickel sulfide precipitates from the initial millerite-like structure of the young nickel sulfide precipitates to the polydymite structure. This transformation is accompanied by the heazlewoodite formation and is possibly facilitated by the presence of water species contained in the material (Chapter 4 and 5).

2.9 Solubility of nickel sulfides

The solubilities of nickel sulfides are not well defined. In CRC Handbook of Chemistry and Physics 86th ed. (2005 - 2006), the solubility of nickel sulfide is left blank. The existing data, for example, compiled in Lange and Adolph (2005) and Smith and Martell (1976) originate from historic measurements.

Previous studies of dissolution of nickel sulfides mainly concerned in acid solutions. Thiel and Gessner (1914) reported that the three nickel sulfides in the precipitate differed each other in their solubilities in 2 N HCl. The fraction of nanoparticulate nickel sulfide phase is the most soluble and readily dissolved in cold 2 N HCl. The second soluble phase in their experiment is NiAs-type NiS, which is partially dissolved in cold 2 N HCl. The synthetic millerite is the most stable and insoluble even in hot strong acidic medium. The small particle size of the nanoparticulate NiS contributes to the enhanced solubility.

Cooper and Morse (1998) found that NiS and Ni_3S_2 (commercial products of AlfaTM) is better dissolved in concentrated HNO_3 than in 6 M HCl at room temperature. But neither of the two materials dissolved completely in concentrated HNO_3 . NiS_2 (commercial products of AlfaTM) on the other hand, dissolved completely in concentrated HNO_3 , but its dissolution in

6 M HCl is negligible. They synthesized NiS by precipitation of nickel sulfate and sodium chloride. This material was half dissolved in 1 M HCl and the remainder was completely dissolved in concentrated HNO₃ at room temperature. Unfortunately, no structural information of any of the samples is reported in the paper. Their experimental data confirmed the positive effect of particle size on the efficiency of dissolution.

Bjorling and Mulak (1976) studied the kinetics of dissolution of synthetic millerite in nitric acid and concluded that the surface reaction is the limiting factor for the dissolution process. Mulak performed a series of dissolution experiments on synthetic millerite and heazlewoodite in terms of temperature, concentration of acid, stirring speed, presence of catalytic ions. He found that dissolution of synthetic heazlewoodite is very slow in nitric acid at concentration lower than 2 M or at concentration of 3 M below temperature 50 °C. From 60 to 90 °C at 3 M nitric acid, the dissolution rate increases linearly (Mulak 1985). The presence of silver ions accelerates the dissolution (Mulak 1987b), while cupric and ferric ions do not show much catalytic effect (Mulak 1987a). Presence of potassium dichromate promotes the dissolution of millerite. The consumption of dichromate is dependent on temperature, increasing temperature and reducing pH accelerating the dissolution (Mulak 1983). The catalytic mechanisms of cupric ions on millerite dissolution were proposed (Hubli et al. 1995; Mulak et al. 2001).

My own experience showed that the precipitated nanoparticulate NiS at pH 9 was easily dissolved in 6 M HCl at about 60 °C with presence of Ti(III) citrate which served as a strong reducing agent (Zehnder and Wuhrmann 1976). The use of reducing agents, such as Ti(III) citrate, for the enhanced dissolution of FeS has been reported (Rickard and Morse 2005). The presence of the reducing agent ensures that S⁰ is not produced. Rhombic sulfur has an extensive stability field at acid pH and the addition of acid to sulfide results in the formation of this difficultly soluble material – unless the Eh is kept low. The complete reaction with oxidising acids, such as HNO₃, is consistent with this observation. This is also consistent with the observation that the solubility is very sensitive to the exposure to the air (Chapter 3). Cotton et al. (1999) suggested that exposure to air converts NiS to Ni(OH)S which is insoluble.

The nickel sulfide dissolution reaction in acid solutions can be expressed as



where

$$\log K^*_1 = \log + \log \{\text{H}_2\text{S}_{\text{aq}}\} + 2 \text{pH} \quad (2.3)$$

or



where

$$\log K^*_2 = \log \{\text{Ni}^{2+}\} + \log \{\text{HS}^-\} + \text{pH} \quad (2.5)$$

$\text{NiS}_{(s)}$ represents any solid nickel sulfide species. There is no stoichiometric constraint on it. Ni^{2+} is the hexaqua Ni^{2+} ion. $\{\}$ refers to activity.

The measurements of solubility constants of nickel sulfides have only been reported by a few authors (Berner and Zawadzki 1910; Carney and Laitinen 1970; Donges 1947; Kolthoff 1931; Thiel and Gessner 1914). The earliest attempt seems to be made by Berner and Zawadzki dated from 1910 who calculated a $\log K_{\text{SP}}$ of -23.85 from even earlier data of formation enthalpies and electrode potentials. The experimental data that is mostly cited and used for later recalculations was actually produced by Thiel and Gessner in 1914 who performed a detailed study on the solubility of freshly precipitated nickel sulfide by mixing solutions of nickel chloride and sodium sulfide. The $\log K$ values they reported for the three phases they observed are -20.5, -26.0 and -27.7. These phases correspond to nanoparticulate NiS, NiAs-type NiS and millerite respectively according to the later structural characterization by Huang (Chapter 4 and 5) and Levi and Baroni (1935). However, in Thiel and Gessner's experiments, no attempt was made to determine whether the system had approached equilibrium or not. Gamsjager et al. (2005) considered that the time allowed for the dissolution reaction was too short and the data reflected dissolution kinetics rather than thermodynamics. Hence, the solubilities obtained in this work are not reliable, neither are the numerous later calculations which simply relied on this original data (Dyrssen and Kremling 1990; Emerson et al. 1983; Huerta-Diaz et al. 1998; Jacobs and Emerson 1982; Licht 1988;

Smith and Martell 1976). Donges (1947) prepared the nanoparticulate NiS and NiAs-type NiS in the same way as Thiel and Gessner (1914). He attempted to measure the solubility of the nickel sulfide spectrophotometrically after digesting the material in 1 M HCl for 10 minutes, which seems too short for equilibrium to be approached. Again, no equilibrium check was made in his work.

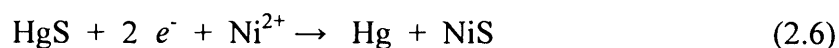
The solubilities of nickel sulfides in neutral and alkaline conditions seems to be completely neglected. To best of my knowledge, no measurement has been made. The reason is probably because the value was thought to be extremely small (Seidell 1950). This assumption is made by mistakenly neglecting the existence of nickel sulfide complexes, which is still the case in some modern literature (e.g. the Nagra Thermochemical Database) (according to Thoene (1999)). However, in this pH range, complexation of nickel sulfide is expected to dominate rather than free ions as in acidic conditions.

Thoene (1999) suggested that in alkaline conditions, the solubility of Ni sulfide is probably analogous to zinc sulfide by comparing the stability constants of metals in the Irving-Williams order ($Mn^{2+} < Fe^{2+} < Co^{2+} < Ni^{2+} < Co^{2+} < Zn^{2+}$) with a series of organic ligands. He argued that the stability constants of Ni complexes are roughly equivalent to those of Zn complexes. He showed that at pH 8.5, the complexation of zinc sulfide plays a key role in determining the solubility of sphalerite (ZnS).

In the last 15 years, a number of aqueous nickel sulfide complexes were reported, mainly by the electrochemical approach. The stability and composition of aqueous Ni sulfide complexes has been critically reviewed by Rickard and Luther (2006). The reported stability of nickel bisulfide varies between $\log K = 4.77$ to 5.3 (Al-Farawati and van den Berg 1999; Luther et al. 1996; Zhang and Millero 1994). Luther et al. (1996) also found the formation of $[Ni_2(HS)]^{3+}$ and $[Ni_3(HS)]^{5+}$ while Al-Farawati and van den Berg (1999) reported $[Ni(HS)_2]^{3+}$. In addition, Coucouvanis et al. (1985) synthesized $[Ni(S_4)_2]^{2-}$ in an organic solvent. These species are less pH dependent than the dissolution reactions of Equations (2.2) or (2.4). Obviously, the existence of the aqueous nickel sulfide complexes significantly contributes the solubility of nickel sulfides at high pH regions.

Based on the electrochemical data, the thermodynamic data of nickel sulfide is recalculated using a specific ion interaction model (Ghezlbash and Korgel 2005). However, Thoene (1999) warned that the use of thermodynamic data from electrochemical experiment for solubility calculations needs caution. He argued that in the electrochemical experiments, high concentrations of metal and ligand are needed for sufficient signal to be received. The experimental systems are strongly oversaturated and the thermodynamic data produced cannot provide a suitable estimate for the solubility.

Carney and Laitinen (1970) determined the solubility constant of NiS electrochemically by exchange reaction of



and calculated the stability constant of NiS by the ratio to HgS. The $\log K'_{s,0}$ of NiS determined in this experiment is -17.8. The morphology of the product is supposed to be amorphous which may account for the high value compared with that obtained from other methods mentioned above.

The solubilities of millerite and heazlewoodite reported as $\log K = 15.101$ and $\log K = 34.526$ respectively in Robie et al. (1978) were calculated from Rosenqvist's (1954) thermochemical data.

2.10 Stability of nickel sulfides

The significance of the current poor understanding of the solubilities of nickel sulfides is that the stabilities of nickel sulfides are consequently poorly constrained. The stability of bulk phases of nickel sulfides have been measured by heterochemical methods and is quite robust. For example, Rosenqvist (1954) did a systematic investigation on the thermochemical properties of nickel sulfides phases. His data were used in some lateral studies (e.g. Arita

2006; Waldner and Pelton 2004) on the modelling and optimization of the thermodynamic parameters of the nickel sulfide phases. Nine phases were identified at 1 bar pressure for temperatures from 25 °C to above the liquidus. They are liquid phase, high-temperature Ni_3S_2 , high-temperature Ni_{1-x}S , low temperature Ni_3S_2 , low temperature NiS , Ni_7S_6 , Ni_9S_8 , Ni_3S_4 and NiS_2 (Waldner and Pelton 2004). A review on the binary system of Ni-S is found in Gamsjager et al. (2005). However, in low temperature environment where water is probably involved, the relative stabilities between some phases are less well understood. For example, heazlewoodite is less stable with respect to millerite at 80 °C in nitric acid solution (Mulak 1985). My observations (Chapter 4 and 5) suggest that hydrated nanoparticulate NiS (millerite) is unstable with respect to heazlewoodite and polydymite at room temperature.

2.11 Concluding remarks

In this chapter, it has been demonstrated that, the low temperature species of nickel sulfides form a complicated system, crystallizing in a variety of structures and stoichiometries, which contribute to their novel physical and chemical properties. The products of nickel sulfides precipitated in aqueous environments have not previously been well constrained. Their structure, composition and transformation between phases at different pH are not well understood. Current data on the solubilities of nickel sulfides are misleading. A systemic study on the solubilities of different phases of nickel sulfides with different particle sizes and surface properties in different pH environment based on the actual solubility measurement, rather than calculations from previous thermodynamic data, is obviously urgently needed. The problem is that such work requires both careful characterizations of the solid phases as well as advanced solution chemistry.

Nickel sulfides display some peculiar structure such as millerite and heazlewoodite that do not commonly exist for other transition metal sulfides or oxides. These structures result in very short Ni-Ni and Ni-S bonds that account for its special electronic properties. The

structures of other nickel sulfides such as NiAs-type NiS, polydymite and vaesite belong to the typical structure type for transition metal chalcogenide.

The compositional studies on nickel sulfides are incomplete. Current data suggest that millerite and heazlewoodite are stoichiometric; no evidence is found that vaesite or godlevskite are non-stoichiometric; NiAs-type NiS tends to be Ni insufficient; polydymite could accommodate a substantial amount of Fe in replacement of Ni, subject to unit cell adjustment, but the pure phase is probably stoichiometric.

A number of recipes have been developed for the synthesis of nickel sulfides in aqueous environments. Sulfidising and reduction treatments of the precursor precipitates give good crystallinity of well defined products, whereas the use of solvents and microemulsion has effects on the morphological control of the products. Generally, the aqueous precipitation is advantageous to produce nanocrystalline products. However, without more detailed knowledge of the characteristics and solubilities of the nickel sulfides, synthetic routes to preparing some of these electronically very exciting materials will be limited.

Acknowledgement

I thank Martin Wolstencroft for translating parts of Thiel and Gessner (1914)'s paper (German to English) and Paula Janeiro-Barral for translating parts of Levi and Baroni (1935)'s paper (Italian to English) for me.

Chapter 3

The Composition of the Nanoparticulate Nickel Sulfide

Figures

Figure 3.1 TGA results on the NiS precipitate at 28 days age.

Figure 3.2 TGA results of the NiS precipitates at 60 days age.

Figure 3.3 DSC and MS results of 3 duplicate NiS samples.

Figure 3.4 Sulfur oxide evolution from the NiS precipitates in the TGA-MS experiment.

Table

Table 3.1 Results of Ni and S analyses of the NiS precipitates.

Abstract

The dominant nickel sulfide precipitated in normal Earth surface aqueous environments is nanoparticulate hydrated NiS with a general formula which can be represented as $\text{NiS}\cdot x\text{H}_2\text{O}$, where x is about 1.5. The atomic Ni:S ratio is close to 1. The presence of water was proven by mass spectroscopic analysis of the products on heating the precipitates and the water concentration determined by the weight loss. The average hydrated NiS nanoparticle is modelled as a 4 nm sphere with a 1 nm dehydrated crystalline NiS core and a hydrated and defective mantle phase in the outer layer. There is an average 6 at% excess of Ni over S which appears to be related to the co-precipitation of threophrastite-like $\text{Ni}(\text{OH})_2$ in the mantle layer. There are about 24 ± 3 H_2O molecules per nm^3 in the mantle layer of the nanoparticles. Thermogravimetric results suggest that the water is an integral part of the mantle layer configuration analogous to the intralayer H_2O of same clays. The composition of the material varies as a function of the particle size and the mantle:core ratio as well as pH.

Apparently this is the first reported compositional analysis of aqueous NiS precipitates since 1931. The near 1:1 atomic ratio between Ni and S is consistent with millerite-like structure of the nanoparticle core. The hydrated NiS is different from its Fe counterpart which is dehydrated. In aqueous solutions at $\text{pH} \leq 9$, nanoparticulate $\text{NiS}\cdot x\text{H}_2\text{O}$ is the first formed Ni sulfide, which subsequently undergoes transformations to more stable Ni sulfide phases. This suggests that nanoparticulate $\text{NiS}\cdot x\text{H}_2\text{O}$ determines Ni solubility in many natural systems. The chemical information of nickel sulfide precipitates is the key to the understanding of the catalytic performance of this material including its potential significance in prebiotic reactions related to the origins of life.

3.1 Introduction

Transition metal sulfides, particularly iron and nickel sulfide precipitates are of great interest because they show novel catalytic properties in a range of prebiotic carbon fixation reaction

which may have been involved in the process of the emergence of life (e.g. Cody 2004). For example, carbon monoxide has been reported to be condensed to acetic acid (Huber and Wächtershauser 1997) and peptides (Huber and Wächtershauser 1998) in the presence of iron and nickel sulfide precipitates with H_2S or CH_3SH . Currently all the steps in the prebiotic formation of proteins had been achieved synthetically with iron nickel sulfide catalysts although with varying yields and under widely varying conditions (Wächtershauser 2000).

However, the properties of the nickel sulfide precipitates are not well defined (Chapter 2). Their structures have been unclear or incompletely understood for a long time (e.g. Donges 1947; Jaramillo and Sonnenfeld 1989; Thiel and Gessner 1914; Wang et al. 1997). The chemical information of this material seems mainly to date from the studies of Thiel and Gessner in 1914 and Mickwitz in 1931. Thiel and Gessner suggested that the material might be hydrated and Mickwitz proposed the formula as $\text{Ni}(\text{OH})(\text{HS})$ or $\text{Ni}(\text{HS})_2$ according to Mellor (1936). The composition of this material is influenced by the pH of the precipitation medium (Jeong and Manthiram 2001) and the amounts of the reactants (Mellor 1936).

This chapter deals with the compositional studies of the “amorphous” nickel sulfide precipitates of Jeong and Manthiram (2001) and other workers synthesized under standard conditions in pH 9 aqueous solutions. The pH range was constrained by the observation (Chapter 4) that decreasing pH results in the increasingly enhanced formation of polydymite, Ni_3S_4 , and heazlewoodite, Ni_3S_2 . At more alkaline pH values (> 11) NiAs-type NiS begins to dominate the precipitates. However, amorphous NiS dominates in the neutral to alkaline pH range which is important in many natural systems including seawater. X-ray and HRTEM studies (Chapters 4 and 5) show that this amorphous NiS is actually nanoparticulate with a millerite-type core structure. The experiments described in this report were aimed at (1) to determine if the nickel sulfide precipitates are hydrate and (2) to determine the composition of the phase.

3.2 Methods

3.2.1 Sample preparation

For nickel sulfide precipitates, analytical grade $\text{NiSO}_4 \cdot 7\text{H}_2\text{O}$, and $\text{Na}_2\text{S} \cdot 9\text{H}_2\text{O}$ were used as starting materials in the synthetic reactions. *DD* water, that is deionised 18.2 M Ω cm (DW, MilliQ) water deoxygenated by bubbling with oxygen-free nitrogen for more than 45 minutes, was used for making solutions and washing the products. All processes involving NiS were conducted in a N_2 -filled MBraun Labmaster 130 anoxic chamber maintained at $\text{O}_2 < 2$ ppm level. 0.2 M 50 mL nickel (II) sulfate solution was dropwise added into the stirred and buffered sodium sulfide solution (0.1 M, 100 mL). Sodium sulfide solution was buffered to pH 9 with Hydrion™ phosphate buffer. The pH of the filtrate after precipitation is within 8.9 - 9.1 pH range.

According to Rickard et al. (2006), thorough washing of the sample has a significant effect on the recovery of the total chemical analysis from the metal and sulfide analyses. The washing removes other salts in the system which may be precipitated during the filtration and drying process. Rickard et al. (2006) found that co-precipitated counterions in the reactants such as sulfate can make up to 20 wt% of the total analyses of the unwashed sulfidic materials. So the nickel sulfide precipitates were washed thoroughly by re-suspending the precipitates in *DD* water and shaking for a few minutes before filtration. The washing and filtration process was repeated four times. The first and last filtration was analysed by ion chromatography to confirm that it is “clean”. The solid was collected in a round bottom bottle for freeze drying for more than 48 hours and then it was stored in the N_2 -filled anoxic chamber before analysis.

3.2.2 Ion chromatography (IC)

Ion chromatography was used to analyse the first and fourth filtrate of the precipitate during the washing procedure. The composition in the final filtrate reflect the “cleanness” of the metal sulfide solid, i.e, if there is any remnant of buffer component or the sulfate counterion

in the sample, it should show up in the filtrate. The instrument is the DIONEX DX-80 Ion Analyser with a carbonate/bicarbonate eluent.

3.2.3 Ni and S analyses

The dissolution approach developed in Rickard et al. (2006) for FeS dissolution was employed. The dissolution apparatus was assembled in the anoxic chamber. Weighed nickel sulfide precipitate (about 0.005 g) was added into the base of apparatus with 5 mL Ti(III) citrate (prepared by adding 5 mL 15% TiCl_3 to 50 mL 0.2 M sodium citrate solution buffered to pH 7 with Na_2CO_3 (Zehnder and Wuhrmann 1976)). 20 mL 6 M deoxygenated HCl (and 20 mL CrCl_3 in some cases) was added into the digestion apparatus for a reaction of 2 hours at about 60 °C. HCl solution was bubbled by N_2 gas at the rate of about 5 bubbles per second for at least 45 minutes before use. It is found that the complete deoxygenation of the HCl solution and the strict prevention of oxidation during the dissolution procedure are critical for a successful dissolution. Minor inclusion of oxygen results in the formation of black sulfur which is insoluble under these conditions. CuCl_2 solution (about 0.1 M, standardised against 0.1 M EDTA standard solution from Fisher™) was used to collect the evolved H_2S .

Sulfide is analysed by back titration of CuCl_2 with the standard 1 M EDTA, with 70 mL pH 5.5 sodium acetate trihydrate/acetic acid buffer and 0.5% aqueous solution of glycine cresol red as indicator.

3.2.4 Inductively coupled plasma-optical emission spectrometer (ICP-OES) analysis

The dissolved Ni was analysed with a JY Horiba Ultima 2 ICP-OES system. The analytical lines used were 221.65 nm, 231.60 nm and 341.48 nm. The calibration was performed by external calibration using 7 multi-element standard solutions prepared by dilution of 1000 ppm single element stock solutions. The range of standard concentrations for Ni was 0 ppm to 200 ppm. Peak intensities and concentrations were determined in triplicate for each sample solution.

3.2.5 Energy dispersive X-ray (EDX) analysis

Elemental analyses were made on Energy Dispersive X-ray experiments connected with an Oxford INCA scanning electron microscopy (SEM) and Philips transmission electron microscopy CM20 to check the elements presence on the precipitate samples.

3.2.6 Thermogravimetric analysis (TGA)

The TGA of the nickel sulfide precipitates were carried out on a Thermo Analysis Instruments SDT Q600. The furnace was heated under N₂ atmosphere. The heating temperature during the experiments steadily increased from room temperature to 400 °C for a duration of 18 minutes. The results were compared with runs on an AlfaTM 99.9% nickel sulfide specimen.

3.2.7 Thermogravimetric-mass spectrometry (TGA-MS)

The TGA-MS analyses were made on a Netzsch Simultaneous Thermal Analyzer STA 449C Jupiter equipped with a TG-DSC sample carrier (Netzsch type S), and a PtRh₁₀-Pt thermocouple. Evolved gas analysis was carried out by coupling the TG-DSC system through an adapter head in the STA 449C Jupiter gas outlet via a 200 °C heated capillary to a Netzsch Aeolos QMS 403C quadrupole mass spectrometer with m/z (mass-to-charge ratio) range 10 - 300.

Thermal analysis (TG) allows distinction of weight losses that can be associated with dehydration reactions. Differential scanning calorimetry (DSC) measures the difference in the amount of heat required to increase the temperature of a sample. It distinguishes exothermic from endothermic reactions with energy changes taking place at temperatures characteristic for specific materials. Mass spectrum (MS) measures the ion current of the mass fraction concentration. It represents the distribution of components (atoms or molecules) by mass-to-charge ratio (m/z) in a sample. The weight loss of the sample was normalised to the initial mass, and the corresponding signals were exported to the NETZSCH software for analysis as a function of temperature. The number of m/z signals selected gave a temporal resolution of 10 s corresponding to a temperature change of approximately 2 °C. In order to

compare the relative intensity of m/z peaks for different samples the signals from the QMS were normalised to the total intensity.

The sample up to 10 mg was placed in an Al_2O_3 crucible under a flow of argon to avoid oxidation from air. An empty identical reference crucible is placed on the sample holder to enable differential scanning calorimetry (DSC) measurements to be made.

Two experimental TGA-MS programmes were conducted. Programme (1) were performed on the NiS precipitates at 60 days age after precipitation with heating rate of $10\text{ }^\circ\text{C}/\text{min}$ from 30 to $700\text{ }^\circ\text{C}$, under flowing helium ($30\text{ cm}^3/\text{min}$). A reference AlfaTM 99.9% nickel sulfide was analysed on this programme. Programme (2) (also the isothermal experiment) was performed on NiS precipitates at 6 days age by heating samples at $10\text{ }^\circ\text{C}/\text{min}$, from 30 to $200\text{ }^\circ\text{C}$ under a flow of helium ($30\text{ cm}^3/\text{min}$), and remaining at $200\text{ }^\circ\text{C}$ for 2 hours. Correction runs (with empty crucible) were performed under both experimental conditions, and sample runs were corrected accordingly.

3.2.8 Powder X-ray diffraction (XRPD) experiment

XRPD experiments were carried out on a Philips PW 1710 using Cu $K\alpha$ radiation ($\lambda = 1.54056\text{ \AA}$) scanning from 5.01° to 69.99° with a scan step of 0.02° per 0.5 s.

3.2.9 Analytical uncertainties

The analytical error of Ni ion analysis by ICP-OES is below 2% (from an unpublished independent investigation on the nickel ion analysis with the instrument by the author). Rickard (2006) demonstrated that the standard deviation of sulfide analyses with the method used in this study is within 1.58%. So the absolute uncertainty in the chemical analysis of NiS, $\sigma_{(\text{NiS})}$, is given by

$$\sigma_{(\text{NiS})} = \sqrt{\sigma_{(M)}^2 + \sigma_{(S)}^2}$$

where $\sigma_{(\text{Ni})}$ is the standard deviation of the Ni analyses and $\sigma_{(S)}$ is the standard deviation of the S analyses. The calculated $\sigma_{(\text{NiS})}$ is $\pm 2.5\%$ or ± 0.025 in the mole ratio.

3.3 Results

3.3.1 IC analyses

The IC results of the first and last filtrate demonstrate that washing the sample four times effectively removed the ion impurity from the precipitation procedure. While significant amount of sulfate present in the first filtrate, the concentration dropped to a negligible value in the fourth filtrate. It confirmed that no significant concentration of any impurity ion species were present in the sample. So the samples had been sufficiently washed.

3.3.2 Ni and S analyses

Samples at each age were analysed with three duplicate analyses together with a blank run. The results are summarized in Table 3.1. The reproducibility of the analyses was within the limits of the precision of the individual analyses and the calculated standard deviation of the totals reported above.

All the precipitates were freeze-dried for more than 48 hours and looked like dry powders. However, the analytical totals average 78.6 ± 2.2 wt% which suggests c. 21 wt% water in the precipitates. Independent analyses of the precipitates with IC, ICP-OES and EDX (see below) found no substantial concentrations of any other cations or anions.

Table 3.1 Results of Ni and S analyses of the NiS precipitates. All analyses are averages of duplicates.* CrCl₃ used in the digestion (see text).

Precipitate	Age days	Ni wt%	S wt%	Total wt%	Ni:S Atomic ratio
1	4	52.3	27.3	79.6	1.06
2	5	51.1	25.3	76.4	1.11
3*	8	52.1	27.7	79.8	1.03
<i>average</i>		<i>51.8</i>	<i>26.8</i>	<i>78.6</i>	<i>1.07</i>

The analyses show no systematic trends. The totals do not change systematically with age and there is no relationship between the atomic ratios and sample age or sample total. The addition of CrCl_3 to the dissolution process does not demonstrate any difference and samples were readily dissolved with or without CrCl_3 . The Ni:S ratio shows a systematic excess of Ni over S which is greater than the precision of the analyses. The average Ni:S ratio is 1.07 and it varied in the samples between 1.03 and 1.11.

3.3.3 EDX analysis

The elemental analyses of the nickel sulfide solid with EDX showed no significant concentration of elements other than Ni, S and O. The atomic ratio of Ni and S is about 1:1, although the deviation is large due to the experimental error involved in the procedure of the analysis. The oxygen presents about 7 at% in the results of EDX connected with the Philips CM20 TEM instrument and about 29 at% in the EDX connected with the Oxford INCA SEM. There may be two reasons for the oxygen presence: (1) the samples underwent rapid oxidation on transporting to the instrument, or when the instrument column was evacuated before analysis and (2) the oxygen is from H_2O in the material.

3.3.4 TGA analysis

The TGA analyses on the nickel sulfide at 28 days age after precipitation show a total weight loss of c. 14% gradually lost from room temperature to 400 °C (Fig. 3.1). The weight loss is expected to continue if the temperature increases further after 400 °C. Comparably, the AlfaTM 99.9% nickel sulfide reference sample only showed a weight loss less than 1% under the same experimental conditions.

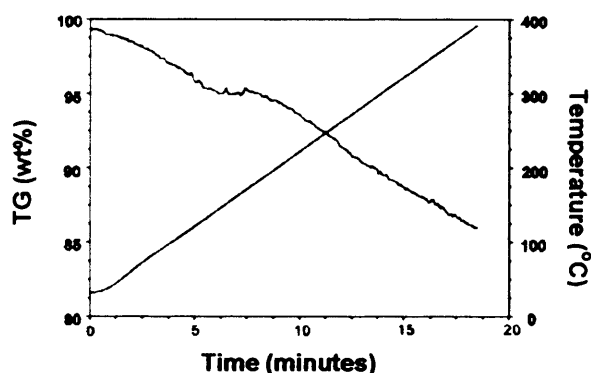


Figure 3.1 The TGA results of the NiS precipitate at 28 days old. It shows a constant decrease of mass as the temperature increased from room temperature to 400 °C. The total weight loss was about 14%.

3.3.5 TGA-MS analysis

The results of TGA-MS analysis with Programme (1) on samples at the age of 60 days show that there is a gradual weight loss from 30 to 700 °C, where the decrease levelled off. The total weight loss is about 24%, averaged from six replicate analyses. The difference of the replicate runs appears to range over 5 wt% (Fig. 3.2).

DSC and mass spectra obtained on Programme (1) are shown in Fig. 3.3

and 3.4. The vast majority of the evolved gas has m/z 18, which is assigned to water. The loss of water was principally between 200 and 400 °C and peaked at c. 375 °C (Fig. 3.3). Sulfur species with m/z 48 and 64 were produced principally at c. 500 °C (Fig. 3.4). The total weight loss enhanced at 450 °C was due to the sulfur evolution. The DSC curves suggest that as the temperature rose there was an exothermic process. At c. 600 there was a sharp endothermic reaction, which is likely to be a melting process. After an exothermic process, another endothermic reaction occurs at c. 700 °C.

The TGA-MS system was not set-up for precise chemical analyses. However, estimates of the concentration of the various species evolved can be made from the observed weight loss and the mass spectra. The sulfur species accounted for about 2 wt% of the total evolved gas and water content is around 22 wt%, which is consistent with the results of the chemical analyses. Again, only 1% weight loss was observed for the reference AlfaTM 99.9% nickel sulfide in this programme.

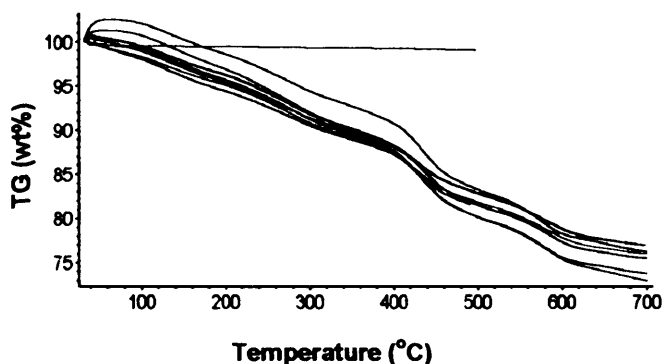


Figure 3.2 The TGA results of the NiS precipitates at 60 days age. The green line is the 99.9% NiS reference run. The others are duplicate runs on samples from one precipitate. The total weight loss was about 24% and the mass decrease levelled off at the end temperature 700 °C.

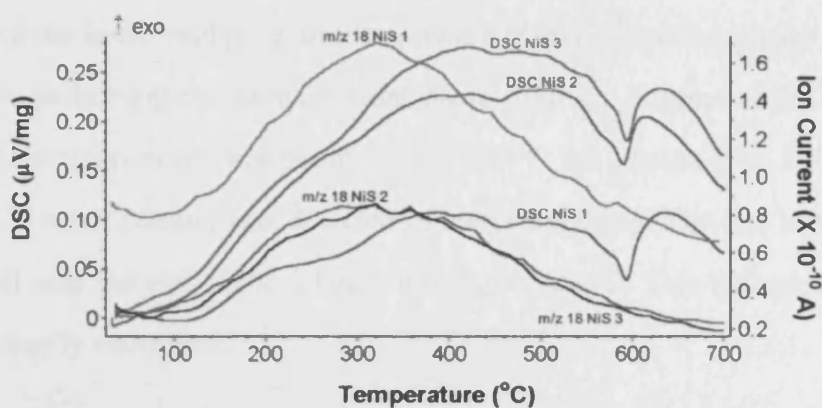


Figure 3.3 DSC and MS of 3 NiS duplicate samples plotted against temperature. DSC spectra show that under 600 °C, the reaction is the exothermic process. At c. 600 °C, a sharp endothermic reaction occurs, which is likely to be a melting process. After 700 °C, another endothermic reaction occurs. MS spectra show that water evolution peaks around 375 °C.

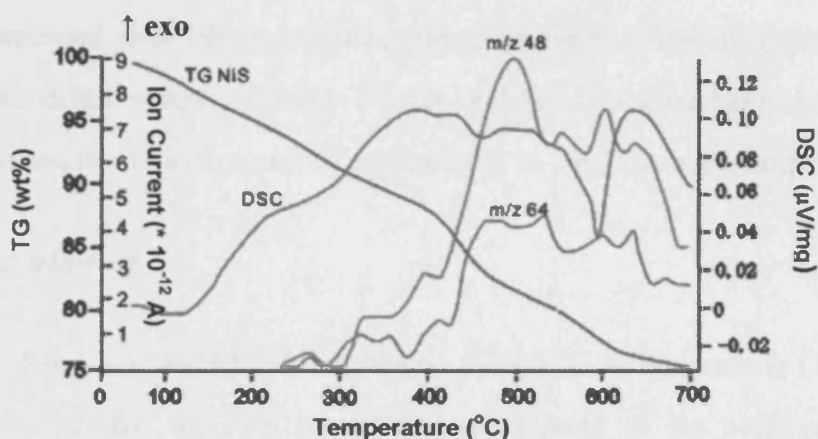


Figure 3.4 Sulfur evolution peaks around 500 °C. TG, DSC and MS spectra are plotted against temperature. m/z 48 is SO; m/z 64 is SO₂ or S₂ fraction.

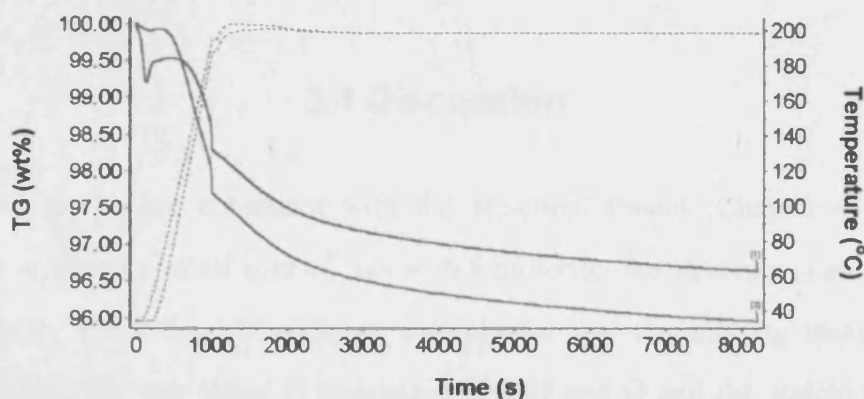


Figure 3.5 Isothermal TGA-MS experiments of two analyses ((1) and (2)) on the NiS precipitates at 6 days old. The solid lines represent mass change plotted against time. The dotted lines show the accompanying temperature. Only c. 2 wt% was lost when the sample was kept at 200 °C for 2 hours, indicating water evolution is not kinetically controlled.

The results from the isothermal programme on two NiS samples at 6 days age show a weight loss of c. 1.5% on heating the samples from 30 to 200 °C. Another c. 2% weight loss is observed when the temperature was maintained at 200 °C for 2 hours (Fig. 3.5). Only m/z 18, corresponding to water release, was detected in the evolved gas. The rate of the weight loss was levelled off near the end of the 2 hours heating at 200 °C. This indicates that the water loss is not kinetically controlled.

The results of Programme (1) of the TGA-MS experiments are consistent with the TGA results where when the sample was heated to 400 °C, the weight loss was c. 14%. The isothermal results (Programme (2)) are also consistent with the results of Programme (1) in which case when the temperature reached 200 °C, the total weight loss was about 4%. The weight loss continued after the temperature increased further. This demonstrates that, the samples at three different ages, 6 days, 28 day and 60 days after being kept in standard conditions in an anoxic environment, behave similarly in the TGA experiments.

3.3.6 XRPD experiments

XRPD results of the samples after being heated to 300 °C in Programme (1) of TGA-MS experiments showed that the NiS precipitate transformed to the well crystalline high temperature nickel monosulfide, NiAs-type NiS phase; and the product after being heated to 700 °C was in well crystalline heazlewoodite Ni₃S₂ structure.

3.4 Discussion

The analytical results are consistent with the structural model (Chapter 4) for the NiS nanoparticles in which a small core of NiS with a millerite-like structure is surrounded by a hydrated mantle. The TGA-MS analyses demonstrate that the missing mass in the total analyses is water. The m/z signal is consistent with H and O and the stoichiometry of the reaction in the closed TGA-MS system demonstrates these elements must have been evolved as H₂O during the heating cycle. The resultant water contents of c. 21 wt% from wet

chemical analysis and an estimated c. 22 wt% from the TGA-MS analyses are reasonably close within the experimental uncertainties.

The analyses were made on samples at the age of 4 - 8 days old for the wet chemical analysis and within 60 days for the TGA-MS analyses. This suggests that the change of water contents in the material during the period being kept in the anoxic chamber is not substantial. This is also supported by the similar behaviour of the materials at different ages (6 days, 28 days and 60 days after precipitation) in the TGA experiments. The hydrated NiS material can be thus represented as $\text{NiS}\cdot x\text{H}_2\text{O}$. The c. 21 wt% water in this material translates into around 1.5 water molecules per NiS and the formula may be written as $\text{NiS}\cdot 1.5\text{H}_2\text{O}$. Water is lost on heating and the value of x in this formulation decreases with temperature. XRPD results reveal that the products after being heated are in the structures of well crystalline dehydrated NiAs-type NiS and Ni_3S_2 (heazlewoodite), confirming the loss of water on the material at high temperatures.

The results of the isothermal TGA-MS experiments suggest that the loss of water on heating is not kinetically controlled. That is, heating the material for at 200 °C does not constantly increase the amount of water evolved. Together with the fact that the water content of the material remains almost unchanged during 60 days being kept in standard conditions in an anoxic environment, the water can therefore be regarded as structural water rather than merely as water adsorbed on the surface. The dehydration process of the materials indicates a fairly robust metastable configuration of this mantle phase.

The results of the chemical analyses of the material are consistent with the data from structural analyses (Chapters 4 and 5) which show that the nanoparticles display a classical core and mantle structure. The NiS core is crystalline NiS with millerite structure and about 1 nm in size. Assuming the nanoparticles are spheres with 4 nm in diameter (an average based on the HRTEM images in Chapter 5), the mantle phase is about 1.5 nm thick which contains significant amount of water. According to the water content estimated above, there are about $24 \pm 3 \text{ H}_2\text{O}$ molecules per nm^3 in the mantle layer of the nanoparticles. That is $16 \pm 2 \text{ H}_2\text{O}$ per nm^2 covering the surface of the 4 nm nanosphere of the nickel sulfide. However,

this is not surface water but they are incorporated in the 1.5 nm thickness of the material. Not surprisingly, the figure of 16 ± 2 H₂O molecules per nm² is about 6 times of the 3 H₂O molecules per nm² surface water for 3 nm ZnS spheres described in Zhang et al. (2003). The greater water content in the NiS nanoparticles is due to the different means of sample preparation. In Zhang et al. (2003), the ZnS nanoparticles were prepared in an organic solvent and water was subsequently added into the organic solvent to be adsorbed onto the surface of ZnS. However, the NiS in the present study was prepared directly from aqueous precipitation where water strongly interacted with nickel and sulfur ions in solution when they were initially bonded. The rapid crystallization during the precipitation process together with the water bonding causes considerable disorder in the mantle phase of the nanoparticles and resulted in the “amorphous” structure reported in the previous literature (Jaramillo and Sonnenfeld 1989; Thiel and Gessner 1914; Wang et al. 1997).

There is a slight excess of Ni over S in the chemical analyses. The present series of precipitates were synthesised at pH 9 in order to avoid the more rapid transformation of NiS to Ni₃S₄ and Ni₃S₂ which occurs at more acid pH and to avoid the formation of NiAs-type NiS which forms at pH 11.8. However, Ni(OH)₂ formed at pH 9 in aqueous solutions (Ramesh et al. 2006). Indeed, PDF analyses suggest small amounts of Ni(OH)₂ (theophrastite) in samples formed at pH 9 (Chapter 4). I therefore assign the small excess of Ni over S in these samples to the presence of Ni(OH)₂ in the nanoparticle mantle. The TGA-MS data indicates that any hydroxyl present in the sample is necessarily in very low concentrations. My analytical data suggests that around 7 at% of the total Ni is possibly in the form of mantle Ni(OH)₂ suggesting around 12 at% (OH)⁻ or a variation in the H₂O content within the analytical precision of the methods used.

It is interesting to note that in the analogous FeS system, no water was found in the FeS precipitates. However in the case of NiS precipitates prepared and analysed in similar conditions, the material is hydrated.

3.5 Conclusions

The nickel sulfide nanoparticles precipitated at pH 9 is formulated as $\text{NiS}\cdot x\text{H}_2\text{O}$ where x approximates to 1.5. The hydrated NiS nanoparticles support the core-mantle structural model as a 4 nm sphere with a 1 nm dehydrated crystalline NiS core and a mantle phase of 1.5 nm in thickness which is developed with combined information from structural characterization of this material. The core phase has a well-ordered millerite-like structure (Chapter 4) and is close to stoichiometric NiS. The mantle phase exhibits significant disorder and includes water. There are about 24 ± 3 H_2O molecules per nm^3 in the mantle layer of the nanoparticles. The rate of water loss slows down and levels off at 200 °C in 2 hours. No significant loss of water was found when the sample is kept in an anoxic chamber under standard conditions up to 60 days. This shows that the water is not merely adsorbed on the particle surface but is an integral part of the mantle structure. It behaves similarly to the water contained in the intralayers of some clays.

The Ni:S atomic ratio is close to 1 but Ni shows slight extra over S of about 7 at% which is balanced by hydroxyl and the formation of a threophrastite-like $\text{Ni}(\text{OH})_2$ phase in the mantle. The metastable configuration of the hydrated NiS nanoparticles is quite robust.

This hydrated nanoparticulate $\text{NiS}\cdot x\text{H}_2\text{O}$ is likely to be the dominant phase in many natural sulfidic environments in the presence of Ni, including seawater. The composition of the material varies as the nanoparticle size varies as a consequence of varying mantle:core ratios of the nanoparticles. Variations in average composition also occur with pH. At more acid pH, the Ni_3S_4 and Ni_3S_2 contents increase and this appears to be time dependent. In very alkaline conditions, threophrastite-like $\text{Ni}(\text{OH})_2$ formation increases and NiAs-structured NiS becomes the dominant phase. The results suggest, however, that $\text{NiS}\cdot x\text{H}_2\text{O}$ determines the solubility of Ni in many low temperature natural systems.

There has been considerable interest in the role of Ni sulfides as potential catalysts in prebiotic reactions involved in the origin of life. However, the Ni sulfide used in these experimental studies has not been well characterized. The results of this investigation

suggest that the dominant Ni sulfide at low temperatures in these systems is likely to be nanoparticulate hydrated $\text{NiS}\cdot x\text{H}_2\text{O}$ with a millerite-like core structure. The data on the variations of composition and structure of this material with pH and time may contribute to a better understanding of the role of Ni sulfides in this process.

Acknowledgements

The TGA experiments were carried out with assistance of Robert Jenkins in the Cardiff School of Chemistry. The TGA-MS experiments were performed by Elisa Lopez-Capel and David Manning at the University of Newcastle.

Chapter 4

Structural Characterization of Nanoparticulate NiS using X-ray Scattering Techniques

Figures

Figure 4.1 Conventional XRPD results of NiS at 4 days old.

Figure 4.2 Simulated XRPD patterns with broadened Bragg peaks.

Figure 4.3 Synchrotron XRPD patterns of 16 - 17 day old NiS precipitates.

Figure 4.4 Polydymite growth in the NiS precipitates.

Figure 4.5 The XRPD matches of polydymite and heazlewoodite against sample 3.1.

Figure 4.6 Experimental PDF patterns of the NiS precipitates at 16 or 17 days old.

Figure 4.7 PDF fits for sample 3.1.

Figure 4.8 PDF fits for sample 5.1.

Figure 4.9 PDF fits for sample 9.1.

Appendix

Figure 4A.1 Conventional XRPD pattern of 9 batch runs of the NiS precipitate.

Figure 4A.2 Smoothed conventional XRPD pattern of 9 batch runs of the NiS precipitates.

Figure 4A.3 PDF fits for sample 7.1 from all single models.

Tables

Table 4.1 Summary of the XRPD analyses.

Table 4.2 Summary of the resultant structural parameters from the PDF refinements.

Abstract

The structure of nanoparticulate NiS precipitated at pH 3.0 - 11.8 in aqueous solutions under standard temperature and pressure was characterized by conventional and synchrotron powder X-ray diffraction (XRPD) experiments, XRPD simulations and pair distribution function (PDF) technique. The results show that nickel sulfide precipitated between pH 3 and 9 develops an early millerite-like structure and it transforms to the more stable polydymite structure under standard conditions. This transformation occurs more readily for nickel sulfides formed in acid conditions. Pronounced polydymite Bragg peaks are developed in 16 days with the sample precipitated at pH 3. Evidence from XRPD data support the idea that the transformation is accompanied by Ni_3S_2 production. Nickel sulfides from neutral and acid conditions at 16 to 17 days age are a mixture of millerite and polydymite structures. Nickel sulfides formed at pH 9 consists of structural components of millerite and theophrastrite. The samples are highly defective. The coherence lengths estimated for neutral and alkaline samples are about 1 nm and it is larger for samples formed in acid conditions. Nickel sulfide precipitated at pH 11.8 possesses a NiAs structure with particle size about 18 nm. The results are useful for understanding the role of NiS involved in the novel prebiotic reactions that may have led to the origins of life.

4.1 Introduction

The study of the nanostructure of the metal sulfide precipitates is central for understanding the prebiotic reactions that may have led to the origins of life on the earth or from the cosmos (e.g. Corliss et al. 1979; Russell and Hall 1997; Wächtershauser 1992). Nickel sulfides promote some novel prebiotic reactions associated with this process (Cody et al. 2001; Huber and Wächtershauser 1997, 2006). However, the nature of the nickel sulfides involved in the reactions is unknown. The precipitates of nickel sulfides at room temperature have been traditionally considered as amorphous (Levi and Baroni 1935; Donges 1947; Jeong and Manthiram 2001; Jaramillo and Manthiram 2001). However HRTEM data clearly demonstrate that they are nanocrystalline (Chapter 5) and the structure of the nanoparticulates has not been well defined previously (cf. Chapter 2). The present study is aimed at characterizing the structure of nickel sulfide precipitates using X-ray scattering techniques.

X-ray powder diffraction (XRPD) is one of the most powerful techniques for structural study of materials. The application of synchrotron X-ray source makes high resolution and wider range of data collection possible through its high intensity and flexibility for the measurements. Simulation of X-ray diffraction patterns for comparison with the experimental ones is a common practice for crystallographers. The pair distribution function (PDF) approach has been developed for investigating structural properties of materials challenging for conventional XRD technique. Originally developed for studying liquid and amorphous materials mainly from the 1960s, the PDF technique, benefiting from the wide availability of synchrotron sources, has been developed as a powerful technique for studying disorder and nanocrystallinity (Egami and Billinge 2003).

The PDF technique uses the Fourier relationship between measured scattering intensities and the real-space arrangement of pairs of atoms. The advantage over conventional XRPD method is that it makes use of the diffuse scattering as well as the Bragg scattering. It transforms the X-ray or neutron scattering, the so-called total scattering, directly to atomic coordinates in real-space. The PDF, $G(r)$, is defined as

$$G(r) = 4\pi r[\rho(r) - \rho_0], \quad (4.1)$$

where ρ_0 is the average atomic number density, $\rho(r)$ is the atomic pair-density and r is a radial distance. The function $G(r)$ gives information on the number of atoms at a distance r from a reference atom in a spherical shell of unit thickness. It peaks at characteristic distances between pairs of atoms. It is related to the measured X-ray or neutron powder diffraction pattern through a Fourier transform

$$G(r) = (2/\pi) \int_{Q=0}^{Q_{\max}} Q[S(Q) - 1] \sin(Qr) dQ \quad (4.2)$$

where $S(Q)$ is the total scattering structure function, containing the measured intensity from an isotropic sample such as powder.

$$S(Q) = \frac{I^{\text{coh}}(Q) - \sum c_i |f_i(Q)|^2}{\left| \sum c_i f_i(Q) \right|^2} + 1 \quad (4.3)$$

where $I^{coh}(Q)$ is the measured scattering intensity from a powder sample which needs to be corrected for experimental effects such as background, multiple scattering, normalized by the flux and chemical composition of the sample, c_i and f_i are the atomic concentration and X-ray atomic form factor respectively, for the atomic species of i .

It can be seen from (4.1) to (4.3) that $G(r)$ is another representation of the scattering data. However it represents the structure in real space which is of advantage for complex structure studies. It includes information from both long-range atomic structure, manifest in the sharp Bragg peaks in the XRPD data, and the local structure, manifest in the diffuse components of the diffraction pattern.

In a PDF experiment, powder scattering data is collected ideally in a wide Q range from a synchrotron facility, due to the Debye-Waller factor and therefore, a higher real space resolution. The coherently scattered intensities need to be extracted from the raw X-ray scattering pattern by applying corrections for flux, background, Compton scattering and sample absorption. The intensities are normalized and reduced to the structure function and then Fourier transformed to PDF. Plausible structural models are looked for and their calculated PDF are compared with the experimental PDF. Finally refinement is carried out for searching and refining the most promising model. The refined parameters usually include unit cell, atom coordinates, thermal parameters crystalline sizes and instrumental parameters.

Some success has been obtained by PDF technique for elucidation of complex structure with nanostructural features. Particularly, it has successfully addressed the nanocrystalline structure of freshly precipitated FeS, the Fe counterpart of nickel sulfides in this study (Michel et al. 2005).

In this work, I apply conventional XRPD experiments, synchrotron XRPD experiments, XRPD simulations and PDF technique to characterize the structure of aqueous precipitates of nickel sulfides from various pH under ambient conditions.

4.2 Methods

4.2.1 Sample preparation

For aqueous precipitation, analytical grade $\text{NiSO}_4 \cdot 6\text{H}_2\text{O}$ and $\text{Na}_2\text{S} \cdot 9\text{H}_2\text{O}$ were used as starting materials. All reagents were made up in deionised 18.2 M Ω cm (DW, MilliQ) water, which was deoxygenated by bubbling with oxygen-free nitrogen for at least 45 minutes. All precipitation and filtration were conducted in a N_2 -filled MBraun Labmaster 130 anoxic chamber maintained at $\text{O}_2 < 2$ ppm level. Buffer solutions were used for adjusting the pH for most precipitations. pH 3 buffer was prepared by mixing potassium hydrogen phthalate and HCl. pH 5, 7 and 9 buffer powders were from Hydrion™ and are composed of acetate, phosphate and carbonate respectively. The end pH of the filtrate after the precipitation was measured. They were within the ranges of 3.0 - 4.0, 5.0 - 5.8, 7.0 - 7.3 and 8.9 - 9.1 respectively for precipitations made in pH 3, 5, 7 and 9 buffers. For pH 3.0 - 4.0 and pH 5.0 - 5.8 conditions, nickel sulfate solutions were buffered; for pH 7.0 - 7.3 and pH 8.9 - 9.1 conditions, sodium sulfide solutions were buffered. A typical precipitation was conducted by dropwise addition of one solution (0.1 M, 50 mL) into a stirred and buffered solution (0.05 M, 100 mL). Sample numbers 3.1, 5.1, 7.1 and 9.1 refer to the samples precipitated at pH 3.0 - 4.0, pH 5.0 - 5.8, pH 7.0 - 7.3 and pH 8.9 - 9.1 respectively. In addition, another precipitation was made by addition of 50 mL 0.02 M sodium sulfide into 50 mL 0.01 M nickel sulfate solution without pH adjustment. The starting material is 1:2 for Ni:S in mole ratio. The pH measured for the filtrate of the precipitation is 11.83. This sample is named sample 11.8. Products were washed, filtered and freeze dried for at least 48 hours, then ground into fine powders. Samples were stored in standard conditions in the anoxic chamber before analysis. The age of samples is calculated from precipitation (before freeze drying).

4.2.2 Data collection

Conventional laboratory XRPD experiments were carried out on a Philips PW 1710 using $\text{Cu K}\alpha$ radiation ($\lambda = 1.54056 \text{ \AA}$) scanning from 5.01° to 69.99° with a step of 0.02° per 0.5 s.

Synchrotron powder X-ray scattering data was collected at beamline BL02B2 Spring-8 Synchrotron facility, Japan. Samples were loaded into 0.5 mm capillaries. The X-ray wavelength used was 0.357 \AA . The X-ray beam was linearly polarized. An empty capillary was analyzed for background subtraction and an image plate was used as detector. It has almost no dead time for data collection. A CeO_2 standard was used for the calibration of the

incident wavelength. Measurements on the CeO₂ standard reference sample show that the Q resolution of the diffractometer is very high. This means that PDF peak broadening and exponential dampening resulting from the Q resolution of the diffractometer are negligible for the PDF region below 10 Å. The synchrotron XRPD data were tried for both Rietveld refinement and PDF analysis. All data were collected at room temperature.

4.2.3 Data processing

XRPD patterns were simulated and manipulated by MERCURY 1.4.2 (Macrae et al. 2006). GSAS (Larson and Von Dreele 2004) was used for Rietveld refinements based on the synchrotron XRPD data. However, the fits were generally very poor. The very broad diffraction peak is not sensitive enough for obtaining structural information via Rietveld refinements and this warrants the PDF analysis. For the PDF analysis, the maximum Q value used for Fourier transform was 20 Å⁻¹. Absorption correction, background subtraction, Compton scattering subtraction and corrections to ensure S(Q) oscillates around S(Q) = 1 at high Q and Fourier transform were performed with standard procedure on Wavemetric Igor in Spring-8. Structural models were refined with PDFgui (Farrow et al. 2007a). Each of the PDF refinements was computed several times until repeatable results were obtained. All the refined structures are inspected with MERCURY 1.4.2 for atomic distance check to make sure they are plausible.

4.2.4 Models used

Structural models were used in various data analyses in this study. XRPD patterns of eight phases were simulated for comparison to the conventional XRPD patterns. They include all seven nickel sulfide phases recorded in the Inorganic Crystal Structure Database (ICSD) (Fletcher et al. 1996): trigonal millerite NiS (Grice and Ferguson 1974), cubic vaesite NiS₂ (Nowack et al. 1991), cubic polydymite Ni₃S₄ (Lundqvist 1947), trigonal heazlewoodite Ni₃S₂ (Fleet 1977), NiAs-type NiS (Sowa et al. 2004), orthorhombic godlevskite Ni₉S₈ (Fleet 1987) and cubic Ni₃S₂ (Line and Huber 1963). In addition, the XRPD pattern of trigonal theophrastite β-Ni(OH)₂ (Ramesh et al. 2006) was also simulated. Ten structural models were used for refinements against PDF data of samples 3.1, 5.1, 7.1 and 9.1. These include the eight models listed above, plus two simulated phases: the Ni counterpart of the tetragonal mackinawite FeS (Lennie et al. 1995), and the Ni end-member of cubic pentlandite (Fe,Ni)₉S₈ (Rajamani and Prewitt 1975) which have not been reported as minerals or synthetic materials.

4.3 Results

4.3.1 Conventional XRPD of samples at 4 days old

Fig. 4.1 shows the XRPD patterns of samples 3.1 (Fig. 4.1a), 5.1 (Fig. 4.1b), 7.1 (Fig. 4.1c), 9.1 (Fig. 4.1d) and 11.3 (Fig. 4.1g) at 4 days old. Sample 11.8 is distinctly different from the others with a better crystallinity. The structure of this sample is readily assigned to NiAs-type NiS. Scherrer equation

$$t = \frac{K * \lambda}{B * \cos \theta_B} \quad (4.4)$$

where t = sample thickness; K = constant depends on crystallite shape (assumed value 0.89 was used); λ = X-ray wavelength; B = FWHM (full width at half max) and θ_B = Bragg angle, gives the particle size of this sample 18 nm. The rest of the investigation is focused on the structural characterization of the less crystalline samples 3.1, 5.1, 7.1 and 9.1.

Due to the lack of coherence of scattering from the very small crystallite size, the XRPD patterns of samples 3.1, 5.1, 7.1 and 9.1 share a similar fashion of two broad peaks at around 2.7 and 1.7 Å, where almost all known bulk phases of nickel sulfides have several Bragg peaks. Examining the four patterns in detail, one can spot some different features at the top of each broad peak. For instance for sample 3.1, the broad peak at $d = c. 2.7$ is split to two subpeaks at $c. d = 2.6$ and 2.9 Å. The other broad peak is a combination of two or more peaks spanning from 1.68 to 1.82 Å. There is no bulk phase of single nickel sulfide that has peaks matching all the four positions. This may indicate the mixture nature of this material. However, polydymite and heazlewoodite are the two phases that peak at three of the four positions. The matching of the two phases with sample 3.1 data is shown in Fig. 4.1e and 4.1f. It can be seen that both the two bulk phases match the majority of the very broad Braggian features in the data of sample 3.1 except for the peak at around 2.6 Å. However, the 1.8 Å peak in heazlewoodite model is slightly higher than the 1.6 Å peak while the experimental data show the opposite. Moreover, the relative intensities of the peaks at 2.9 Å and 1.7 Å of heazlewoodite are not consistent with the data of sample 3.1 either. On the other hand, polydymite display the expected relative intensities among the three major observed peaks. So polydymite is considered the best crystalline phase in sample 3.1. However, this assignment does not address the 2.6 Å peak, which might be assigned to the (410) planes of NiAs-type NiS.

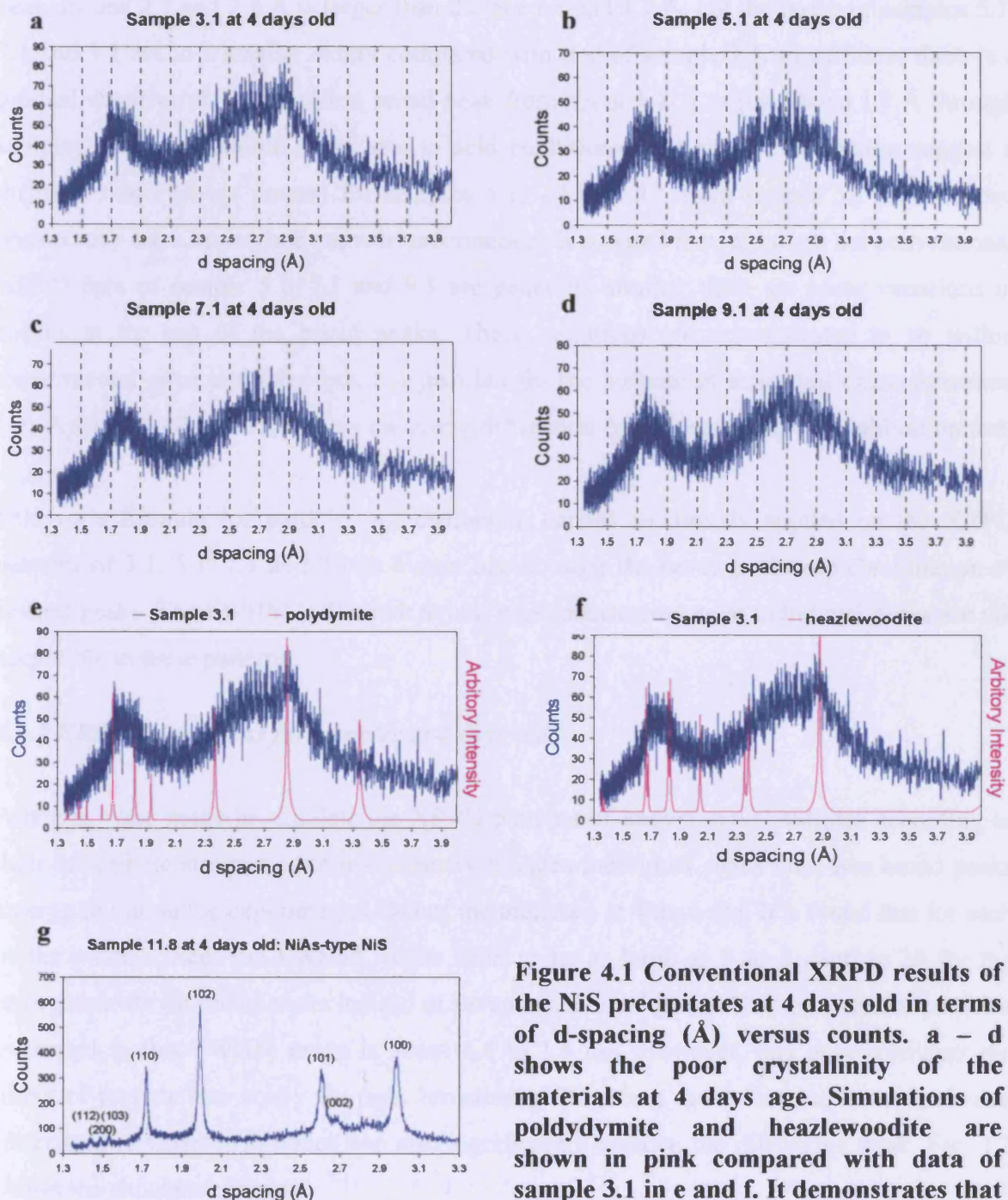


Figure 4.1 Conventional XRPD results of the NiS precipitates at 4 days old in terms of d-spacing (Å) versus counts. a – d shows the poor crystallinity of the materials at 4 days age. Simulations of polydymite and heazlewoodite are shown in pink compared with data of sample 3.1 in e and f. It demonstrates that polydymite is a relatively better candidate. f shows that sample 11.8 is well crystalline NiAs type NiS.

Except sample 3.1, data of samples 5.1, 7.1 and 9.1 have their common maxima at around 2.7 Å rather than 2.8 Å for sample 3.1. The size proportion of the two broad peaks of samples 5.1, 7.1 and 9.1 are different from that of sample 3.1. For all the four data, the broad peak around 2.7 and 2.8 Å is larger than the one around 1.7 Å, but the peaks of samples 5.1, 7.1 and 9.1 are to a smaller extent compared with that of sample 3.1. In addition, there is a gradual negative shift of the first broad peak from about 1.8 Å to just above 1.7 Å through samples made in alkaline conditions to acid conditions. The above information suggest a different major phase present for samples 5.1, 7.1 and 9.1 from sample 3.1 and the two phases may have undergone some transformation. It is noted that, although the conventional XRPD data of sample 5.1, 7.1 and 9.1 are generally similar, there are some variations in shapes at the top of the broad peaks. These variations are demonstrated to be within experimental error and therefore, not justified for the purpose of structural characterization (see Appendix 4A for a report on the X-ray diffraction data repeatability and calibration test).

Scherrer's formula for particle size estimation cannot be directly applied on the XRPD patterns of 3.1, 5.1, 7.1 and 9.1 at 4 days age because the broad peaks are combination of several peaks. The FWHM (full width at half max) measurements of individual peaks are not accessible in these patterns.

4.3.2 XRPD simulations for samples at 4 days old

Attempts were made to simulate the XRPD patterns of known nickel sulfides according to their bulk phase structures but intentionally broaden individual peaks until two broad peaks emerge to mimic the experimental data of the materials at 4 days old. It is found that for each of the models used, the FWHM values need to be as large as 5 to 8 degrees 2θ for the emergence of two broad peaks instead of several individual peaks. The thickness of particles estimated in this FWHM range is about 1.0 to 1.6 nm. However, this only considers the effect of particle size solely for peak broadening. It ignores the defect and water inclusion (discussed in Chapter 3) which can also significantly broaden the diffraction peak. Fig. 4.2 shows the simulated patterns.

Compared the simulated patterns with experimental data, the simulated XRPD pattern of polydymite with thickness of 1.2 nm defined by Scherrer's formula closely matches the experimental data of sample 3.1, especially in the area of the combined peak near $d = 1.7 - 1.8$ Å. However, the broad peak around 1.7 Å in the simulated polydymite XRPD pattern is too small relative to the peak around 2.8 Å in comparison with the two corresponding peaks

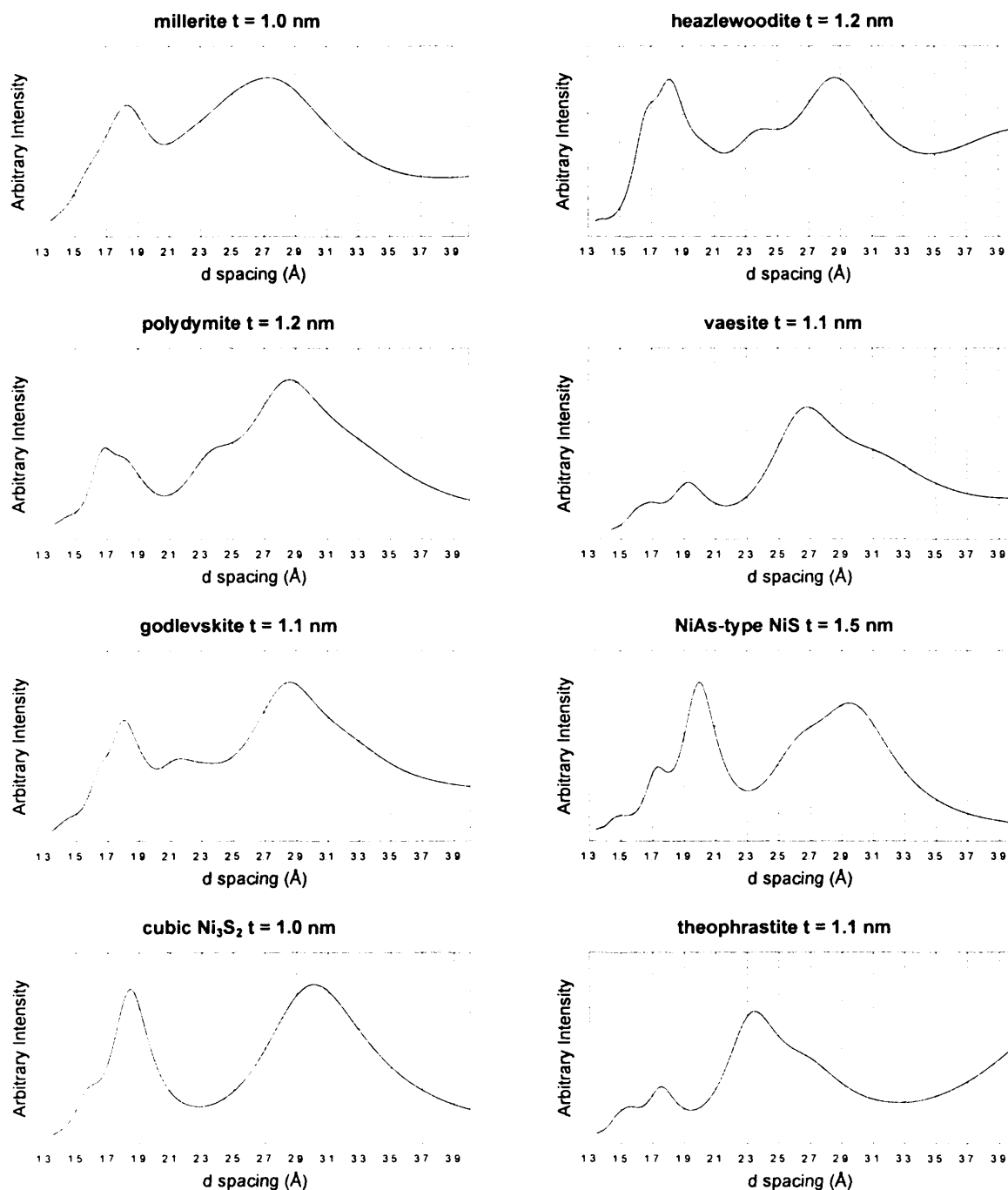


Figure 4.2 Simulated XRPD patterns with broadened Bragg peaks (by MERCURY 1.4.2) for nickel sulfides and hydroxide phases in terms of d-spacing (Å) versus arbitrary intensities. Compared with experimental data in Fig. 4.1, it shows that simulated polydymite gives the closest shape at c. 1.70 Å but only simulated millerite gives the consistent proportion of peak sizes to the experimental data.

in the data of sample 3.1. This can be explained by the coexistence of another phase of smaller particle size in addition to polydymite in this sample – the other phase contributes to the intensities of the broad peaks in sample 3.1. From Fig. 4.2, millerite, heazlewoodite and NiAs-type NiS have relatively larger peaks at the smaller d-spacing position, which may contribute to the intensities as a less crystalline material underneath the more crystalline polydymite peaks and thus balance the peak size proportion in the data of sample 3.1.

The other three samples 5.1, 7.1 and 9.1 have common maximum at about 2.7 Å and share a similar pattern of the two broad peaks. Among the 8 simulated models, millerite gives the pattern closest to the experimental data in terms of the position of the major peak at 2.7 Å and the size proportion of the two broad peaks. However, it is also noted that, the minor millerite peak around 1.7 Å is about 0.04 Å more positive compared with the experimental data of samples 5.1, 7.1 and 9.1. It appears to be an end member of the transformation series with the position of the minor peak shifting starting from 1.82 Å for millerite to 1.78 Å for sample 9.1 (Fig. 1d), 1.75 Å for sample 7.1 (Fig. 1c) and 1.72 Å for sample 5.1 (Fig. 1b) and 3.1 (Fig. 1a), or one seems to observe a peak growth at around 1.7 Å from sample 9.1 to sample 3.1. However, this assumption needs approving. Other simulated patterns such as godlevskite, cubic Ni₃S₂, and theophrastite have peaks fitting into this area, although they do not have the correct peaks sizes.

4.3.3 Synchrotron XRPD of samples at 16 - 17 days old

Fig. 4.3a - d are the individual XRPD pattern obtained from synchrotron X-ray radiation source on samples 3.1, 5.1, 7.1 and 9.1 aged for 16 or 17 days. They are plotted together in Fig. 4.3e for comparison. Apart from the better resolution given by the synchrotron X-ray radiation source, significant crystal growth is observed for sample 3.1, as well as sample 5.1 but to a less extent. The peaks on top of the sample 3.1 pattern are confidently indexed to the polydymite structure. These peaks are non-uniformly broadened. The narrowest peak is reflected by the (440) planes from which the particle thickness is estimated as 70 nm via Scherrer equation while the reflection from (311) planes suggests a particle size of 40 nm. All the Bragg peaks are broadened to different extents. This may be due to a particular shape of the formed polydymite nanocrystals in this material. It can be clearly seen from the sample 3.1 pattern that sharper peaks are on top of a broad background, indicating that apart from the crystalline polydymite, the material consists of another phase in a less crystalline state. The identity of this nanocrystalline material cannot be directly identified from the broad background. The pattern of sample 5.1 is similar but the Bragg peaks on the top are

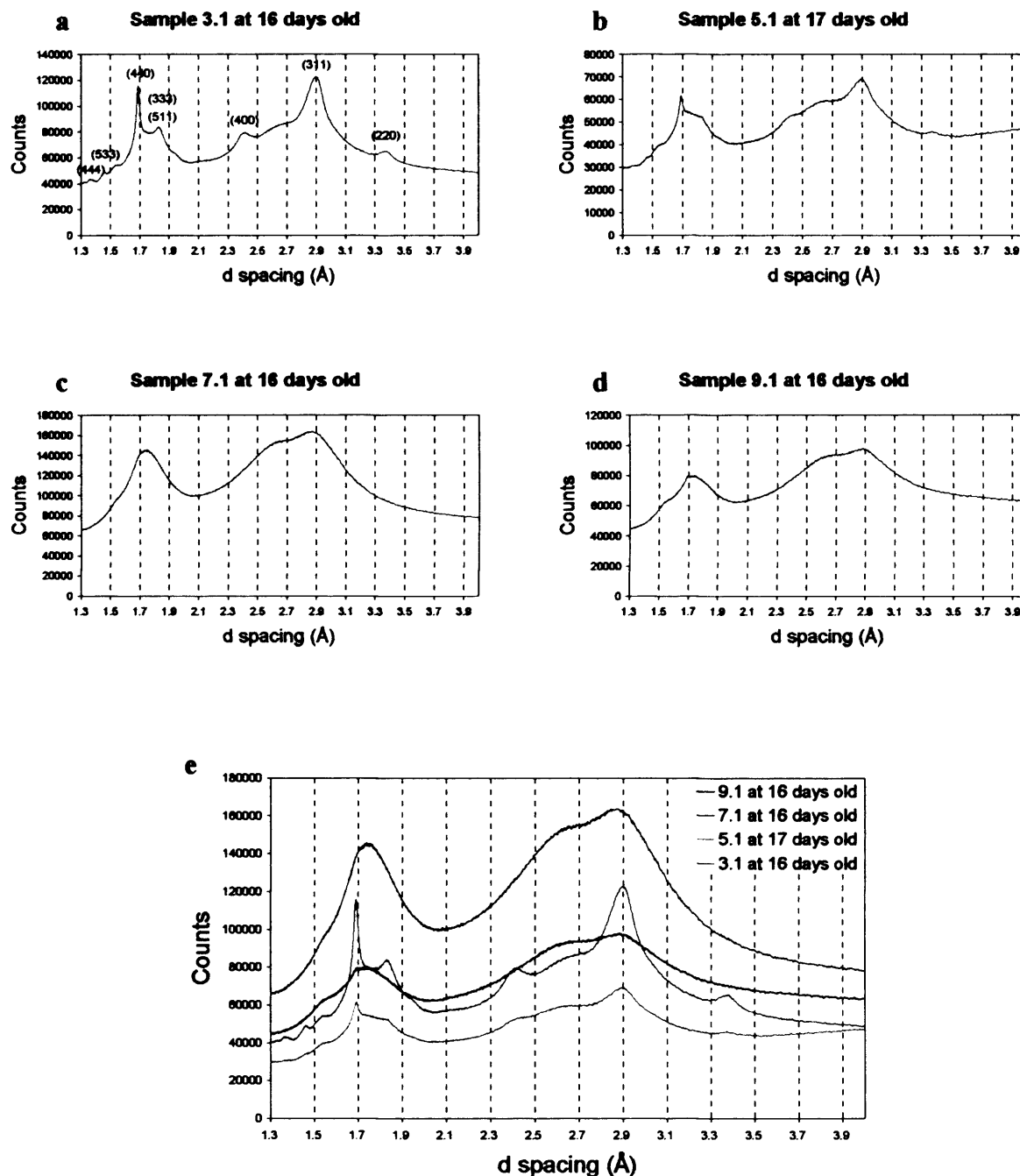


Figure 4.3 Synchrotron XRPD patterns of 16 - 17 day old NiS precipitate in terms of d-spacing (Å) versus counts. Sample 3.1 at 16 days old clearly displays polydymite structure. The corresponding polydymite planes are shown in (a). The pattern of sample 5.1 shows similar characters to sample 3.1 but the peaks are less sharp (b). The Bragg peaks of sample 7.1 and 9.1 are very broad, revealing poor crystallinity (c and d). These features are more obviously seen in (f) when they are plotted together.

less prominent. Even so, sample 5.1 displays a few characteristic polydymite peaks. The existence of the smaller particles resulting in the broad background is more prominent in the case of sample 5.1, suggesting that less of the original phase had evolved to the polydymite structure.

This trend of decreasing polydymite formation with increasing pH continues through samples 7.1 and 9.1. In these two samples, a broad peak at 1.73 Å is shown instead of the 1.67 Å polydymite peak and the 1.73 Å broad peak also exist as a background broad peak underneath the 1.67 Å peak for samples 3.1 and 5.1. Thus the broad peak at 1.73 Å seems to represents the nanoparticulate nickel sulfide phase that exists in all samples although it is more obviously shown in samples 7.1 and 9.1 where the polydymite crystallization is minimal. The peak at 1.73 Å could be best assigned to millerite (401) plane. Other likely phases with peaks close to this position are (012) and (102) planes of theophrastite at 1.75 Å, and (110) plane of NiAs-type NiS at 1.72 Å. All the four samples have their second maxima at c. 2.88 Å. This is a significant positive shift from the previous broad peak positioned at c. 2.7 Å in Fig. 4.1b, 1c and 1d, which matches the simulated broadened peak of millerite, to 2.88 Å, which could be possibly assigned to polydymite, heazlewoodite or vaesite. And it appears to accompany with the peak shift within the 1.7 Å region as mentioned above. It is also noted that, there is a step at 1.67 Å in sample 9.1 at 16 days which is the characteristic polydymite peak. The results indicate that for samples 5.1, 7.1 and 9.1, there is probably a solid state transformation between day 4 to day 16 or 17 during which period the previous millerite-like nanoparticles converted to polydymite phase. The evidence supporting this assumption is the peak shifts around 1.7 Å and around 2.8 Å. It is also noted that the broad peak around 2.6 Å exist in all the four patterns of the samples of 16 or 17 days from the synchrotron XRPD data. This peak appears in the sample 3.1 of 4 days analysis but it is not shown up in the other three samples at 4 days age. It is particularly prominent in 7.1 and 9.1 at 16 days age where the reflections of the relatively more crystalline polydymite are not as strong. The 2.6 Å peak may be assigned to the reflection of (101) plane of NiAs- type NiS, which is the main phase for sample 11.8 precipitated at pH 11.83 in this system.

The results of the X-ray diffraction experiments on the materials at 4 days and 16 or 17 days ages are summarized in Table 4.1.

Table 4.1 Summary of the X-ray diffraction analyses.

Samples at 4 days old	Conventional XRPD	<ol style="list-style-type: none"> 1. Polydymite phase is contained in sample 3.1. The peak around 2.6 Å may be indicative of the coexistence of NiAs-type NiS. 2. Samples 5.1, 7.1 and 9.1 possess a different phase from sample 3.1. 3. A peak shift is observed from c. 1.77 to c. 1.70 Å for samples formed in alkaline to acid conditions, which may be a sign for phase transformation.
	XRPD simulations	<ol style="list-style-type: none"> 4. The simulated polydymite pattern matches the XRPD pattern of sample 3.1 at 4 days age in the peak shape around 1.7 Å, but polydymite does not give the correct peak sizes. Another less crystalline phase, possibly millerite, heazlewoodite or NiAs-type NiS coexists in this sample. 5. Only the simulated millerite pattern gives the appropriate size proportion of the two major peaks for all the four samples. 6. Millerite appears to be the end member of the transformation series with the minor peak shifts from 1.82 Å for millerite to 1.77 Å for sample 9.1, 1.75 Å for sample 5.1 and 1.70 Å for sample 3.1.
Samples at 16 or 17 days old	Synchrotron XRPD	<ol style="list-style-type: none"> 7. Polydymite crystallized within 16 days. Polydymite formation is more prominent for samples formed in acidic conditions. 8. Another poor crystalline phase with a characteristic summit at c. 1.73 Å universally exists in all the four samples. It is best assigned to the (401) plane of millerite at 1.73 Å; or (012) and (102) planes of theophrasite at 1.75 Å; or (110) plane of NiAs-type NiS at 1.72 Å. 9. The universally existing peak around 2.6 Å in all the four samples at 16 or 17 days age may be assigned to the (101) reflection of NiAs-type NiS

4.3.4 Crystal growth

Fig. 4.4 shows the polydymite growth in samples at different ages from conventional XRPD data. It can be seen that the crystallization of polydymite is most prominent in sample 3.1. After 50 days, the polydymite crystals have grown to about 85 nm estimated by Scherrer's equation. The stronger XRPD intensities of sample at 50 days than those at 344 days is because of the bigger sample amount analysed. Obvious polydymite growth is also observed for samples 5.1 and 7.1 but this systematically decreases with increasing formation pH. For sample 9.1, the polydymite transformation is not obvious from the XRPD data. Fig. 4.4 confirms that the polydymite transformation occurs more readily in samples formed in more acid conditions.

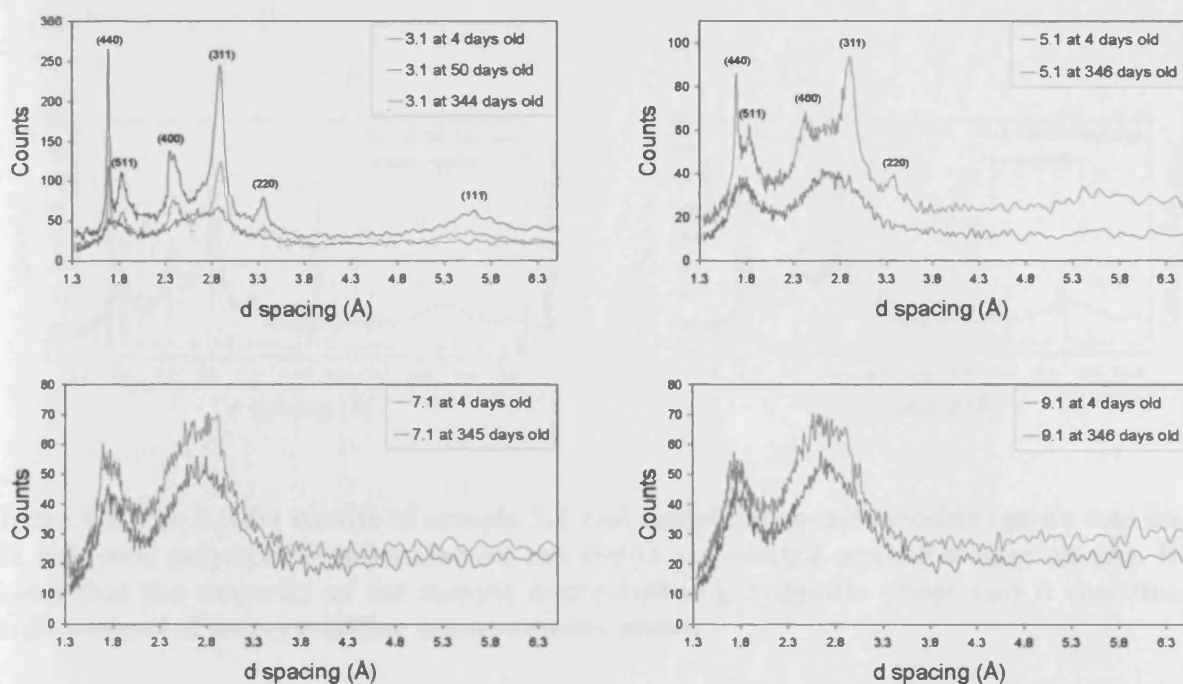


Figure 4.4 Conventional XRPD patterns of samples at different ages in terms of counts versus d spacing (Å). Polydymite grows more significantly in the NiS precipitated in acidic pH (sample 3.1 and 5.1).

Because the data of selected area electron diffraction indicates the formation of heazlewoodite in sample 3.1 at 241 days age (Chapter 5), and because heazlewoodite and polydymite have very similar X-ray diffraction lines, Fig. 4.5 shows the comparison of the match of bulk phases of polydymite and heazlewoodite with XRPD data of sample 3.1 at 344 days old. Compared with the two single fits, it can be concluded that polydymite is the proper phase assigned to the data because: (1) heazlewoodite has a large peak at c. 4.1 Å which is absent in sample data; (2) the sample data have peaks at 3.4 and 5.5 Å while they are absent for heazlewoodite; (3) polydymite matches all the significant individual peaks in the data and does not have any extra peak; and (4) all the peaks for polydymite bulk phase have roughly consistent relative intensities with the data, while the peak at 1.8 Å in heazlewoodite bulk phase is too large relative to the peak at 1.7 Å. However in the sample data, there is a small peak at 2.0 Å which cannot be assigned to polydymite but is probably heazlewoodite (200) reflection. The 2.0 Å peak is also found in the sample 5.1 at 345 days age. This supports the finding in electron diffraction results that heazlewoodite exists in the materials. Transmission electron microscope looks at the local properties of the material whereas XRPD examines the average of the powder sample and it is dominated by the well crystalline material that gives distinguished Bragg peaks. The results of SAED and XRPD suggest that polydymite is a better crystalline phase in sample 3.1 and heazlewoodite is poorly crystalline and/or smaller in particle size.

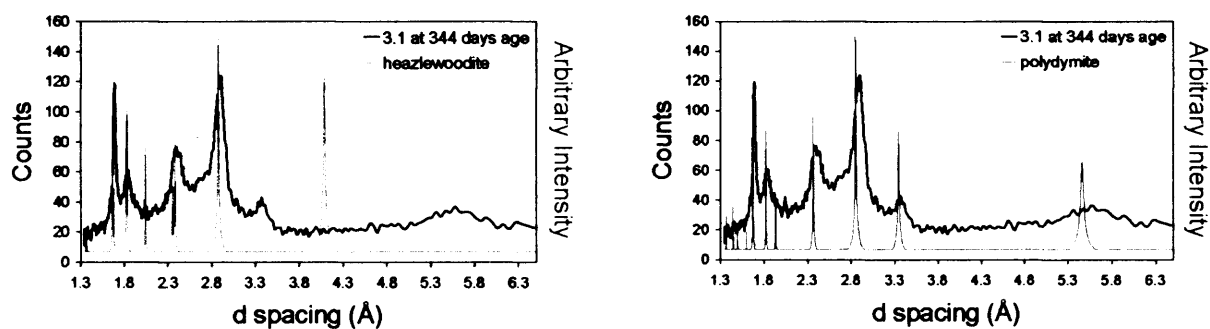
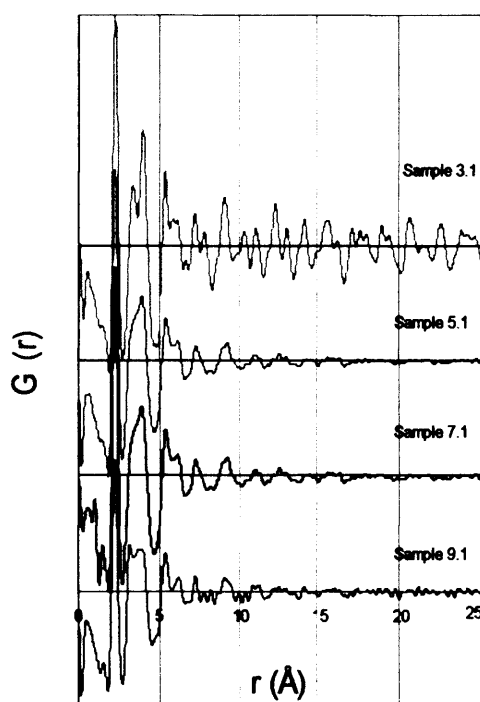


Figure 4.5 The XRPD results of sample 3.1 and calculated heazlewoodite (green line on the left) and polydymite (pink line on the right) are plotted against d spacing (Å). It shows that the majority of the sample is crystalline polydymite phase and it contains small amount of less crystalline heazlewoodite phase.

a. r (Å) up to 50 Å.



b. r (Å) up to 10 Å.

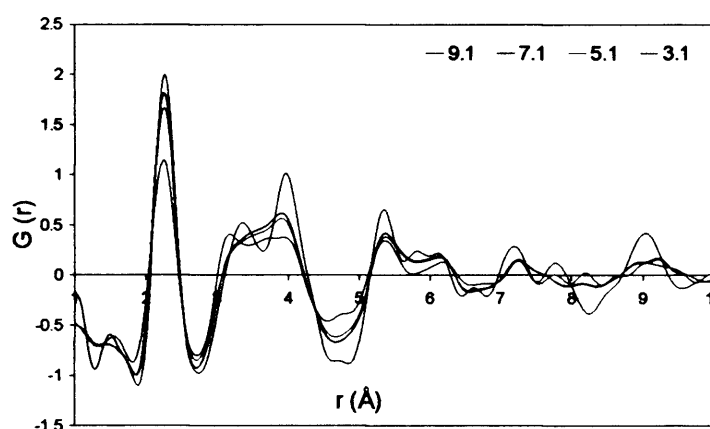


Figure 4.6 Experimental PDF of the NiS precipitates at 16 - 17 days old in terms of G versus r (Å). (a) shows that the amplitude of the features falls off after 10 Å except sample 3.1 whose $G(r)$ fluctuation continues after 50 Å. This reflects the short structural coherence for sample 5.1, 7.1 and 9.1 and sample 3.1 has relatively longer structural coherence. (b) compares the different $G(r)$ features of the four samples in the region below 10 Å.

4.3.5 PDF analyses

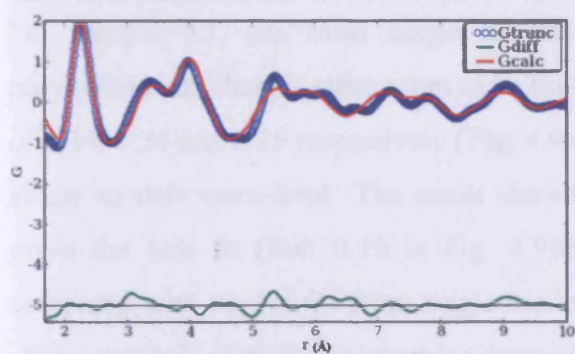
Fig. 4.6 shows the calculated PDF graphs of the four samples in the scales up to 25 \AA (Fig. 4.6a) and up to 10 \AA (Fig. 4.6b) in real space. The existence of the $G(r)$ peaks reflects the nature of the structure of the materials and the broadness of the $G(r)$ peak indicates considerable disorder. The fall-off of amplitude of the features in the experimental PDF graphs can be used for estimation of the size of structural coherence. For samples 5.1, 7.1 and 9.1, the fluctuation of $G(r)$ diminishes after 10 \AA while for sample 3.1, the fluctuation remains after 25 \AA . Therefore, I estimate the structural coherence of sample 5.1, 7.1 and 9.1 to be about 10 \AA and for sample 3.1, it is beyond 50 \AA (when scaling up to 50 \AA , the fluctuation still remains). This is consistent with the XRPD results in Fig. 4.3, where polydymite crystals are observed with estimated crystal size of 40 to 70 nm for sample 3.1.

Fig. 4.6b amplifies the region of 1 to 10 \AA of $G(r)$ for the four samples. Systematic changes are observed among the four samples. They all have the common first peak at 2.3 \AA , which could be alternatively interpreted as (1) a Ni-S distance in a NiS_5 coordination pyramid towards the vertex existing in materials such as millerite and godlevskite or (2) the Ni-S distance in a bipyramids with a Ni_3 triangle and two sulfur atoms at apices in heazlewoodite or (3) the Ni-S distance in Ni octahedral site in a cubic close packing of sulfur in polydymite. Peak positions vary after the first common peaks for different samples. Unlike others, sample 3.1 displays two discrete peaks at 3.1 and 4.3 \AA while samples 5.1, 7.1 and 9.1 show a broad area in this region which apparently results from a combination of several peaks. These peaks are not well resolved in this region due to the shortage of order range in the structure of the samples. Noted that although in Fig. 4.3, the XRPD patterns of samples 5.1 and 7.1 are different, the PDF data of samples 5.1 and 7.1 are similar. In XRPD patterns, peaks are located at the spacings between diffraction planes of the crystalline structure whereas, in PDF, the peak position related to the atomic bond lengths at high concentration in the specimen. The combined XRPD and PDF data may suggest that samples 5.1 and 7.1 share similar short-range structural components but differ in their long range coherence. This would be consistent with the nanoparticulate nature of these precipitates in that they may not have enough crystalline planes to develop conventional Bragg peaks in traditional powder X ray diffraction. The PDF of sample 9.1 differs from others in possessing a significant peak at 3.1 \AA , which might be the characteristic bond of Ni-Ni and O-O in theophrastrate $\text{Ni}(\text{OH})_2$.

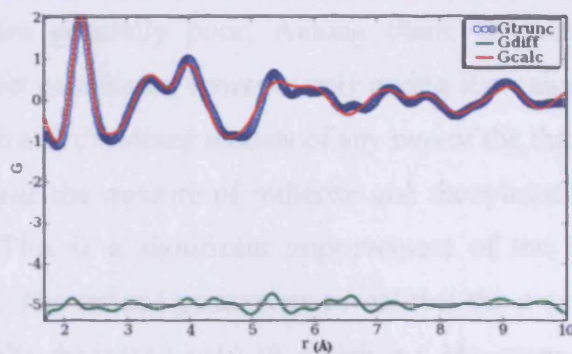
Not surprisingly, the polydymite model gives the best single fit for $G(r)$ of sample 3.1 (Fig. 4.7a), as agrees with the XRPD data where well crystalline polydymite peaks are observed on top of a broad background. The fitted graph at the peak around 5.4 \AA shows noticeable discrepancy. Calculated polydymite PDF shows that there is no peak with high intensity at this position. So the relatively significant peak at 5.4 \AA of $G(r)$ of sample 3.1 may be due to the coexistence of another phase that corresponds to the broad background in the XRPD data of sample 3.1. Several mixed models were tried. The best fit is given by the mixed model of polydymite and millerite, with R_w decreased from 0.24 to 0.20. In this mixed model, the unit cell of the resultant polydymite structure increases 1.4%, whereas for millerite, a reduction of 1.1% in a axis and an increase of 4.8% in c axis resulted. A small fit improvement is also obtained by using the mixed model of polydymite and heazlewoodite. The resultant R_w is 0.22. In this case, unit cell of polydymite model increases 1.68% while the unit cell of heazlewoodite model reduces 6.6%. Fig. 4.7b and 4.8c shows the improved fits from the two mixed models.

As mentioned above, the PDF data for samples 5.1 and 7.1 are similar. Fig. 4.8a, b and c show the three best fits obtained from single models for PDF data of sample 5.1. The three models are millerite, polydymite and Ni pentlandite with R_w at 0.24, 0.23 and 0.24 respectively. Examining the three fit graphs in detail, it is found that, in the region between 3 and 4 \AA , the sample data has a few combined peaks which cannot be resolved into two individual peaks. However, for models polydymite and Ni pentlandite, they only have two or one peak in this area respectively, so these two models are not the best fits for the data. The data agrees with the millerite model which has three significant peaks distributed in this region. Moreover, it also shows a better fit for the peak positioned at 5.4 \AA . For the above reasons, I think that millerite is the best single model for samples 5.1 and 7.1 among others. Refinements using all the 10 single models for PDF data of sample 7.1 are presented in Appendix Fig. 4A.3 for comparison of the goodness of fits with the different structural models.

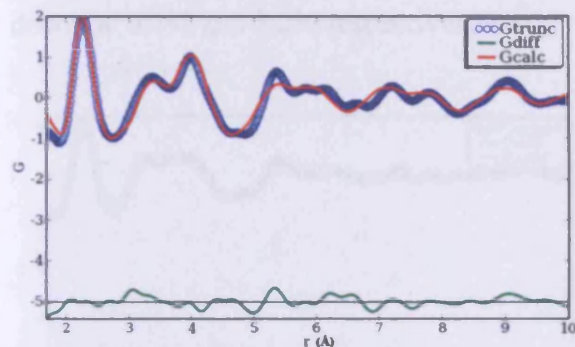
Significant improvement of fit (R_w : 0.15) achieved when mixed model of polydymite and millerite was attempted (Fig. 4.8d). This suggests the sample is a mixture of the two phases. This agrees with the observation of polydymite peaks in the synchrotron XRPD data for sample 5.1. For the refined millerite structure, there is 3.0% reduction in a axis and 3.5% increase in the c axis of unit cell. For the refined polydymite, the unit cell enlarged 0.95%.



a. Single polydymite model (Rw: 0.24)

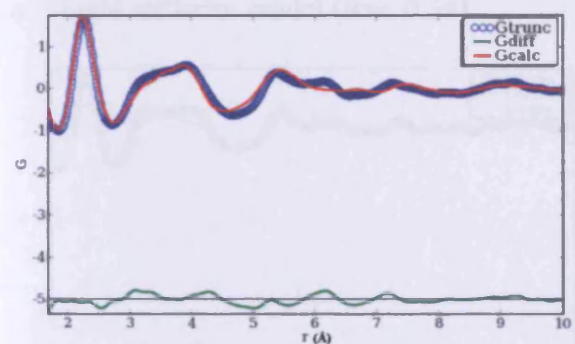


b. Mixed model of polydymite and millerite (Rw: 0.20)

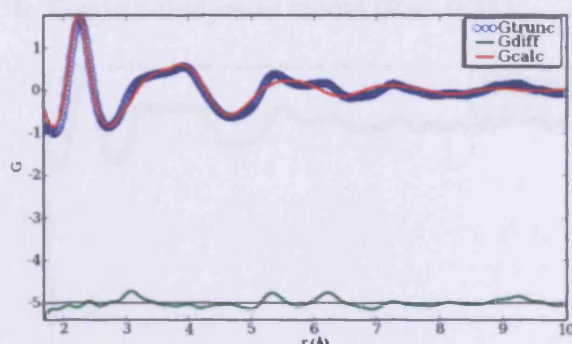


c. Mixed model of polydymite and heazlewoodite (Rw: 0.22)

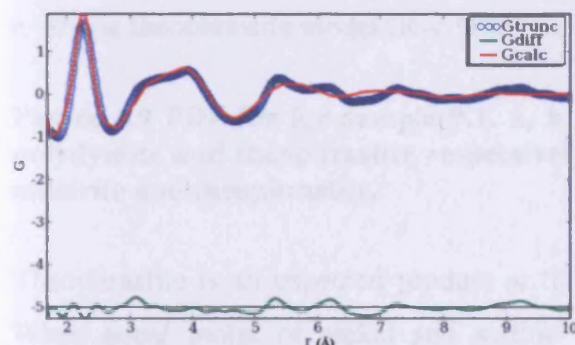
Figure 4.7 PDF fits for sample 3.1. The upper double lines are the calculated PDF from model (red) and the refined PDF from experiment (blue). The green line below shows the difference. a. single fit from polydymite; b. improved fit from mixed model of polydymite and millerite; c. improved fit from mixed model of polydymite and heazlewoodite.



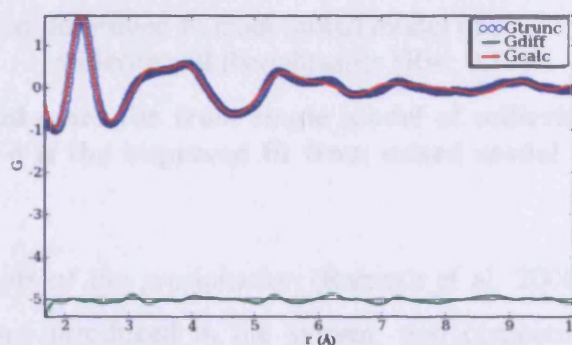
a. Single millerite model (Rw: 0.24)



b. Single polydymite model (Rw: 0.23)



c. Single Ni pentlandite model (Rw: 0.24)



d. Mixed model of polydymite and millerite (Rw: 0.15)

Figure 4.8 PDF fits for sample 5.1. a, b and c are fits from single models of millerite, polydymite and Ni pentlandite respectively. d is the improved fit from the mixed model of polydymite and millerite.

For sample 9.1, fits from single models are generally poor. Among them, millerite, polydymite and theophrastite seem to be the best candidates, however only giving R_w values of 0.34, 0.34 and 0.35 respectively (Fig. 4.9a, b and c). Mixed models of any two of the three single models were tried. The result shows that the mixture of millerite and theophrastite gives the best fit (R_w : 0.19 in Fig. 4.9d). This is a significant improvement of the fit compared with the results from single models. The refined parameters reveal that the a axis of the unit cell of millerite increases dramatically from 9.61 to 10.36, which is 6.8% increase and the c axis also increases 3.8%. However for theophrastite model, the a and c axis decrease 0.7% and 5.2% respectively.

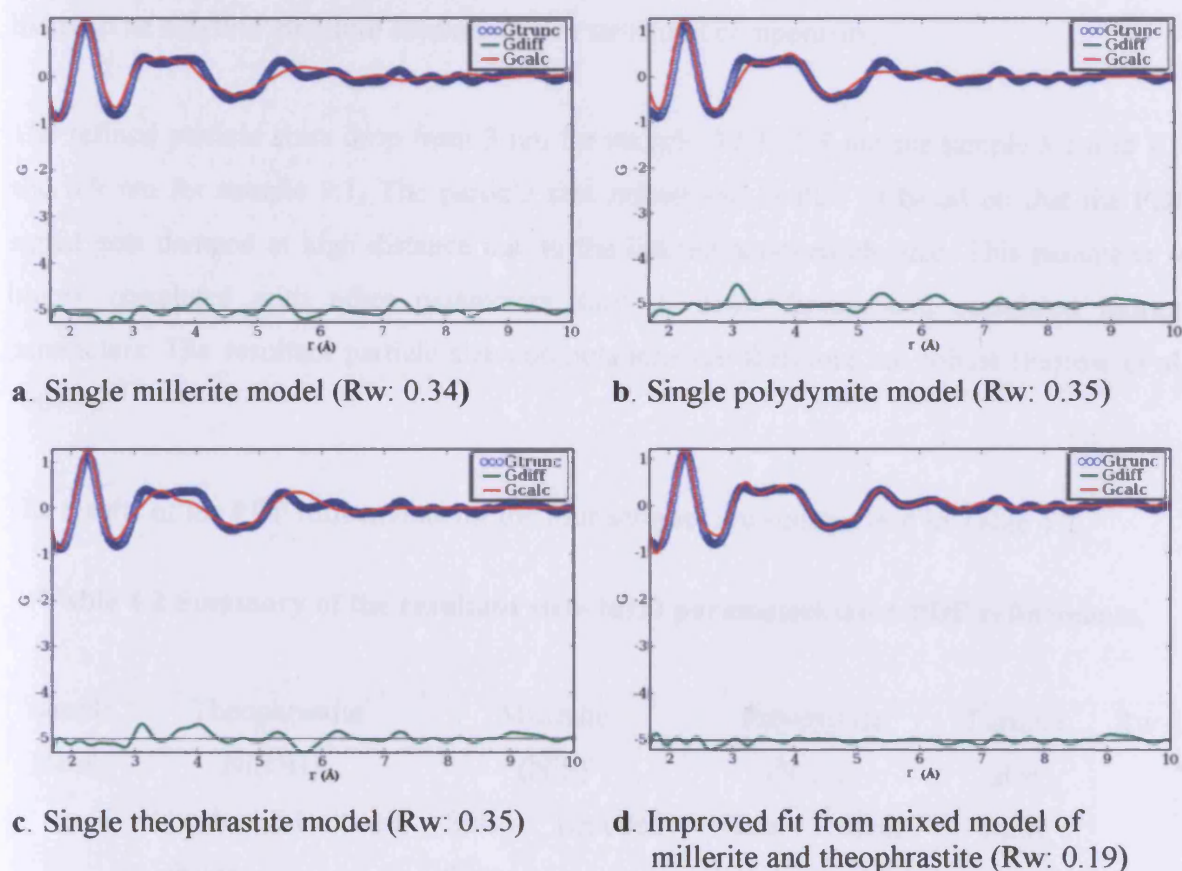
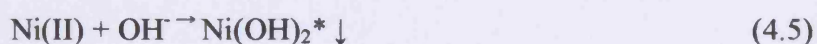


Figure 4.9 PDF fits for sample 9.1. a, b and c are fits from single model of millerite, polydymite and theophrastite respectively. d is the improved fit from mixed model of millerite and theophrastite.

Theophrastite is an expected product at this pH of the precipitation (Ramesh et al. 2006). When equal molar of nickel and sulfide was introduced in the system, two competing reactions occur during the precipitation process:



NiS* represents the hydrated nickel sulfide precipitate; Ni(OH)₂* represents the precipitated nickel hydroxide which may also contain water species in its layer structure (Ramesh et al. 2006). The dominant reaction of the two competing reactions depends on the kinetics and thermodynamics of the two reactions under the certain conditions. Although the kinetics of nickel sulfide precipitation are unknown, the mechanism is likely to be similar to the kinetics of FeS precipitation (Rickard 1995) since the rate is dependent on the rate of water exchange with HS⁻ and independent of the metal ion. The nickel sulfide precipitation is therefore expected to be much faster than that of theophrastrite in this system. This agrees with the refined results that millerite dominates this sample over theophrastrite. However, this does not necessarily mean that the two species exist as two discrete phases. Rather the material is likely to be a hybrid structure containing two structural components.

The refined particle sizes drop from 3 nm for sample 3.1 to 1.8 nm for sample 5.1 and 7.1, and 0.9 nm for sample 9.1. The particle size refinement in PDF is based on that the PDF signal gets damped at high distance due to the limited nanoparticle size. This parameter is highly correlated with other parameters such as scale factors and correlated motion parameters. The resultant particle size computations are therefore not robust (Farrow et al. 2007b).

The results of the PDF refinements for the four samples are summarized in Table 4.2.

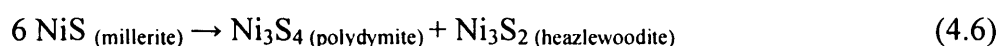
Table 4.2 Summary of the resultant structural parameters from PDF refinements.

Sample Name	Theophrastrite Ni(OH) ₂		Millerite (NiS)		Polydymite (Ni ₃ S ₄)		Particle size (nm)	Rw
	Scale factor	Unit cell	Scale factor	Unit cell	Scale factor	Unit cell		
9.1	0.43	<i>a</i> : -0.7% <i>c</i> : -5.2%	1.29	<i>a</i> : +6.8% <i>c</i> : +3.8%	-	-	0.9	0.19
7.1/5.1	-	-	0.24	<i>a</i> : -3.0% <i>c</i> : +3.5%	0.38	+0.9%	1.8	0.15
3.1	-	-	0.26	<i>a</i> : +1.1% <i>c</i> : +4.8%	0.35	+1.4%	3	0.20

4.4 Discussion

4.4.1 Phase identification and transformation

The XRPD and PDF results suggest that the NiS precipitates from pH 3.0 to 9.1 have an initial millerite-like structure. They transform to Ni₃S₄ (polydymite) in a solid state reaction with time. This transformation occurs more readily in samples formed in acidic conditions, XRPD and TEM results (Chapter 5) suggest that the transformation is accompanied by the formation of Ni₃S₂ (heazlewoodite). The reaction thus follows:



Apparently, the solid state transformation from NiS (millerite) to Ni₃S₄ (polydymite) is analogous to the iron sulfide system where FeS (mackinawite) transforms to Fe₃S₄ (greigite) by heating (Lennie et al. 1995) or under TEM beam (Horiuchi 1971). The transformation between mackinawite and greigite in FeS system is facilitated by a structural congruency between the two phases. In both structures, sulfur atoms are cubic close-packed and the transformation of mackinawite to greigite is a rearrangement of Fe atoms in the S array (Lennie et al. 1997). However, the structural analogy between NiS (millerite) and Ni₃S₄ (polydymite) is not obvious, and it is unlikely to be structurally related if it is an exsolution reaction as (4.6) because of the complex atomic rearrangement in the structure. The transformation in the NiS system does not require heat. The obvious positive factor for the transformation is time. The hydrogen bonding and the polar water incorporation in the NiS material which is absent in the FeS nanoparticles (Rickard et al. 2006), may help facilitate the transformation and the hydroxyl group that is incorporated in the samples formed in alkaline conditions may not. According to Zhang et al. (2003)'s study on the hydrated nanoparticulate ZnS, the polar surface water strongly interacts with the nanoparticles. In addition, the X-ray or electron beam bombardment may have an effect on the transformation but this needs further studies to confirm.

Aqueous precipitation is critically influenced by the pH. Under different pH, nickel sulfides have different solubilities (see Chapter 2). Acidic environments promote the solubility of nickel sulfides and the alkaline conditions tend to limit it (Cooper and Morse 1998). According to Ostwald's law, the immediate solid formed on precipitation is the phase that is disordered and unstable with the free energy closest to that of the reactants. In the media where the solid has a high solubility such as in the acidic solutions for nickel sulfides, the

disordered first precipitated phase transforms to a more stable phase in a step-wise manner during the course of dissolution and reprecipitation on the surface layer of the first precipitated solid to reach a lower free energy state. This repetitive dissolution and precipitation process facilitates the transformation to and crystallization of more stable phase, polydymite in the NiS system. In alkaline condition, on the other hand, the solubility of nickel sulfide is low and the precipitation process is thus fast. The fast precipitation results in the formation and preservation of disordered unstable nickel sulfide, as demonstrated in Fig. 4.1d. The transformation to more stable phase does not go much further because of its limited solubility. Hence, the material precipitated at pH 9, millerite phase, represents the early form of the precipitation and it is metastable relative to polydymite partly formed at pH 3.

Iron and nickel are closely related transition metals. However, their first precipitated species in water are structurally different. Disordered mackinawite is the first precipitated phase in the FeS system (Rickard 1969; Wolthers et al. 2003). It is in tetragonal layer structure. It consists of sheets of Fe atoms in square planar coordination. The Fe atoms are tetrahedrally coordinated to four sulfur atoms (Rickard and Luther 2007). However, millerite has a unique hexagonal structure. It has a five-fold coordination of Ni atoms by S forming a square pyramid NiS_5 , and five-fold coordination of ms by Ni forming a square pyramid SNi_5 . The NiS_5 pyramids connect with three edges and form columns along [110]. This forms Ni triangles with short Ni-Ni bond of 2.53 Å. For the thiospinel of the two species, greigite Fe_3S_4 and polydymite Ni_3S_4 share the similar structure. It is noted that pH 3 is also the optimal environment for aqueous synthesis of greigite, as apparently also the case for polydymite in this study. The difference in structure of the sulfides of iron and nickel may be due to their different electron configuration. Nickel with electron configuration $1s^2 2s^2 p^6 3s^2 p^6 d^8 4s^2$, has 6 electrons on its d subshell of the 3rd shell. This is two electrons more than that of iron ($1s^2 2s^2 p^6 3s^2 p^6 d^6 4s^2$). The spin-paired d^8 configuration of Ni^{2+} is typically coordinated in square pyramidal (Makovicky 2006) as such in millerite and another nickel sulfide with a peculiar structure, godlevskite.

It had been believed that the aqueous precipitates of nickel sulfides are mixture of several phases since the pioneer studies conducted by Thiel and Gessner (1914). The product phases depend on the pH of precipitation environments (Wang et al. 1997). Joris (1969) suggested that in acid conditions, the initial product is $\text{Ni}(\text{HS})_2$ which transformed to NiAs-type NiS and millerite. From the present results, no evidence of formation of $\text{Ni}(\text{HS})_2$ is found. Jeong

and Manthiram (2001) suggested, heazlewoodite formed at pH 5 - 6 after the precipitate was treated with reducing and sulfidizing agents. The results obtained in this work do not suggest direct heazlewoodite formation from solution. The product of nickel sulfide precipitation from neutral to alkaline conditions has been considered to be amorphous (Jeong and Manthiram 2001; Mellor 1936). The results in this study show that the major phase formed in alkaline conditions at 4 days age display a nanocrystalline millerite-like structure. The PDF results show that the material contains structural components of millerite and theophrastite at 16 days. A broad peak is observed at 2.6 Å in XRPD spectrum of sample 3.1 at 4 days and this peak is observed in XRPD patterns of all the four 16 - 17 day old samples. This peak might be assigned to the (101) plane of NiAs-type NiS phase. NiAs-type NiS is the main phase formed at pH 11.83 in the NiS precipitations system. However, results from the PDF refinements do not support the presence of NiAs-type NiS in samples from pH \leq 9. When NiAs-type NiS was tried as one component in the mixed model with polydymite, no improvement of fit results and the refined scale factor for the component of NiAs-type NiS is negligible.

4.4.2 Hydrated NiS

Chemical analysis shows that the NiS precipitated in alkaline conditions contains c. 22 wt% water. Zhang et al. (2003) showed that there is a crystalline core sized about 1.4 nm for 3 nm hydrated ZnS nanoparticles. This structural configuration is consistent with the observations of the hydrated NiS nanoparticles reported in this study. The structural coherence estimated from the XRPD simulations and fall-off features of the PDF patterns is about 1 nm. This corresponds to the size of the well crystalline NiS (millerite) core in the hydrated material. 1 nm spherical core is about 3 millerite unit cell overlaying each other along the *c* axis. Beyond this range, defects develop, partly due to the bonding of the surface water and partly due to the rapid precipitate nature of the material. The defective mantle area is about 1.5 nm in thickness containing about 24 ± 3 H₂O molecules per nm³. The corresponding thickness of the hydrated layer for ZnS in Zhang et al. (2003)'s model is 0.8 nm demonstrated by molecular dynamics calculation. It is reasonable that the hydrated nanoparticulate NiS in this study contains more water and is affected more strongly by water incorporation since the material is formed by direct precipitation from aqueous solutions, while the ZnS in Zhang et al. (2003) is previously formed in organic solvent and water was added subsequently into the organic solvent to allow the water adsorption onto the ZnS nanoparticles. The NiS formed in alkaline solutions is slightly sulfur insufficient, which is balanced by the incorporation of hydroxyl group. This may increase the effect of water bonding on the structure of the

material and is consistent with the observation of the increase in theophrastrite-like $\text{Ni}(\text{OH})_2$ in materials from alkaline conditions. Theophrastrite could occlude water between internal layers. However, the resultant unit cell of theophrastrite from the PDF refinement does not show the prolonged c axis but the opposite.

Compared with nickel and sulfur, oxygen and hydrogen have smaller X-ray scattering factors. So water affect the X-ray scattering experiments mainly by influencing the positions of nickel and sulfur, and thus the X-ray scattering patterns for these two heavier elements, rather than the addition of X-ray scattering patterns of oxygen and hydrogen elements. The disorder and strains brought about by the water inclusion in the NiS particles result in the broadness in XRPD and PDF patterns.

4.4.3 Particle size

The PDF refinements on particle sizes indicate that the structural coherence of the materials decrease in sequence from samples prepared in acidic medium to those from alkaline medium. The fall-off of the features in the experimental PDF graphs agrees that samples 5.1, 7.1 and 9.1 are just above 1 nm in diameter and the size of sample 3.1 is over 50 nm. These results are roughly in accordance with the thickness calculated from simulated XRPD patterns with Scherrer's formula. However, they are smaller than the particle sizes measured as 2 to 9 nm under high resolution electron microscope (HRTEM) (Chapter 5). The reason for this is that, the particle size estimated in both PDF analysis and Scherrer's formula consider the internal structural coherence, which is the crystalline core of the nanoparticles. Beyond this range, the structure is influenced by the bonding of water and loses its integrity. The gap between the sizes of the well crystalline core and the whole crystal measured in HRTEM supports the core-mantle model for the structure of the hydrated nanoparticulate NiS.

4.5 Conclusions

The nickel sulfides precipitated in aqueous system under ambient conditions pH range 3.0 - 11.8 are nanocrystalline. The early form of the precipitates from moderate pH range 3.0 to 9.1 is with millerite-like NiS structure. It gradually transforms to the more stable Ni_3S_4 (polydymite) phase in solid state under standard conditions. The XRPD evidence supports the idea that the reaction is accompanied by Ni_3S_2 (heazlewoodite) production. Solids

formed at low pH more tend towards this transformation. Well crystalline polydymite crystals are observed in about two weeks after the sample is precipitated at pH 3. Samples precipitated in pH 5 - 7 at 16 or 17 days old display a mixture of millerite and polydymite structural components, which agrees with the transformation process from NiS (millerite) to Ni₃S₄ (polydymite). Sample formed at pH 9 is dominated by NiS (millerite) structure mixed with Ni(OH)₂ theophrastite structural components, due to the competitive reactions between sulfide and hydroxyl group to react with Ni²⁺ in solution. The polydymite crystallization is not obvious for this sample after 346 days. Nickel sulfide precipitated at pH 11.83 with Ni:S mole ratio of 1:2 develops a well-crystalline NiAs structure with particle size about 18 nm.

Considerate disorder is observed for the precipitated nanomaterials. Disorder is brought in by the fast precipitation process due to the limited solubility of nickel sulfides in aqueous system, and the water bonding in the mantle phase that modifies the crystalline structure of the nanoparticles.

The structural coherence for samples formed in neutral to alkaline conditions is about 1 nm and it is larger for samples formed in acidic conditions. This is the size of the crystalline NiS (millerite) core. The gap between the size of the structural coherence and the crystal size observed from the HRTEM images explains by the proposed core-mantle structural configuration for the hydrated nanoparticulate NiS. Beyond the range of the 1 nm crystalline core, the structure is highly defective and influenced by the water bonding.

APPENDIX**XRPD Repeatability and Calibration Test****4A.1 Introduction**

There are three aims for the X ray diffraction instrumental test: (1) current powder XRPD data of the nickel sulfides precipitated in different pH environments generally give two broad peaks with small variation in the shapes at the top of the broad peaks, some of them appearing to be composed of several subpeaks, while others fairly round. This set of experiments is designed to assess whether these variations are due to the structural characteristics of the specimen or the instrumental error; (2) the systematic shifts of the peak positions during continuous measurements are tested and; (3) to calibrate the working conditions of the instrument.

4A.2 Methods

For the aims (1) and (2), nickel sulfide sample was prepared by mixing 0.1 M 50 mL solutions of $\text{NiSO}_4 \cdot 6\text{H}_2\text{O}$ and $\text{Na}_2\text{S} \cdot 9\text{H}_2\text{O}$ of analytical grade. All reagents were made up in deionised 18.2 M Ω cm (DW, MilliQ) water and was deoxygenated by bubbling with oxygen-free nitrogen for at least 45 minutes. The precipitation and filtration were conducted in a N_2 -filled MBraun Labmaster 130 anoxic chamber maintained at $\text{O}_2 < 2$ ppm level. Products were washed, filtered and freeze dried for at least 48 hours, then ground into fine powders and stored in standard conditions in the anoxic chamber before analyses. For the aim 3), analytical KCl (99% from Fisher Scientific) was used and was grounded to powder before being loaded into the instrument.

XRPD experiments were carried out on a Philips PW 1710 using $\text{CuK}\alpha$ radiation ($\lambda = 1.54056$) scanning from 5.01° to 69.99° . The scan rate of full scan is 0.02° per 1.25 s. The scan rate of short scan is 0.02° per 0.5 s. The nickel sulfide sample was analysed for 9 continuous runs with full scan programme. KCl was analysed with both short scan and full scan programmes. The data for each of them were collected on three repetitive runs.

4A.3 Results

Fig. 4A.1 shows the XRPD patterns of the nine scans on nickel sulfide in d-spacings with added intensities for easy comparison of the peak shapes. It can be seen that for the same specimen, there is some variation of the shape at the top of each broad peak. For example, at the major broad peak around 2.7 Å, scans 1, 7 and 9 have fairly round tops while it divides into two subpeaks for scans 2, 3, 5 and 6. No systematic shift of the peak positions is observed during the nine analyses. This can be reconfirmed in Fig. 4A.2 where the data points are averaged in every 8 counting points.

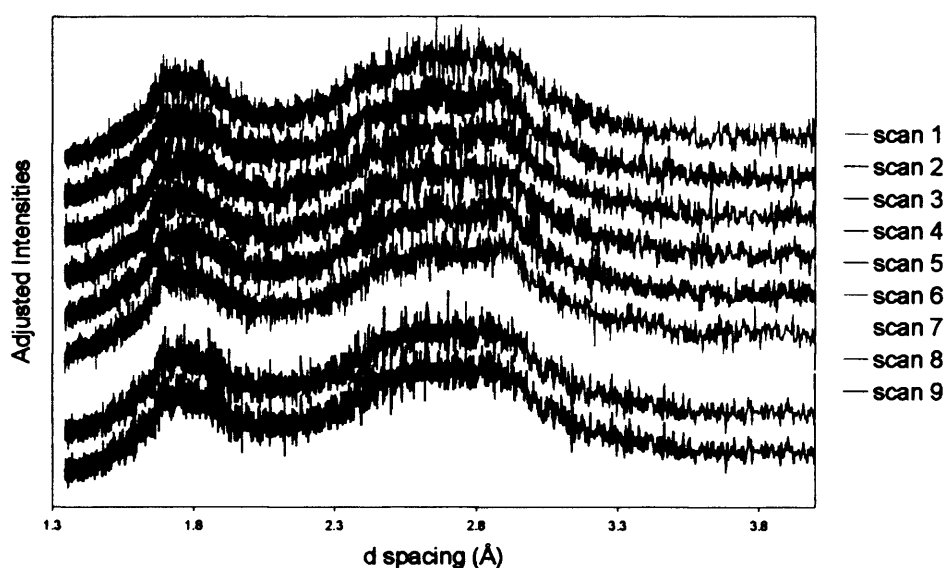


Figure 4A.1 Conventional XRPD data of 9 batch runs on the NiS precipitate. It shows that the variations on the top of the broad peaks are due to instrumental error, rather than the sample structure.

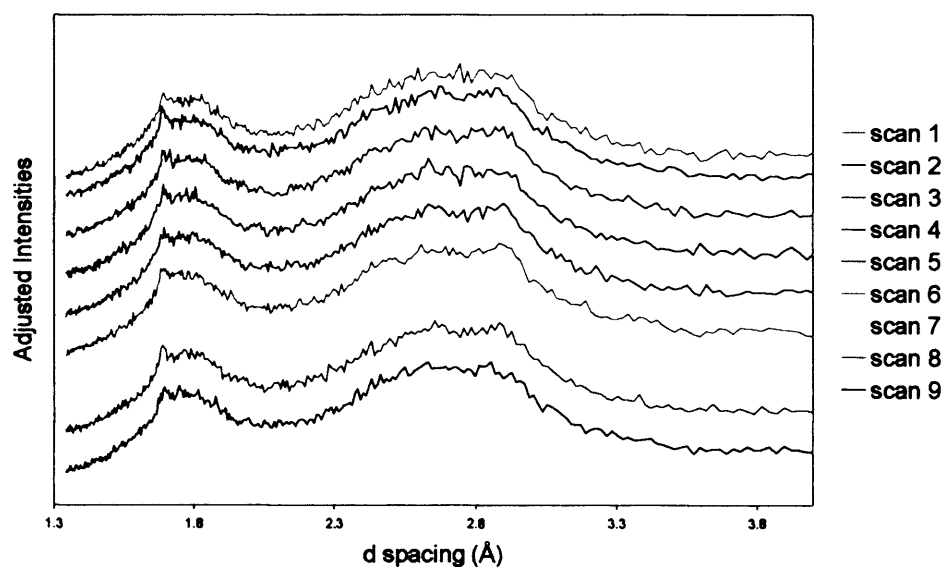


Figure 4A.2 Smoothed conventional XRPD data of 9 batch runs on the NiS precipitate.

4A.3 Results

Fig. 4A.1 shows the XRPD patterns of the nine scans on nickel sulfide in d-spacings with added intensities for easy comparison of the peak shapes. It can be seen that for the same specimen, there is some variation of the shape at the top of each broad peak. For example, at the major broad peak around 2.7 Å, scans 1, 7 and 9 have fairly round tops while it divides into two subpeaks for scans 2, 3, 5 and 6. No systematic shift of the peak positions is observed during the nine analyses. This can be reconfirmed in Fig. 4A.2 where the data points are averaged in every 8 counting points.

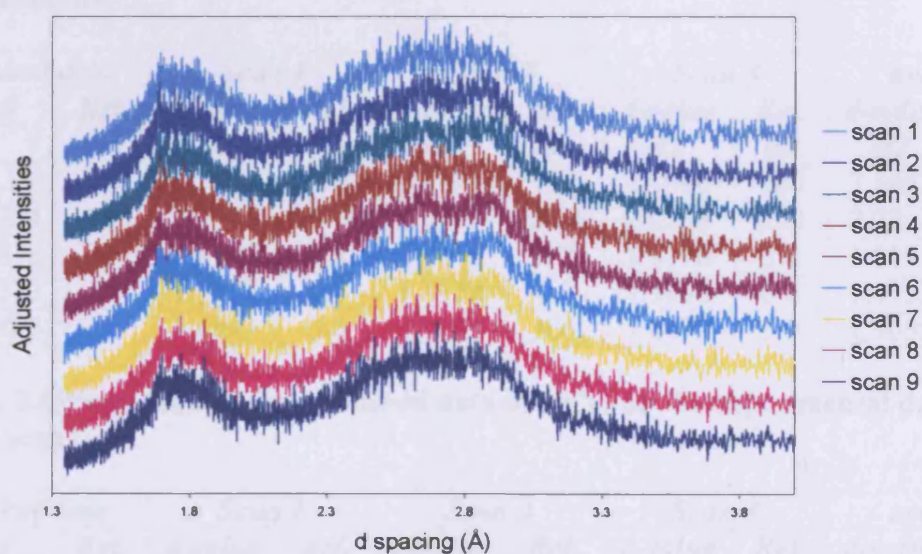


Figure 4A.1 Conventional XRPD data of 9 batch runs on the NiS precipitate. It shows that the variations on the top of the broad peaks are due to instrumental error, rather than the sample structure.

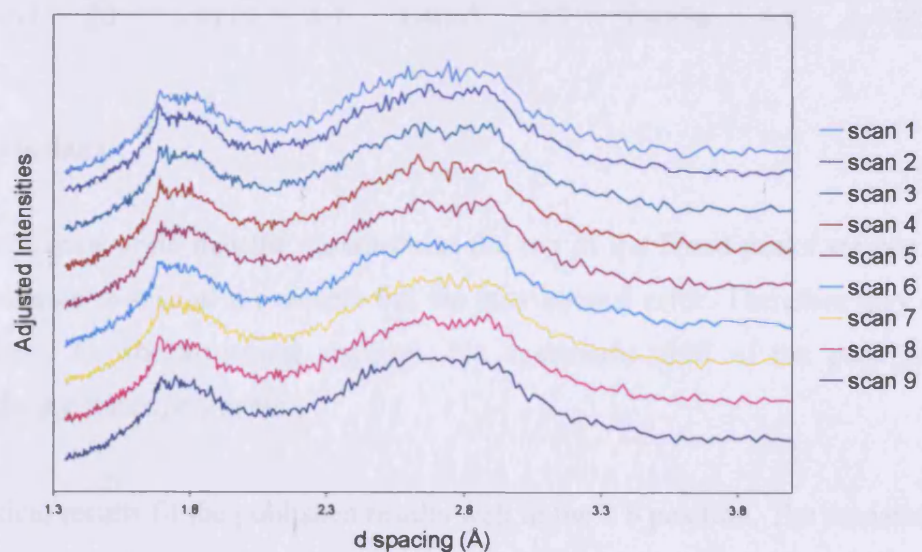


Figure 4A.2 Smoothed conventional XRPD data of 9 batch runs on the NiS precipitate.

Tables A4.1 and A4.2 summarize the results of short scans and full scans on KCl samples compared with the published values of this material. The positions of analytical data fit the published data very well in both short-scan and full-scan analyses. The difference between the averaged three scans with the published data is within 0.5 % and 0.18 %. The standard deviation of the three scans for each peak is within 0.017 and 0.001 which is very small and negligible for the purpose of this thesis work. However, the intensities do not match the published data well for both types of scans. The discrepancy is due to the orientation effect from the lack of sufficient grounding of the sample powder.

Table 4A.1 Comparison of the published data of KCl and the experimental data from three short scans.

<i>Published data</i>			<i>Scan 1</i>		<i>Scan 2</i>		<i>Scan 3</i>		<i>average</i>	
<i>hkl</i>	<i>d</i>	<i>Rel. int.</i>	<i>d-value</i>	<i>Rel. int.</i>	<i>d-value</i>	<i>Rel. int.</i>	<i>d-value</i>	<i>Rel. int.</i>	<i>d-value</i>	<i>Rel. int.</i>
200	3.15	100	3.1441	100	3.1441	100	3.1446	100	3.1443	100
220	2.224	59	2.2255	22.8	2.2258	20.9	2.2258	22.1	2.2257	21.9
222	1.816	23	1.8195	3.8	1.8195	3.7	1.8190	3.9	1.8193	3.8
400	1.573	8	1.5753	5.7	1.5754	6.0	1.5753	6.2	1.5753	6.0
420	1.407	20	1.4093	5.6	1.4094	6.0	1.4099	5.9	1.4095	5.8

Table 4A. 2 Comparison of the published data of KCl and the experimental data from three full scans.

<i>Published data</i>			<i>Scan 1</i>		<i>Scan 2</i>		<i>Scan 3</i>		<i>average</i>	
<i>hkl</i>	<i>d</i>	<i>Rel. int.</i>	<i>d-value</i>	<i>Rel. int.</i>	<i>d-value</i>	<i>Rel. int.</i>	<i>d-value</i>	<i>Rel. int.</i>	<i>d-value</i>	<i>Rel. int.</i>
200	3.15	100	3.1741	100	3.1747	100	3.1747	100	3.1745	100
220	2.224	59	2.2462	10.1	2.2400	14.6	2.2464	9.1	2.2442	11.3
222	1.816	23	1.8265	3.7	1.8261	3.0	1.8268	3.4	1.8265	3.4
400	1.573	8	1.5758	3.3	1.5761	8.0	1.5797	7.7	1.5799	7.8
420	1.407	20	1.4139	4.7	1.4063	2.7	1.4136	4.8	1.4095	5.8

4A.4 Conclusions

The results demonstrate that the variations at the top of the broad peaks are not due to the structural characteristics of the sample but the instrumental error. Therefore they should not be considered for the structural analyses. No systematic shift of the peak positions is observed during the experiments.

The analytical results fit the published results well in the 2θ position. The deviation between the intensities from the published data and the experimental data is due to the orientation effect. The data show good repeatability in the examined experiments.

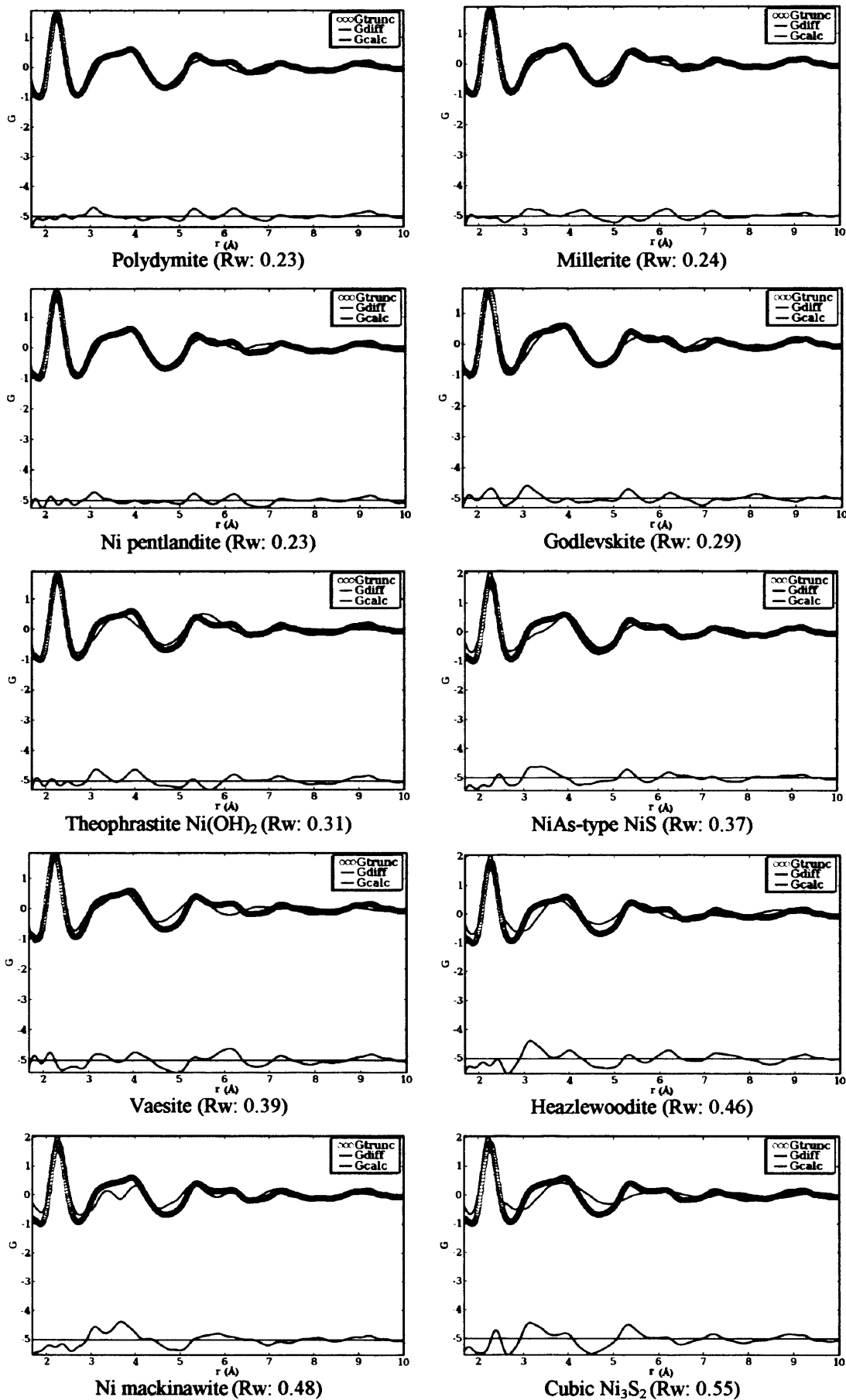


Figure 4A.3 PDF fits for sample 7.1 from all single models.

Acknowledgements

I thank Kenneth D. M. Harris for his helpful discussions on the PDF analysis and Zhigang Pan for teaching me to do the Rietveld refinements. The synchrotron XRPD data were collected in Spring-8 synchrotron radiation facility (Japan) by Kenichi Kato. The synchrotron X-ray scattering data were transformed to $G(r)$ by Shinji Kohara at Spring-8. I wish to acknowledge the use of the Chemical Database Service at Daresbury, UK.

Chapter 5

Electron Microscopic Study of “Amorphous” Nickel Sulfide

Figures

Figure 5.1 HRTEM images of sample 3.1.

Figure 5.2 HRTEM images of sample 5.1.

Figure 5.3 HRTEM images of sample 7.1.

Figure 5.4 HRTEM images of sample 9.1.

Figure 5.5 SAED analyses of sample 3.1.

Figure 5.6 SAED analyses of sample 5.1.

Figure 5.7 SAED analyses of sample 7.1.

Figure 5.8 SAED analyses of sample 9.1.

Figure 5.9 SEM images of the NiS precipitates at magnifications 80 K and 500 K.

Table

Table 5.1 Summary of the measured fringe distances in HRTEM images.

Abstract

“Amorphous” nickel sulfide, prepared in aqueous solutions at ambient temperatures, is nanocrystalline nickel (II) monosulfide with crystal sizes ranging 2 - 9 nm. The majority of the materials show a millerite-like structure on HRTEM images and SAED patterns. The nanoparticles may be platy with the thickness perpendicular to the (131) direction. Ni₃S₂ (heazlewoodite) is detected as the accompanying product of the solid state transformation from NiS (millerite) to Ni₃S₄ (polydymite). The specific surface area estimated according to the HRTEM images is 558 m²/g. SEM results show that the NiS nanoparticulates aggregate to pseudospherical particles with sizes up to 40 nm and produce a material which is highly porous and maintains a large surface area ideally suited to catalysis. These materials have been proposed to have played a key role in the origin of life and have been previously been found to be apparently amorphous in X-ray powder diffraction (XRPD) studies. The “amorphous” nature of the NiS results from the effect of the nanosized particles in conventional X-ray powder diffraction, especially extreme spectral line broadening effects.

5.1 Introduction

Nanoparticles are abundant in planetary systems, especially in the low-temperature environments. They play special geochemical and mineralogical roles because of the novel size-dependent effects. One of the typical geochemical processes for nanoparticle formation is that involved in the high degrees of supersaturation, leading to the production of many crystal nuclei with subsequent limited crystal growth. In the low temperature systems of some hydrothermal vents, the reduced sulfide-containing metalliferous, submarine seepage meets cold ocean water. This environment has been proposed as the site for the origins of life where the precipitates of iron and nickel sulfides played a key role in the very beginning of the evolution process (e.g. Russell and Hall 1997).

Nickel sulfides exhibit some novel physical and catalytic properties. For example, they are common catalysts for hydrogenation (Topsoe et al. 1996) and carbon liquefaction reactions, and are used for storage of solar energy (Fernandez et al. 1993). Their effects on toughened glass and their carcinogenic effects have also received much attention. A number of experiments have demonstrated the potential of nickel and iron sulfide precipitates to promote some interesting organosynthetic reactions, such as the synthesis of acetic acids

(Huber and Wächtershauser 1997) and peptides (Huber and Wächtershauser 1998) (See Table 8.2 for a summary). For this reason, these materials have been implicated in the origin-of-life scenarios. However, the structural properties of the Ni sulfides involved in these experiments were not defined.

Nickel sulfides are known to form in a variety of crystalline phases, including stoichiometric (e.g. NiS, NiS₂, Ni₃S₂, Ni₃S₄, Ni₉S₈), non-stoichiometric (e.g. NiS_{1.03}, NiS_{1.97}) crystalline phases and a phase which is apparently amorphous under conventional X-ray powder diffraction (XRPD) analyses.

The products of aqueous precipitation of nickel sulfide under ambient condition are not well defined (See a review in Chapter 2). They are traditionally regarded as “amorphous” (Jaramillo and Sonnenfeld 1989; Thiel and Gessner 1914; Wang et al. 1997) and hydrated (Nicholls 1973). Jeong and Manthiram (2001) studied nickel sulfide precipitates in aqueous solutions under a range of pH conditions and concluded that the products formed in neutral and alkaline conditions were X-ray amorphous. Chemical analyses show that there is about 22 wt% of water present in the materials and the composition is thus NiS·xH₂O, where $x \sim 1.5$ (Chapter 3). A detailed X-ray powder diffraction study (Chapter 4) showed that the dominant material in Jeong and Manthiram’s amorphous zone is nanoparticulate and has a core with millerite-like structure.

HRTEM is currently the most rigorous technique for the study of nanomaterial (Thomas and Midgley 2004). In this chapter, I present the results of an HRTEM investigation of the nanoparticulate nickel sulfide precipitates.

5.2 Methods

5.2.1 *Basics of the analytical methods*

The advantages of TEM technique over X-ray diffraction mainly rely on the shorter wavelength of electron (typically 1/40 of X-rays), strong atomic scattering and the ability of examining particles at nanometre scale. The small wavelength results in the radius of the Ewald sphere being much larger in electron diffraction. Coupled with spiking reciprocal lattice points from thin specimen, more of the two dimensional distribution of reciprocal lattice points are revealed. For a specimen of nanocrystalline sizes where XRPD does not

give discrete peaks, the electron wave may satisfy the Bragg's law while interacting with the material. The d spacings of the crystalline nanostructure in the specimen can be thereby determined.

In the HRTEM imaging mode, the particle size and shape can be estimated. The fringes and lattice images in HRTEM images are created by the phase contrast from the interference of the transmitted wave and diffracted wave of the electron beam when a crystalline structure in the specimen satisfies Bragg's law. The production of the lattice and fringe images demonstrates the crystallinity of the material. A set of fringes in an HRTEM image may provide information about the size and shape of the nanoparticles (Ohfuji and Rickard 2006). However, the apparent size is subject to the adjustment of defocus of the microscope.

The lattice image is not a direct representation of the crystallographic structure of the specimen but is highly nonlinear (Spence 1988). Accurate determination of lattice spacings of nanoparticulate specimen from HRTEM images is not straightforward. The resulting HRTEM lattice images of nanoparticles may be distorted subject to the projection of electron beams tilting away from the direction of zone axis. The error between the direct measurement of the distance in the fringe and the actual d spacings in the nanoparticles is usually within a few percentages and can be up to 10% (Malm and O'Keefe 1997; Tsen et al. 2003). Tsen et al. (2003) showed that by taking the average of fringe measurements, the error can be minimized and the average of the measurements well represent the real d spacings in the material.

In selected area electron diffraction (SAED) mode, the d spacings of the sample structure and the electron diffraction patterns follow a simple linear relationship between the instrumental conditions and the d -spacings in the specimen.

$$Rd = L\lambda \quad (5.1)$$

where R is the distance between the centre and the diffraction spot on the diffraction pattern; d is the d -spacings in the crystalline specimen; L is the camera length and λ is the electron wavelength. By measuring the distance from the centre to the diffraction spots or the diameter of rings in a electron diffraction pattern, the d spacing of the structure is readily obtained. Unfortunately, the precision of this method is not high and it critically depends on the diffraction-lens setting (Steed and Morniroli 1992). Moreover, nanoparticles with zone axes tilting away from the orientation of incident beam could also produce diffraction spots

but with an error. The shape of nanoparticles influences the shape of the reciprocal lattice points in the SAED patterns. In addition, the dynamic diffraction in a “thick” sample produces extra diffraction spots. A 5% error is common for a measurement in this way (Steeds and Morniroli 1992). Obtaining high precision single crystal SAED requires the sample crystals to be larger than 100 nm in diameter (Cowley 2004). Aggregates of smaller crystalline particles are polycrystalline and the resulting SAED patterns are rings, analogous to XRPD patterns. The diameters of rings in an SAED pattern generated by polycrystalline diffraction can be seen as the average the single diffraction spots and therefore represent the d spacings of the structure with a higher precision than direct measurement of the individual diffraction spots. Measurements of the rings in electron diffraction patterns were performed in the present work to estimate the d spacings of the crystalline structure of the samples.

Nickel sulfides are found to be sensitive to electron beam bombardment. Phase transformation of nickel sulfide from millerite to α Ni_7S_6 is observed under continuous exposure of electron beam (Putnis 1976). In addition, transition metal sulfides are extremely sensitive to low oxygen potentials and it has been suggested that, chemically, even the oxygen potential in an electron microscope “vacuum” may be sufficient to cause oxidation of sulfide samples (Rickard and Luther 2007). The phase transformation that may occur during the examination needs to be taken into account for the data analysis.

5.2.2 Sample preparation

For aqueous precipitation, analytical grade $\text{NiSO}_4 \cdot 6\text{H}_2\text{O}$ and $\text{Na}_2\text{S} \cdot 9\text{H}_2\text{O}$ were used as starting materials. All reagents were made up in deionised 18.2 M Ω cm (DW, MilliQ) water, which was deoxygenated by bubbling with oxygen-free nitrogen for at least 45 minutes. All precipitation and filtration were conducted in a N_2 -filled MBraun Labmaster 130 anoxic chamber maintained at $\text{O}_2 < 2$ ppm level. Buffer solutions were used for adjusting the pH for most precipitations. pH 3 buffer was prepared by mixing potassium hydrogen phthalate and HCl. pH 5, 7 and 9 buffer powders were from Hydrion™ and are composed of acetate, phosphate and carbonate respectively. The end pH of the filtrate after the precipitation was measured. They were within the ranges of 3.0 - 4.0, 5.0 - 5.8, 7.0 - 7.3 and 8.9 - 9.1 respectively for precipitations made in pH 3, 5, 7 and 9 buffers. For pH 3.0 - 4.0 and pH 5.0 - 5.8 conditions, nickel sulfate solutions were buffered; for pH 7.0 - 7.3 and pH 8.9 - 9.1 conditions, sodium sulfide solutions were buffered. A typical precipitation was conducted by dropwise addition of one solution (0.1 M, 50 mL) into a stirred and buffered solution (0.05 M, 100 mL). Sample numbers 3.1, 5.1, 7.1 and 9.1 refer to the samples precipitated at pH 3.0

- 4.0, pH 5.0 - 5.8, pH 7.0 - 7.3 and pH 8.9 - 9.1 respectively. Products were washed, filtered and freeze dried for at least 48 hours, then ground into fine powders. The prepared samples were stored as dry solids at 25 °C in the N₂ atmosphere at O₂ < 2 ppm in the anoxic chamber. Samples of different ages were investigated. The sample age is referred to from the date it was precipitated.

5.2.3 Transmission electron microscopy (TEM)

Several TEM instruments were used including JEOL 2010 with EDX, JEOL 4000, JEOL 3000F with EDX, JEOL 200CX and Philips CM20 with EDX. The solid nickel sulfide precipitates/aggregates were placed in liquid ethanol and then pipetted onto Cu grids. In order to obtain smaller and thinner particle of nickel sulfide on the grid, some samples were shaken in ultrasonic bath in ethanol for about 30 minutes before loading into the instruments. The samples were loaded into the instrument as quickly as possible. However, this cannot prevent the possible oxidation on the specimen. The pumping down time of the TEM chamber after the insertion of the samples is another source of oxidation. During this period the samples are briefly exposed to rapidly decreasing oxygen potentials. The data were recorded by either negative films or CCD camera. Negative films were scanned into the electronic version. All electronic data were measured with Image-Pro Plus 5.1 image processing and analysis software. Energy dispersive X-ray (EDX) experiments were conducted for elemental analysis.

5.2.4 Scanning electron microscopy (SEM)

Scanning electron microscopic (SEM) analyses were conducted on a Cambridge Instruments (LEO) S 360. Images of samples at magnifications of 500K and 80K were taken. SEM-EDX analysis was done on an Oxford Instruments INCA ENERGY X-ray analysis system.

5.3 Results

5.3.1 Particle size, shape and polydiversity

Figs. 5.1 - 5.4 show the HRTEM images of the samples at about 23 days old. At magnifications over 500K, the fringe and lattice images are clearly displayed for all the samples examined. The fringe images represent crystals in the aggregates. Most fringes in sample 3.1 fall in the range of 2 to 5 nanometres with irregular shapes (Fig. 5.1).

For sample 5.1, the majority of the particles have smaller crystalline sizes ranging from 2 to 3 nm, again with irregular shapes (Fig. 5.2a). A particle with a crystalline size of about 10 nm was observed in sample 5.1 (Fig. 5.2b). This particle has a fringe distance of 2.0 Å which is different from other typical fringe distances of this sample of 2.11 Å and 2.35 Å. The corresponding EDX analysis shows that it is a nickel-rich sulfide phase while the composition in other areas have a generally Ni:S atomic ratio of 1:1. But the identity of this phase could be heazlewoodite (Ni_3S_2).

Most fringes for sample 7.1 are within the range of 3.5 to 6 nm, many of them being rectangular shaped (Fig. 5.3).

In sample 9.1, the crystallites have relatively wider range of sizes from just above 2 nm to below 9 nm (Fig. 5.4). Some fringes tend to rectangular shapes with widths about 2 - 3 nm and lengths about 6 - 8 nm, while others look more isometric. The crystallite sizes estimated are in agreement of the results of the average particle sizes determined by small angle X-ray scattering (SAX) experiment. The analysis shows that the particle sizes for sample 9.1 average about 4.6 nm (unpublished data by Tim Wess 2005).

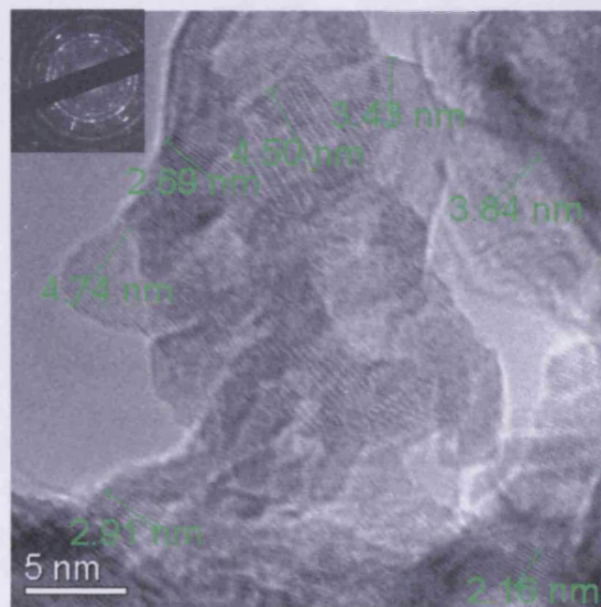


Figure 5.1 HRTEM images of sample 3.1 with crystalline sizes from 2.5 to 5 nm. The SAED pattern obtained from this area shows it is polycrystalline (obtained on JEOL 4000).

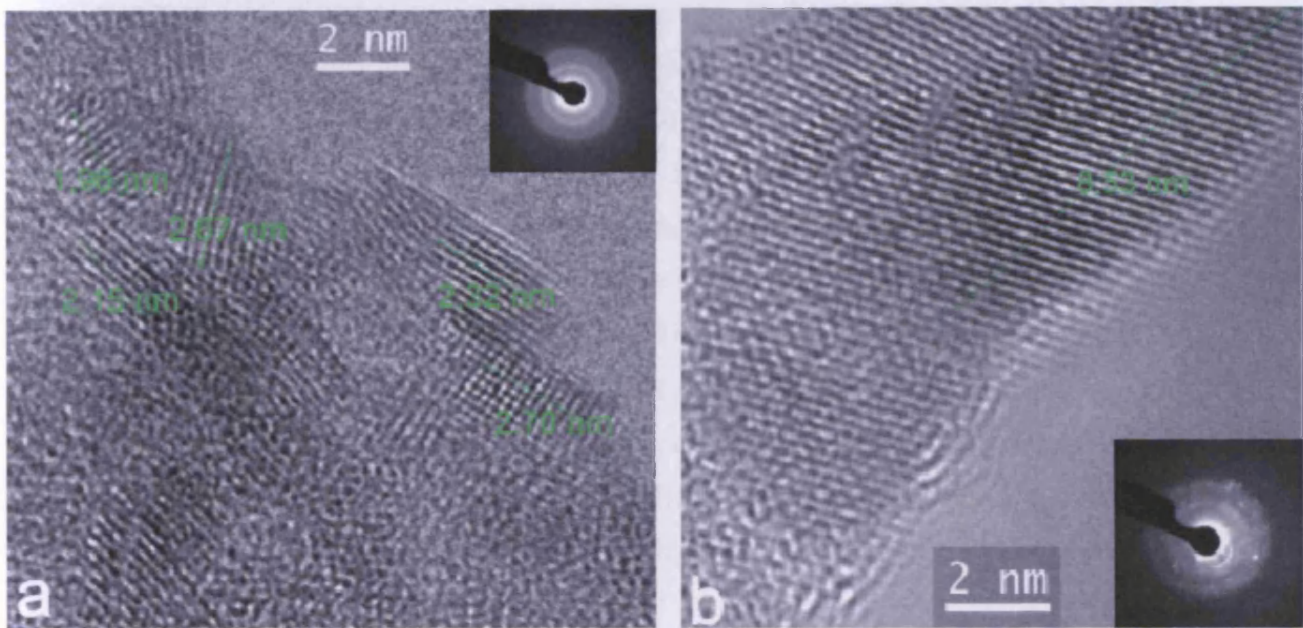


Figure 5.2 HRTEM images of sample 5.1. (a) 2 to 3 nm anhedral crystals. (b) A possible heazlewoodite phase with 10 nm in size and 2 nm fringe spacing. The SAED patterns (on the corners) show they are polycrystalline (obtained on JEOL 3000F).

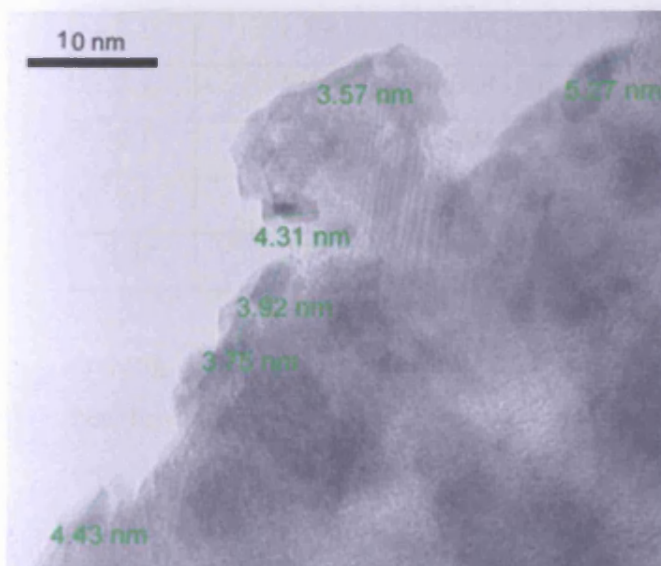


Figure 5.3 HRTEM image of sample 7.1 shows rectangular crystals 3.5 - 6.0 nm in size (obtained on JEOL 2010).

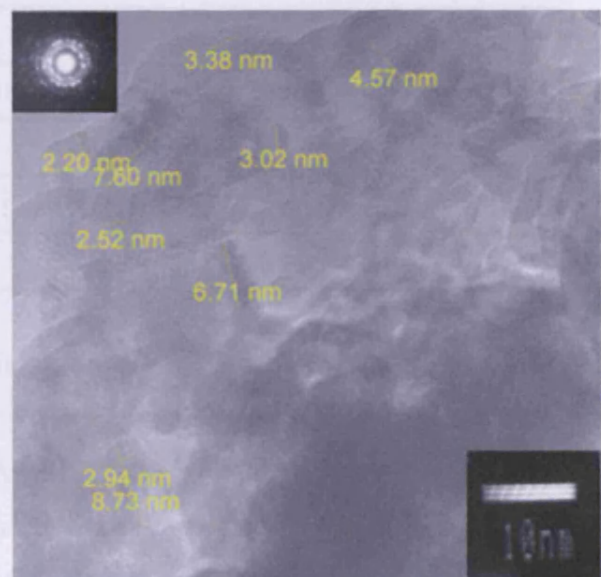


Figure 5.4 HRTEM image of sample 9.1 show various crystals 2 - 9nm in size. The SAED pattern on the corner shows the polycrystallinity of the material (obtained on JEOL 2010).

5.3.2 Fingerprints in the HRTEM images

Measurements of 22 fringe distances of samples 9.1 revealed that 12 out of 22 fringes have distance of 1.89 Å and 6 fringes have distance of 2.16 Å. The other four distances differing from these two values are 1.83, 2.12, 2.37 and 2.59 Å. These fringe measurements were made on sample 9.1 at 16 days and 26 days of age on different TEM instruments. Similar trend was also observed for samples 7.1 and 3.1 within 26 days age. An older 3.1 sample aged 241 days was also measured and similar results were obtained. However for sample 5.1, only 9 measurements were obtained on three particles of the same sample. 7 out of the 9 fringes measured have distances of 2.11 Å. The distances of the other two are 2.35 Å. In addition, as stated above, another large crystal with a fringe distance of 2.0 Å was observed in this sample. The results of the fringe distance measurements are summarized in Table 5.1. The preferred fringe distances shown in the HRTEM images are possibly due to a particular orientation of the nanoparticles on the grids which is attributed to a preferred particle shape.

Table 5.1 Summary of the measured fringe distances in HRTEM images. Data for sample 3.1* were collected after 241 days. Other measurements were made 26 days after precipitation.

<i>Sample</i>	<i>d spacing (Å)</i>	<i>STD</i>	<i>%</i>	<i>d spacing (Å)</i>	<i>STD</i>	<i>%</i>	<i>No. fringes measured</i>
3.1	1.89	0.002	55	2.16	0.006	40	20
7.1	1.89	0.004	50	2.21	0.003	25	12
9.1	1.89	0.003	59	2.22	0.007	36	22
5.1	2.11	0.005	78	2.35	0.002	22	9
3.1*	1.88	0.04	50	2.16	0.07	22	18

Among the possible phases in these materials, including nickel sulfides (millerite, heazlewoodite, polydymite and vaesite), nickel hydroxide, nickel oxide and metallic nickel, only millerite has d spacings close to both 1.89 Å and 2.20 Å corresponding to its (131) and (211) planes respectively. This may suggest millerite exist universally in the majority of the four samples prepared in the pH range from 3 to 9. The inconsistency of sample 5.1 may be an artefact because of the limited number of measurements made on this sample. This agrees with the results of chemical analysis that the atomic ratio of Ni and S in the material is about 1:1 (Chapter 3) and the XRPD analyses (Chapter 4). The shape of the nanoparticles may be platy in the direction perpendicular to (131) since the majority ($\geq 50\%$) of the particles lie in



this orientation; and the thickness in the direction perpendicular to (211) is the second shortest.

However, it is also possible that the samples are mixture of phases, i.e., the characteristic 1.9 and 2.2 Å correspond to two different phases. In this case, the possibilities are millerite with polydymite or vaesite since only millerite among the above candidate phases has d spacing near 2.2 Å. Millerite, vaesite and polydymite have d spacings near 1.9 Å, at 1.86 Å, 1.89 Å and 1.93 Å respectively. Other nickel sulfides such as godlevskite and α Ni₇S₆ with more complex stoichiometries and structures are not considered here since they have numerous reflections in this range which are not observed in these samples.

5.3.3 Specific surface area (SSA) estimation

Specific surface area was estimated as 558 m²/g based on the millerite structure according to the particle size observed on the HRTEM images. The shortest dimension which is perpendicular to the (131) planes is assumed as 2 nm and the area in the direction of (131) plane is averaged as a circular with 4 nm in diameter. This value is comparable to the SSA estimated for FeS precipitates in Ohfuji and Rickard (2006).

5.3.4 SAED structural characterization

Most SAED patterns obtained tend to be in ring shape produced from polycrystalline diffraction because of the small domain sizes of the materials. For many of them, “thick” rings covering ± 0.3 Å d spacings are observed. There are several reasons for the broadening of rings: (1) the size and shape of particles in real space influence the size and shape of diffraction spot in reciprocal space and cause the broadening (Putnis 1992); (2) diffraction domains are subject to deviation of incident orientation of electron beam away from the zone axis. In this case, the real d spacing of the material should be close to the mean of the calculated d spacing range; and (3) the defects and the effect of lattice contraction and expansion in the nanocrystal structure make the d spacings deviate from ideal bulk phases. For polycrystalline material, if the structural defect is not universal for all crystals the rings are broadened. Some randomly dispersed diffraction spots appearing on the SAED patterns suggest dynamic scattering of the electrons or disorder in the specimens. The measured d spacings compared with the models are displayed in Figs. 5.5 - 5.8. The chosen models include all the known structure of nickel sulfides and other possible phases including NiO (bunsenite) and Ni(OH)₂ (theophrastite) and metallic nickel. The structural parameters of the

models are those of bulk phases. Obviously, the d spacings of nanoparticles may differ from the bulk phases to some extent (Waychunas 2001).

SAED data of sample 3.1 (Fig. 5.5) show that older samples (241 days) have thinner and thus better defined rings than those of the younger samples aging about 25 and 30 days. This is due to the growth of nanocrystals during aging. Image 1030 was collected on sample 3.1 at age of 241 days. It displays several well defined lines and at $d = 1.63 \text{ \AA}$, it shows hexagonal arranged reciprocal lattice points. The d spacings calculated from the rings correspond to Ni_3S_2 (heazlewoodite) structure. Image 1046, also from sample 3.1 at 241 days old, looks like millerite pattern. The results on other sites give broad areas that could be assigned to either millerite or polydymite. Perhaps millerite is slightly favoured because it has several lines distributed in the broad area between 3.0 and 2.3 \AA while polydymite only has two near the two ends. However phase identification for patterns with broad area is generally poor with large uncertainties.

The SAED patterns of sample 5.1 are broad (Fig. 5.6). They were all collected 25 days after precipitation. Analysis p2s1 appears to match heazlewoodite a little. Millerite appears to be a better candidate for the other patterns since it possesses several lines in the broad area between 2.9 and 2.4 \AA .

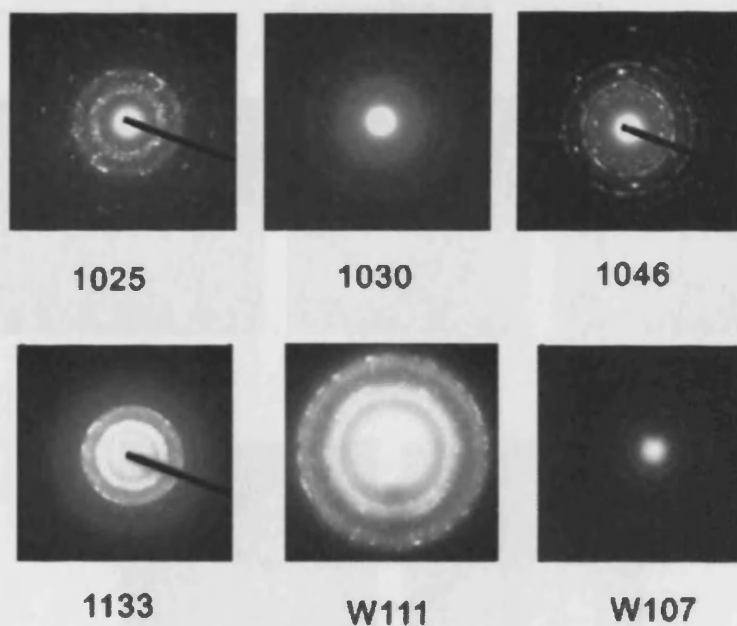
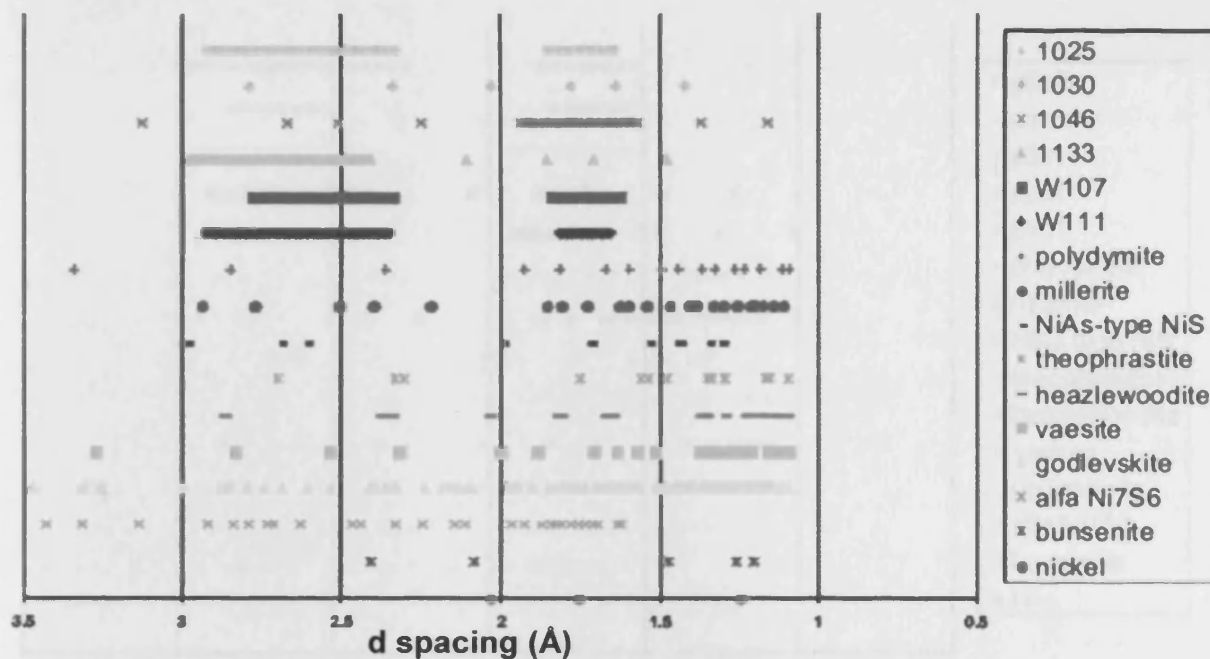


Figure 5.5 SAED analyses of sample 3.1. Images 1025, 1030 and 1046 were collected 241 days after precipitation; image 1133 31 days after precipitation; and images W107 and W111 25 days after precipitation. In the upper graph, the d spacings are calculated from experimental data and are compared with the values of models underneath. It can be seen that image 1030 is heazlewoodite and other images appear to be millerite. The corresponding experimental SAED patterns are displayed under the calculated graph.

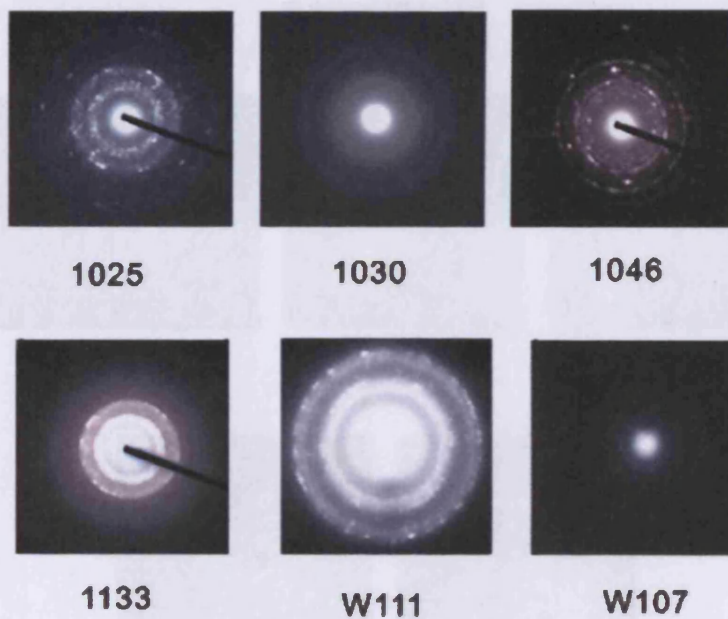
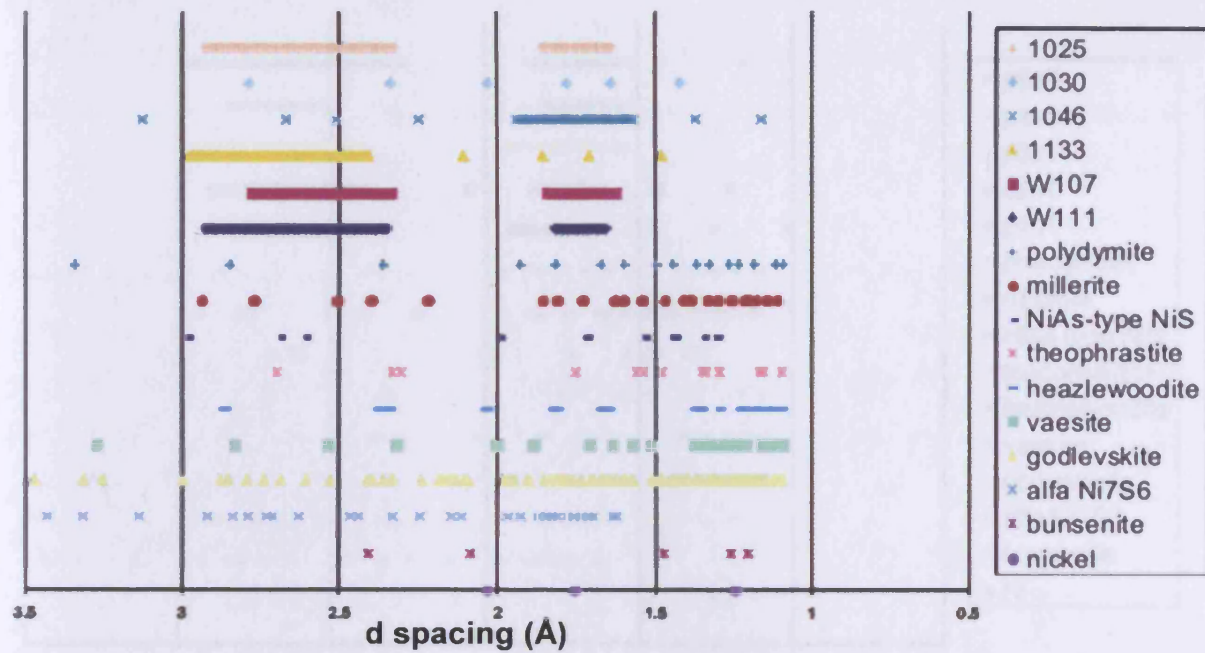


Figure 5.5 SAED analyses of sample 3.1. Images 1025, 1030 and 1046 were collected 241 days after precipitation; image 1133 31 days after precipitation; and images W107 and W111 25 days after precipitation. In the upper graph, the d spacings are calculated from experimental data and are compared with the values of models underneath. It can be seen that image 1030 is heazlewoodite and other images appear to be millerite. The corresponding experimental SAED patterns are displayed under the calculated graph.

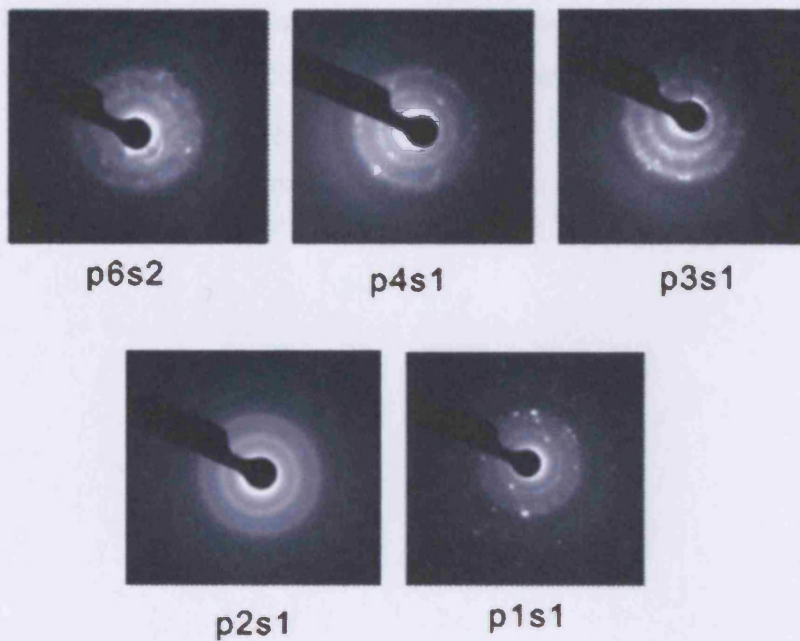
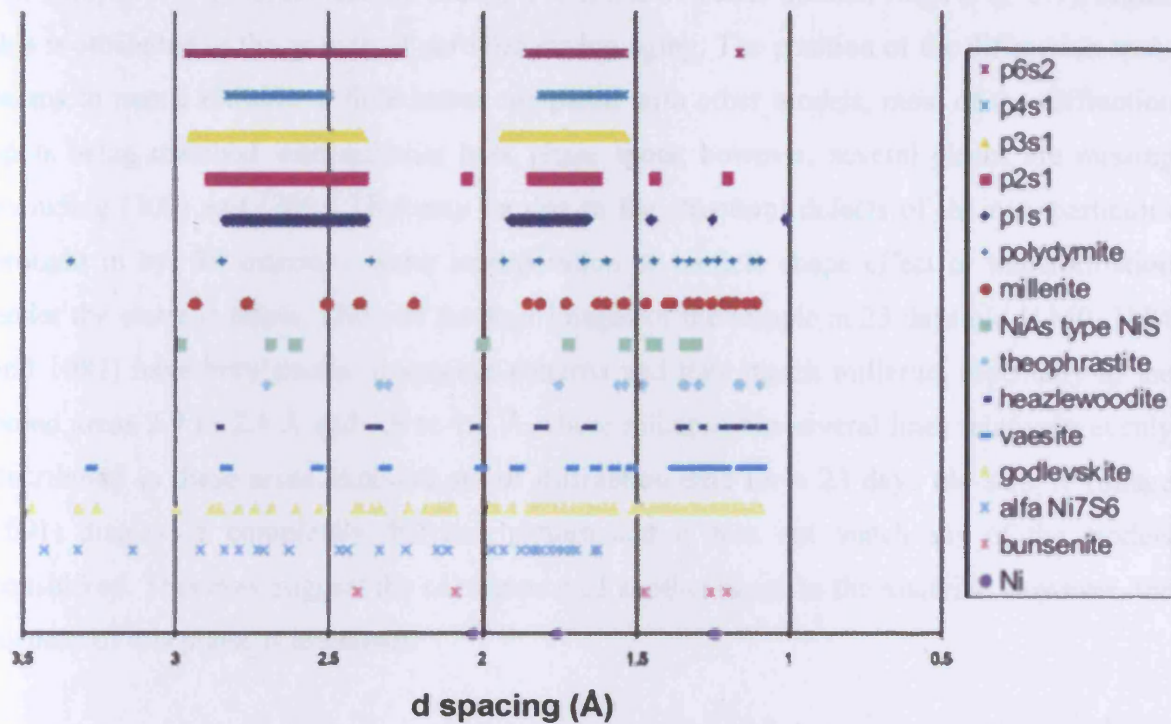


Figure 5.6 SAED analyses of sample 5.1. All data were collected 25 days after precipitation. In the upper graph, the d spacings are calculated from experimental data and are compared with the values of models underneath. The material appears to be heazlewoodite and millerite. The corresponding experimental SAED data are also displayed.

For sample 7.1, the older sample (image 1150) shows better defined rings (Fig. 5.7). Again this is attributed to the growth of particles during aging. The position of the diffraction spots seems to match millerite a little better compared with other models, most of the diffraction spots being matched with millerite bulk phase spots; however, several planes are missing including (300) and (200). This may be due to the structural defects of the nanoparticles brought in by, for example, water incorporation or particle shape effect or transformation under the electron beam. Three of the four images of the sample at 23 days old (1140, 1084 and 1082) have very similar d spacing patterns and they match millerite, especially in the broad areas 2.9 to 2.4 Å and 1.9 to 1.7 Å where millerite has several lines relatively evenly distributed in these areas. Another set of diffraction data for a 23 days old sample (image 1091) displays a completely different pattern and it does not match any of the models considered. This may suggest the coexistence of another phase in the material. However, the identity of this phase is unknown.

In the SAED patterns of sample 9.1 (Fig. 5.8), images 1059 and 1061 appear to match the theophrastite. For images 1066 and 1017, heazlewoodite and millerite may be slightly better fitted. However, these preferences are rather subtle and the fits are poor in general. KD2007 appears to fit heazlewoodite structure, but the match is very poor too. If consider two phases for one diffraction data, many possible pairs could be resulted.

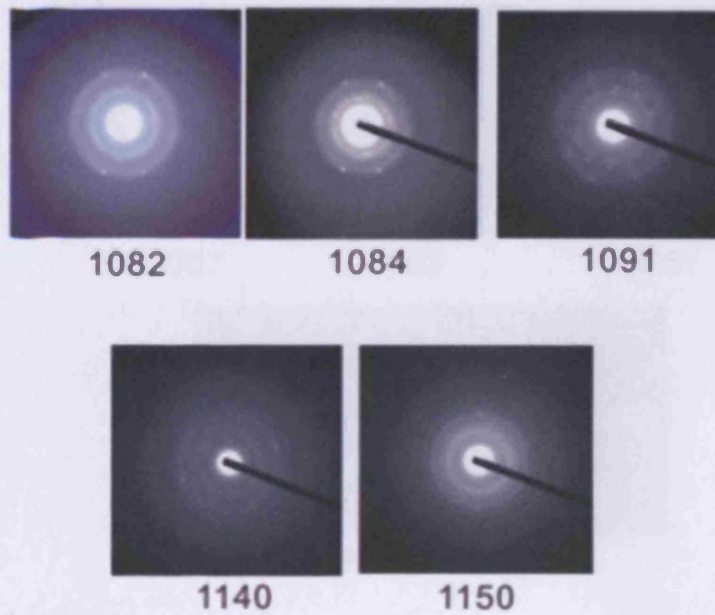
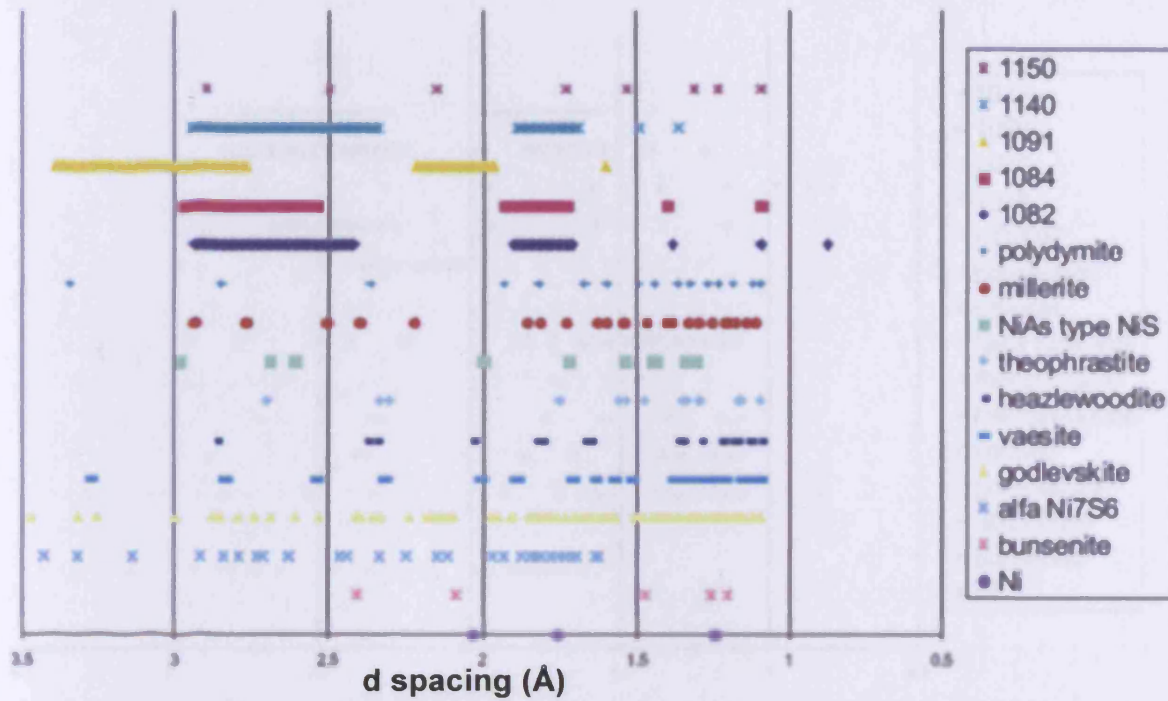


Figure 5.7 SAED analyses of sample 7.1. Images 1082, 1084, 1091 and 1140 were collected 23 days after precipitation. Image 1150 was collected 245 days after precipitation and shows enhanced crystallinity. In the upper graph, the d spacings are calculated from experimental data and are compared with the values of models underneath. It appears that all the patterns, except for the unknown 1091, are millerite. The corresponding experimental SAED patterns are also displayed.

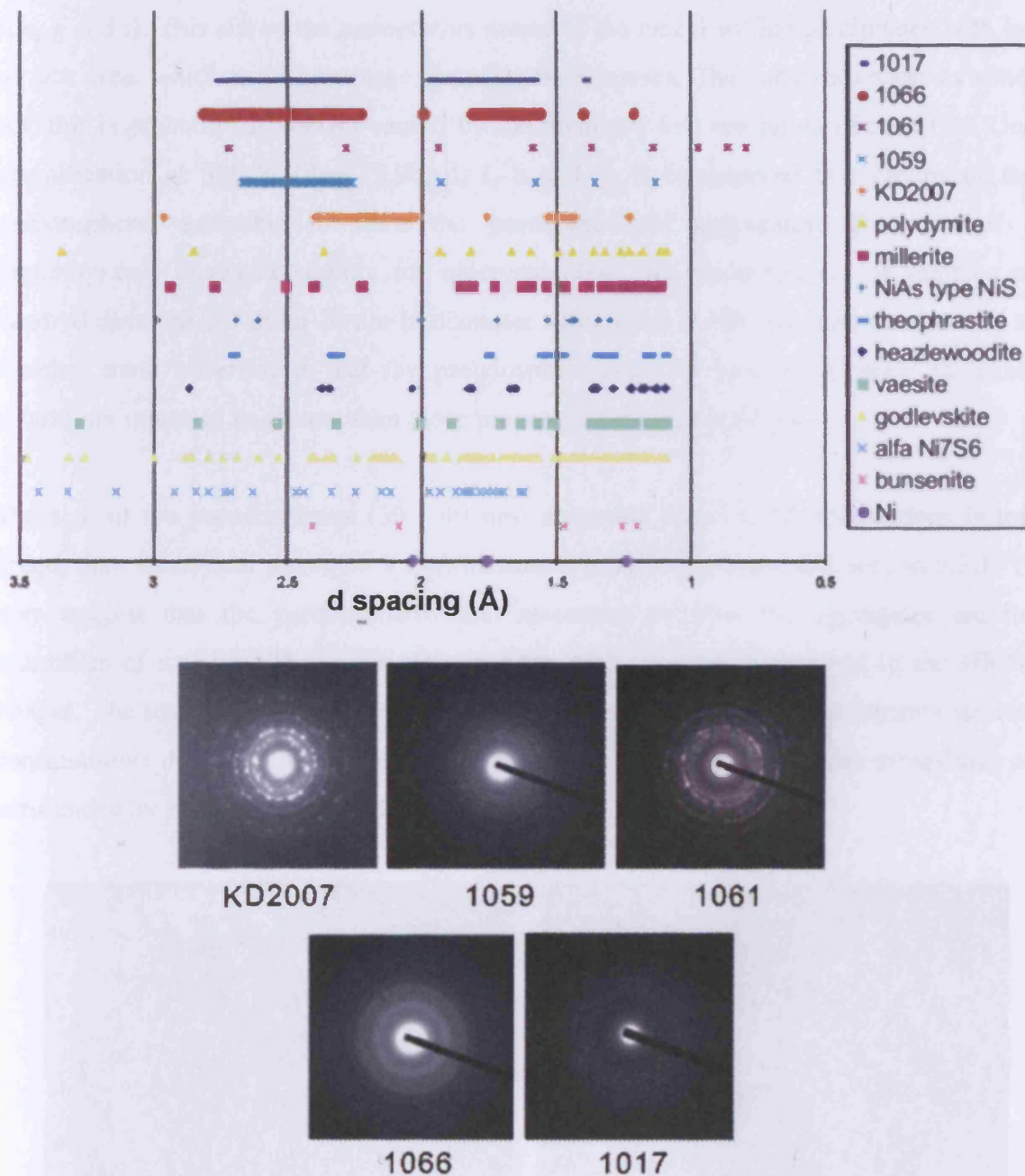
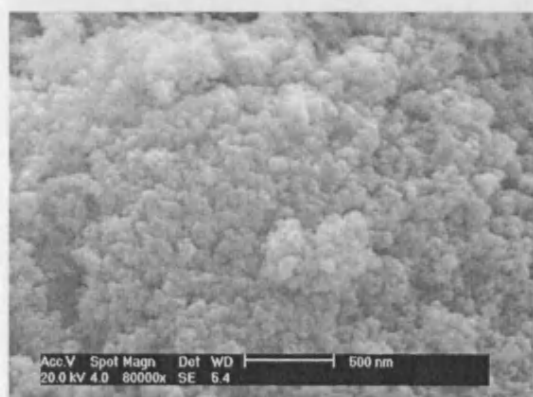


Figure 5.8 SAED analyses of sample 9.1. Images 1059 and 1061 were collected 26 days after precipitation, image 1017, 242 days after precipitated and image KD2007, 16 days after precipitation. In the upper graph, the d spacings are calculated from experimental data and are compared with the values of models underneath. The calculated d spacings are not readily assigned to any specific Ni phases. Their corresponding experimental SAED patterns are also displayed.

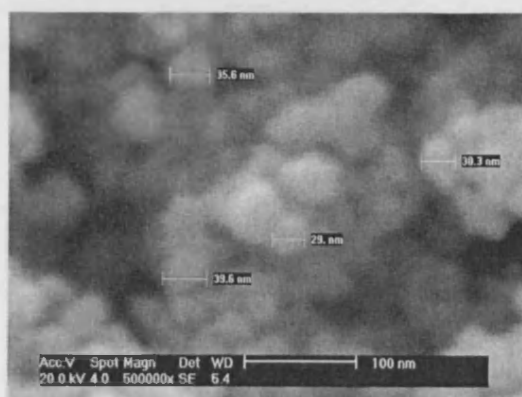
5.3.5 SEM observations

SEM images at 80K magnification display a rough surface for the NiS precipitates (Fig. 5.9a, c, e, g and i). This shows the nanoporous nature of the nickel sulfide precipitates with large surface area, which is an advantage for catalytic purposes. The particles appear as spheres but, this is probably an artefact caused by the relatively low resolution of the SEM. Under magnification at 500 K (Figs. 5.9b, d, f, h and j), it is observed that groups of these pseudospheres assemble to form the pseudospherical aggregates. The size of the pseudospheres increases slightly for older samples. The pseudospheres of samples at a hundred days old are about 30 nm in diameter while those > 300 days old are about 40 nm. Another trend observed is that the pseudosphere sizes of samples prepared in alkaline conditions appear to be greater than those prepared in acidic conditions.

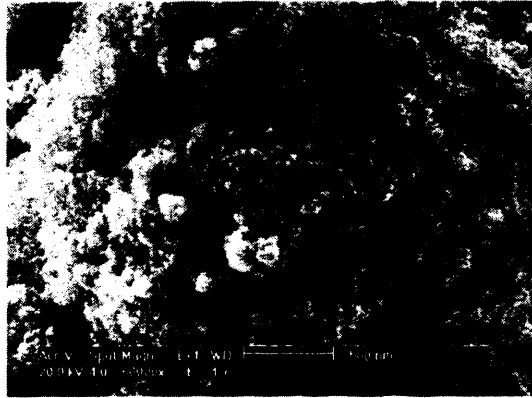
The size of the pseudospheres (30 - 40 nm) measured under SEM observations is much bigger than the crystal sizes (2 - 9 nm) measured in HRTEM images in section 5.3.1. This may suggest that the pseudospheres that assembles to form the aggregates are itself assemblies of smaller NiS nanocrystals in sizes of 2 - 9 nm as observed in the HRTEM images. The structure of the nanocrystals is considered to develop the core-mantle structural configuration described in Chapter 3, which is a 1 nm NiS (millerite) crystalline core surrounded by a defective and hydrated mantle phase.



a. Sample 3.1 at 111 days old (X 80 K)



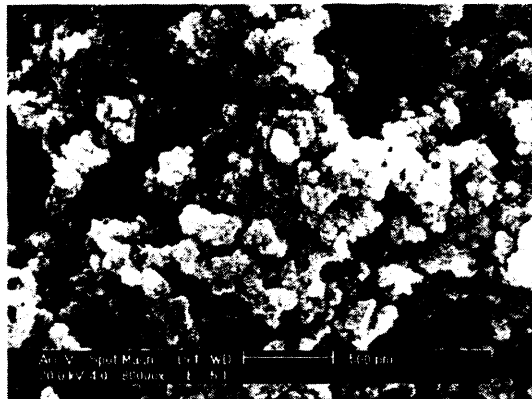
b. Sample 3.1 at 111 days old (X 500 K)



c. Sample 3.1 at 328 days old (X 80 K)



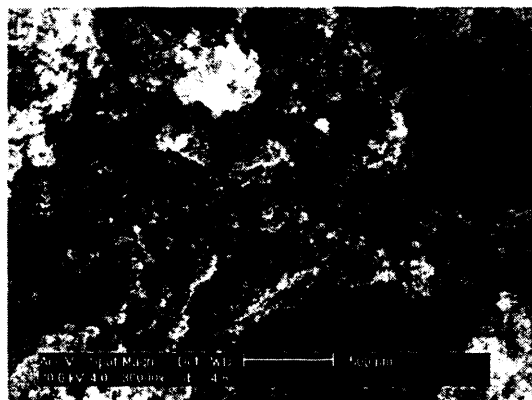
d. Sample 3.1 at 328 days old (X 500 K)



e. Sample 7.1 at 104 days old (X 80 K)



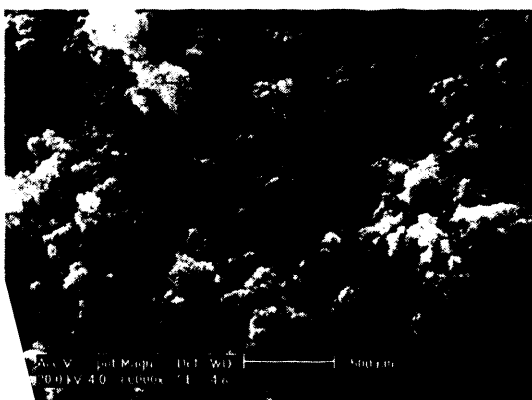
f. Sample 7.1 at 104 days old (X 500 K)



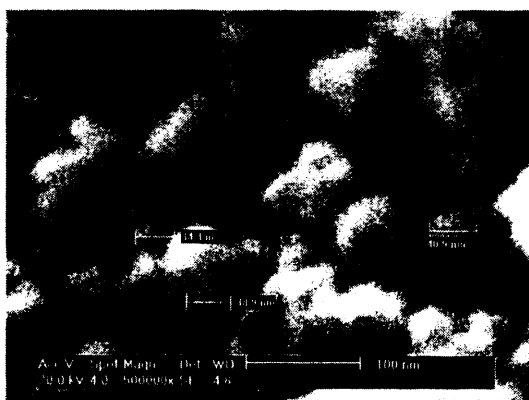
g. Sample 9.1 at 109 days old (X 80 K)



h. Sample 9.1 at 109 days old (X 500 K)



i. Sample 9.1 at 326 days old (X 80 K)



j. Sample 9.1 at 326 days old (X 500 K)

5.9 SEM images of the NiS precipitates at magnifications 80 K and 500 K. It shows the porous nature of the material. The nanoparticles assemble to 20 - 40 nm

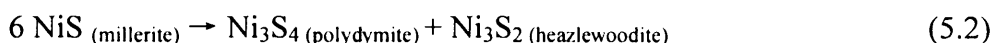
5.3.6 Chemical analyses

EDX analyses show that the samples consist of nickel and sulfur. The atomic ratios are about 1:1 for most samples. However, due to the analytical uncertainty in the measurements, the possibility of the coexistence of nickel sulfide phases with other stoichiometries as minority phases cannot be excluded, especially for samples 5.1 and 7.1 where some nickel rich spots were analysed.

5.4 Discussion

HRTEM and SAED data support that, the majority of the samples consist of nanoparticulate millerite, which is consistent with the structural characterization of these materials by X-ray scattering techniques presented in Chapter 4. The problem with attempting structural assignments with the SAED analyses is that the data collected is polycrystalline. The nanoparticles were too small to give robust single crystal electron diffraction data. This means that the electron diffraction data is collected from a number of particles and becomes an average of particles with various sizes, defects and even including different phases. Except for one SAED analysis (1030), collected from one site of sample 3.1 aged for 241 days which can be assigned to Ni_3S_2 (heazlewoodite) with some confidence, definitive assignment of the SAED patterns to phases is relatively rare in this system, although millerite seems to generally give a better fit. In addition, electron beam bombardment may cause phase transformation. This situation is compounded by the incorporation of water in the structure.

The detection of Ni_3S_2 (heazlewoodite) from one SAED pattern and one suspicious area in the HRTEM image of samples formed at low pH is very interesting. XRPD results show that the initial structure of the precipitates is millerite-like and the transformation to well crystalline polydymite occurs within 16 days in materials formed in low pH (Chapter 4). The detection of Ni_3S_2 confirms that the transformation from NiS (millerite) to Ni_3S_4 (polydymite) follows reaction (5.2):



This is consistent with the chemical analysis that, after the transformation, the overall composition of the material is still close to Ni:S = 1:1. The Ni_3S_2 crystallinity is not as good

as Ni_3S_4 so it does not appear obviously on the XRPD patterns. But Ni_3S_2 formation is supported by a small reflection on the XRPD pattern of 3.1 sample at 241 days old which appears to correspond to the (200) planes of heazlewoodite (Chapter 4).

In the analogous FeS system, a similar solid state transformation is the FeS (mackinawite) transformation to Fe_3S_4 (greigite). Rickard and Luther (2006) discussed the oxidation process in the FeS system and showed that the reaction mechanism is not clear. The Ni_3S_2 formation accompanied with Ni_3S_4 production could shed light on the FeS situation. There might be a formation of an iron-rich sulfide phase in companion with the reaction from FeS to Fe_3S_4 , although the iron-rich sulfide phase is not yet known. This suggestion also agrees with the experimental observations that the Fe:S atomic ratio after the transformation of mackinawite to greigite remains around 1 (Lennie et al. 1995).

Zhang (2003) reported that for 3 nm nanocrystalline ZnS material, the distortion due to the cumulative effects of water bonding on the surface affects at least four atomic layers, approximately 0.8 nm towards the inner structure. However, the addition of water to nanoparticulate ZnS did not result in size change in their TEM observations. According to their molecular dynamics calculations the ZnS nanoparticles, although highly disordered and hydrated, have a crystalline core which is unaffected by water bonding. A similar model was developed for the NiS precipitates in Chapter 3. The model includes a well crystalline NiS (millerite) core with about 1 nm size and a mantle phase containing water species and significant disorder. The crystalline NiS (millerite) core is not obviously distinguished from the mantle phase under the HRTEM images. The fringe images are considered to be the whole nanocrystal including the core and mantle phases. However, the core and mantle phases may be distinguished in the SAED patterns. The well defined thin lines are the reflections from the crystalline NiS core and the broadness of the lines and the wispy features were produced by the defective mantle phase. Oxygen and hydrogen have much smaller structural factors compared with Ni and S, so under TEM observations, what we see are mainly the nickel sulfide configuration.

For NiS sample 9.1, which was prepared in alkaline conditions, both NiS (millerite) and $\text{Ni}(\text{OH})_2$ (theophrastite) are apparently indicated in this material from SAED data. However, it is unlikely that this sample is a simple mixture of the two discrete phases. In the core-mantle structural mode discussed above, the hydroxyl group may only take the positions in

the outer layer where considerable disorder presents. The Ni(OH)₂ structural component is probably contained in this highly defective area.

5.5 Conclusions

Nickel sulfide aqueous precipitates under standard temperature and pressure are not amorphous but nanocrystalline with crystal sizes between 2 and 9 nm. The HRTEM results demonstrate that the quasi-amorphous form of the material, as suggested by XRPD, is caused by its nanoparticulate nature. The dominant phase displays a millerite-like structure. The material is highly defective. Ni₃S₂ (heazlewoodite) was detected on samples from acid solutions, which explains the reduction product of the transformation from NiS (millerite) to Ni₃S₄ (polydymite). The particle shape is indeterminate, but appears to be platy with the shortest thickness perpendicular to the direction of (131) planes of millerite. With ageing the material tends to form larger crystals and other more stable phases, like polydymite. The specific surface area is estimated as 558 m²/g based on the averaging 4 nm size in HRTEM images and an assumption of 2 nm thickness perpendicular to the observed direction. The NiS nanoparticulates aggregate to pseudospherical particles with sizes up to 40 nm which is highly porous and maintains a large surface area ideally suited to catalysis.

Acknowledgements

I thank Hiroaki Ohfuji for his help with using the TEM ~~experiments~~^{instrument} at Ehime University. Data collection at the University of Oxford was assisted by Zhongwen Yao. Helpful comment from Zhongfu Zhou on this Chapter is appreciated.

Chapter 6

Prebiotic Carbon Fixation by FeS/NiS in the Formaldehyde World

Figures

Figure 6.1 A proposed mechanism for H_2CO reduction and condensation by Fe/Ni sulfides and H_2S .

Table

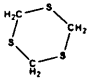
Table 6.1 Summary of $\text{H}_2\text{CO} + \text{H}_2\text{S}$ batch experiments at 25 °C.

Table 6.2 Experimental investigations of the FeS / H_2S / H_2CO system at pH 6.

Table 6.2 Experimental investigations of the FeS / H_2S / H_2CO system at pH 6.

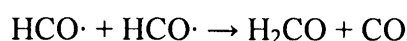
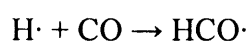
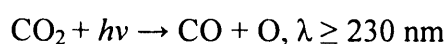
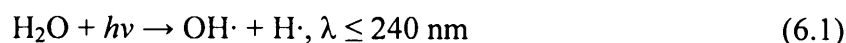
Table 6.4 Investigations of the pH effect on FeS or NiS / trithiane system.

Abstract

Iron and nickel sulfides have the capacity to catalyse carbon fixation from inorganic or simple organic carbon source. These reactions may have been involved in the prebiotic processes that resulted in the origins of life. Formaldehyde (H_2CO) is a likely carbon source present in elevated concentrations in the Hadean Earth. I refer to this environment as the formaldehyde world. An investigation of the system of H_2CO / trithiane, , hydrogen sulfide (H_2S) and iron and nickel sulfides under ambient conditions in aqueous solutions were conducted in this study. Experiments were carried out with a variation of temperature, reaction time, metal sulfide presence and pH. No obvious catalytic effect of Fe/Ni sulfides on the H_2CO condensation or trithiane reduction is found. Several advanced C-C compounds were identified but were probably from a contaminant source. The formation of elemental sulfur seems to be the result of an oxidation process; however, no obvious reduction product was detected. Trithiane, the main product of the reaction between H_2CO and H_2S is found to function similarly to aldehydic carbonyls in suppressing pyrite formation and promote greigite formation. By analogy with the carbonyl reaction, trithiane suppresses the formation of aqueous iron sulfide clusters which are key intermediaries in the formation of pyrite. The presence of thio-organic compounds provides a further cause for greigite formation in sedimentary systems. Due to the biochemical potential of the greigite structure as functional centres of iron-sulfur proteins, this reaction adds further information to the iron-sulfur world hypothesis for the origins of life.

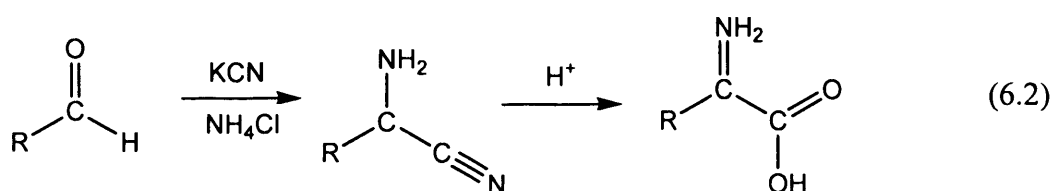
6.1 Introduction

H_2CO was synthesized naturally in the prebiotic atmosphere from CO_2 and H_2O by the enhanced Hadean ultraviolet radiation (Pinto et al. 1980):



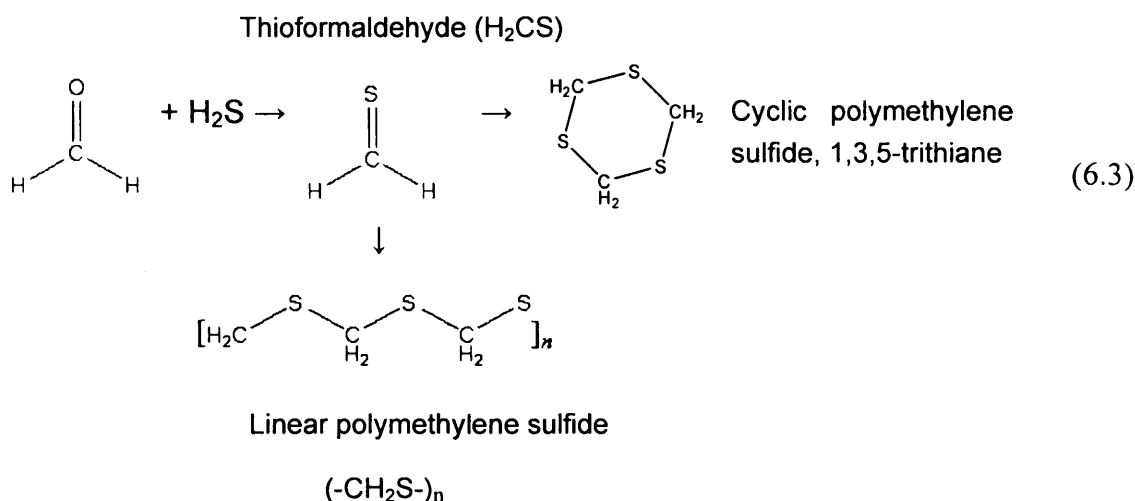
H₂CO is also detected in contemporary sea water (Largiuni et al. 2005). It is recognized as a potential carbon source for prebiotic reactions that led to the origin of life (Feng et al. 2008; Morooka et al. 2005). Schulte and Shock (1993) calculated the thermodynamic properties of aldehydes under hydrothermal conditions, suggesting that aldehydes may have been involved in the transition between hydrocarbons to carboxylic acids in the hydrothermal system. I refer to the time of enhanced natural H₂CO concentrations in the atmosphere and oceans of this planet as the formaldehyde world.

In a calcium hydroxide suspension, H₂CO rapidly undergoes condensation process resulting in a series of carbohydrates which include a fraction of ribose (Zubay 2000, p 211). In this reaction (the formose reaction), glycolaldehyde CH₂OHCHO is the first condensed product from two H₂CO molecules. It has been shown that glycolaldehyde can catalyse the incorporation of H₂CO into sugars. However the strongly alkaline reaction conditions (pH > 11.0) does not favour the survival of aldopentoses which is the form of ribose in RNA. Lead also catalyzes the conversion of H₂CO to sugars (Zubay 1996). In addition, aldehyde is also a pre-requisite for the Strecker synthesis of amino acid. In this process, aldehyde is condensed by reaction with NH₄Cl with presence of KCN. The product is subsequently hydrolysed to amino acid. The process is:



The present study reports an investigation of the reactions among H₂CO, iron and nickel sulfides and H₂S. It mirrors to some extent conditions which may have been encountered naturally in the iron-sulfur world, which has been suggested to have been involved in the prebiotic synthesis of biologically-significant molecules (Corliss et al. 1979; Russell and Hall 1997; Wächtershauser 1992).

H₂CO reacts rapidly with H₂S to produce cyclic and linear polymethylene sulfides. 1,3,5-trithiane is one common type of the cyclic polymethylene sulfides.



This reaction was first found by Hofmann in 1868. Thioformaldehyde (H_2CS) is the intermediate product of the reaction between H_2CO and H_2S in acid condition. It is highly reactive and rapidly condenses into polymethylene sulfides. A 92 - 94% yield of trithiane was once reported when H_2S passed through a solution of H_2CO in concentrated HCl solution with a variety of other products such as $(\text{CH}_2\text{S})_3\text{CH}_2\text{O}$ (Campaigne 1946). The extreme unstable H_2CS is reactive in a variety of condensation and replacement reactions (Usov et al. 1990). Due to this reaction capacity, H_2CS may play an important role for the carbon condensation in the prebiotic reactions.

Schoonen et al. (1999) showed that CO_2 reduction via C-S compounds is more favoured than direct reduction to HCOOH because of the lower LUMO (lowest unoccupied molecular orbital) energy levels for CS_2 and OCS . Huber and Wachtershauser reported the condensation of CO to acetic acid (Huber and Wächtershauser 1997) or peptides (Huber and Wächtershauser 1998) in the presence of a slurry of undefined iron and nickel sulfide precipitates and H_2S (or CH_3SH) at 100°C . They proposed that CH_3SH was an important intermediate in this reaction. In addition, OCS was also reported to mediate the formation of peptides from amino acids at room temperature (Leman et al. 2004). This reaction was accelerated in the presence of metal ions [e.g. Fe(III) , Cd(II) , Zn(II)], oxidizing agents or alkylating agents.

It is found that aqueous FeS clusters react with aldehydic carbonyls to suppress the formation of pyrite (Rickard et al. 2001). The result was interesting in that the mechanism appeared to

be an interaction of FeS clusters with aldehydic carbonyls since the aldehyde could be recovered after the reaction. The reaction was faster and more complete with smaller aldehydes such as H₂CO. Cody et al. (2000) suggested that carbonyl FeS clusters are formed by reactions of FeS, alkyl thiols and CO at 250 °C and elevated pressures. They detected a series of interesting products including 1-decanoic acid revealing a carbonylation process, 1-methyl-nonyl sulfide, revealing CO reduction to methyl and some nonyl-containing organometallic phases. The result suggests that metal sulfides interact with H₂CO and therefore could be instrumental in catalysing C-C bond formation from a H₂CO starting product.

Greigite (Fe₃S₄) is interesting geochemically and biochemically because it is structurally analogous with the active centre of the enzyme that catalyses acetate synthesis from CO₂ and methyl group. The Fe₂S₂ rhombs assembling to Fe₄S₄ cluster in greigite is also the basic component for ferredoxins, the primitive Fe-S electron transfer proteins (Russell et al. 2005). In Russell's FeS membrane model under the hydrothermal circumstances, the released H₂ was adsorbed to the Fe₄S₄ cubane of greigite and was activated to hydrogen atom which attacks CO₂ or methyl to reduce them to CO and water. Greigite is also a major constituent of magnetotactic bacteria that orientate themselves along the Earth magnetic field with the biomineralization of greigite or magnetite in their bodies. Therefore, the greigite formation in hydrothermal conditions is of interest in the origin-of-life scenario.

I designed a series of experiments to explore the reactions among H₂CO, H₂S and Fe/Ni sulfides. A mechanism for the carbon fixation reaction in this system is proposed as follows: the majority of reaction products between H₂CO and H₂S go to polymethylene sulfides rapidly via condensation of the intermediate HCHS. For HCHS which does not condense and unreacted H₂CO, two possible routes may occur: (1) the sulfur atom of SCH₂ is attacked by metal centres in aqueous clusters or on the surface of sulfides solid, followed by reductive desulfuration of metal sulfide-bonded thioorganic constituent, forming C=C bonded compounds from two detached thioorganic constituents; and (2) the sulfur atom of SCH₂ is first attacked by metal centres in the aqueous clusters or on the surface of metal sulfides, followed by another nucleophilic attack of another free highly active HCHS at the carbon

atom of the metal sulfide-bonded thioorganic constituent, forming a C=C bond. Finally the bonded double carbon thioorganic desulfurates from the metal sulfide surface and a molecule of ethylene is formed. The proposal is depicted in Fig. 6.1.

The aim of the present work was to investigate the above system and test the hypothesis of carbon fixation in the formaldehyde world in the presence of iron and nickel sulfides and H_2S .

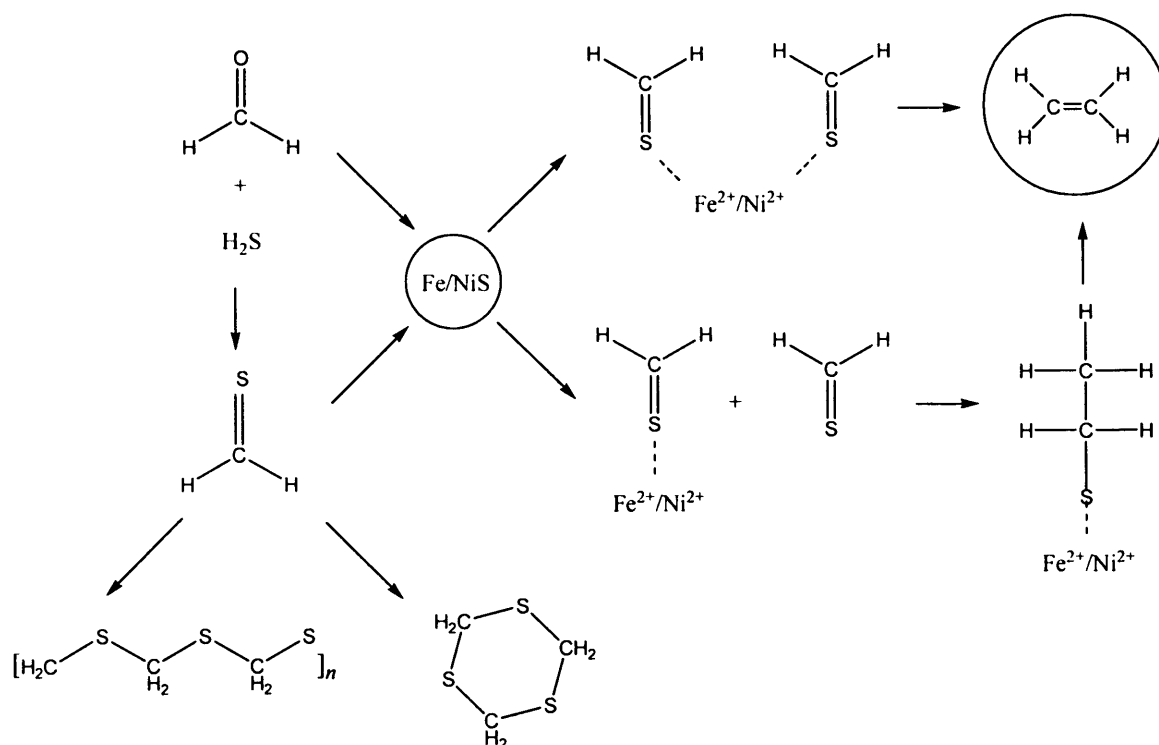


Figure 6.1 A proposed mechanism for H_2CO reduction and condensation by Fe/Ni sulfides and H_2S .

6.2 Methods

6.2.1 Metal sulfides preparation

Metal sulfides were precipitated at various pH. Analytical grade $(\text{NH}_4)_2\text{Fe}(\text{SO}_4)\cdot 6\text{H}_2\text{O}$, $\text{NiSO}_4\cdot 7\text{H}_2\text{O}$, and $\text{Na}_2\text{S}\cdot 9\text{H}_2\text{O}$ were used as starting materials in the synthetic reactions. All reagents were made up in deionised 18.2 $\text{M}\Omega$ cm water (DW, MilliQ) distilled water, which was deoxygenated by bubbling with oxygen-free nitrogen for at least 45 minutes. FeS was

synthesized following Rickard (1997) by pouring 100 mL $(\text{NH}_4)_2\text{Fe}(\text{SO}_4)\cdot 6\text{H}_2\text{O}$ solution (0.6 M) to 100 mL $\text{Na}_2\text{S}\cdot 9\text{H}_2\text{O}$ solution (0.6 M). The pH of the precipitation was unadjusted. For NiS, buffer solutions were used to adjust the pH of the precipitation. pH 3 buffer was prepared by mixing potassium hydrogen phthalate and HCl. pH 5, 7 and 9 buffer powders were from Hydrion™ and are composed of acetate, phosphate and carbonate respectively. For pH 3 and 5, nickel sulfate solutions were buffered; for pH 7 and 9, sodium sulfide solutions were buffered. Precipitations were conducted by dropwise addition of one solution (0.1 M, 50 mL) into a stirred and buffered solution (0.05 M, 100 mL). NiS was also prepared without pH adjustment to avoid the possible contamination from the buffer composition. FeNiS_2 was prepared by mixing 100 mL solution containing 0.1 M $(\text{NH}_4)_2\text{Fe}(\text{SO}_4)\cdot 6\text{H}_2\text{O}$ and 0.1 M $\text{NiSO}_4\cdot 7\text{H}_2\text{O}$ with 100 mL 0.2 M $\text{Na}_2\text{S}\cdot 9\text{H}_2\text{O}$ solution with pH unadjusted. Products were washed, filtered and freeze dried for at least 48 hours, then ground into fine powders. Samples were stored in solid state in the anoxic chamber before analysis. All precipitation, filtration and storage were performed in a N_2 -filled MBraun Labmaster 130 anoxic chamber maintained at < 2 ppm O_2 level. The synthetic materials were used within 50 days after they were precipitated. The preparation procedure for metal sulfides is similar to those formed in the experiments of Huber and Wächtershauser (1997).

6.2.2 Source of other reagents used

Ti(III) citrate was used as a reducing agent in some experiments following Rickard et al. (2001). The Ti(III) citrate was prepared by adding 10 mL 15% TiCl_3 to 50 mL sodium citrate and neutralizing with saturated Na_2CO_3 to 100 mL. In order to check the possible catalytic effect of titanium ion, titanium standard solutions (used in ICP analysis) were used to replace titanium citrate in some experiments. H_2S gas was purchased from VWR™ with purity above 99.5%. Most reactions were taken place in pH 6 phosphate buffer (Hydrion™). Some experiments were done in pH 7 and 9 using the buffer described above for nickel sulfide precipitation. 1, 3, 5 trithiane powder with 97 % purity (from Sigma-Aldrich) was used instead of H_2CO or H_2CO and H_2S in some experiments.

6.2.3 Reaction procedure

For the reaction procedure, methods of Rickard et al. (2001) were followed. The reactions were carried out in sealed glass ampoules. The addition and extraction of reactants and products were performed in the N₂-filled anoxic chamber and on a manifold system that permit oxygen-free access. For a typical experiment, weighted metal sulfide (and trithiane powder if needed) was transferred into the ampoule. Then solutions of H₂CO and buffer were pipetted into the ampoule. The ampoule was then connected to the manifold with a valve closed at the opening. H₂S gas was added when the valve was opened and the system was adjusted to under vacuum to allow the H₂S gas to fill in the ampoule. The ampoule was sealed by heating the neck of the glass ampoule.

6.2.4 Products characterization

Solid products were collected by filtration and freeze drying. They were characterized by X-ray powder diffraction (XRPD) with a Philips 1710 and Cu K α radiation. Liquid phases were analysed by gas chromatography - mass spectrometry (GC - MS) and proton nuclear magnetic resonance (¹H NMR).

Three GC instruments, a Varian EZ-GRIP, an Agilent 6890N and a Perkin Elmer Autosystem were used in this study. The first two connected with mass spectrometer were used to identify the products in the resultant liquids phase and the Perkin Elmer instrument was used to detect if molecular hydrogen were produced in the gas phase. This helps understand the systems where FeS and H₂S are involved since molecular hydrogen is the product of the direct reaction of FeS and H₂S at higher temperatures (Rickard 1997). For liquid analyses, the solid phase was eliminated by centrifuge and the liquid was pipetted into a 10 mL QuickfitTM tube. For analyses done on Varian EZ-GRIP, the solid phase microextraction extractor and fibre (SupelcoTM) was used. The silica fibre was bounded with a 100 μ m film of polydimethylsiloxane (PDMS). The sample was prepared by absorbing the sample on the fibre by placing it into the stirred sample-contained liquid phase for 10 minutes. After the sample absorption, the fibre was inserted into the instrument at a port temperature 220 °C. The column temperature increased from 30 °C to 250 °C at a rate of 5 °C/min. The column

was Factor Four™ VF-23ms (30 m x 0.25 mm x 0.25 μm, Part number: CP8822). The software used in this system was MassLab V1.4 package. Because of the worry that high port temperature at 220 °C for evaporating the substance off the fibre may cause unwanted change for the substance, the Agilent system was used for most analyses. About 200 μL CHCl₃ was added into the solid-eliminated liquid for extracting the substance of interest. 0.2 μL of the extracted CHCl₃ phase was injected by an Agilent 7683 autosampler into an Agilent (6890N) gas chromatograph with a 5 m x 0.53 mm (Phenomenex) guard column followed by a 30 m x 0.25 mm x 0.25 μm analytical ZB5MS column. The injector temperature was from 40 °C. The column temperature was held at 30 °C for 5 minutes (in summer when the room temperature is high, 35 °C was held in the column for 6 minutes), then increased by 5 °C/min to 300 °C. The analytical software was Agilent Enhanced Chemstation G1701DA. The GC used for hydrogen detection was the Perkin Elmer Autosystem with thermal conductivity detector (TCA) and packed column HayesepA supplied by Supelco. The column was 30 feet x 0.125 inch in size. The running temperature was 30 °C. The gas sample was introduced by a syringe via a sample loop for 2 cm³ volume injection on each analysis. The analytical software was Turbochrom V4.

¹H NMR spectra were acquired on a Bruker DPX 400 NMR spectrometer running at 400 MHz. Chloroform CDCl₃ was used for extraction of substance from suspensions of solid and liquid.

6.3 Results

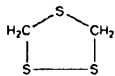
Experimental conditions and results are summarized in Tables 6.1 - 6.4. Organic sulfur compounds such as trithiane, trithiolan  and other linear polymethene sulfides were universally formed in all investigated conditions of different reaction time, temperature, presence/absence of metal sulfides, different titanium species and pH for the reactions between H₂CO and H₂S.

Table 6.1 Summary of H₂CO + H₂S batch experiments at 25 °C.

Exp. No	H ₂ CO (mmol)	H ₂ S (mmol)	pH 6 buffer (mL)	¹ H NMR	GC-MS Agilent
0203071	2.23	5	0	-S-CH ₂ -S-	trithiane and
0203072	2.23	5	0	group	trithiolan
0203073	2.23	5	10		
0203074	2.23	5	10	-	
0203075	2.23	5	10		
0203076	2.23	5	10		
0203077	2.23	5	0		
0203078	2.23	5	0		

In a simple reaction consisting of only H₂CO and H₂S at room temperature within two days, clear oil-like products formed floating at the surface and sitting at the bottom of the bulk solution (Table 6.1). GC mass spectrum data show that they were trithiane and trithiolan. ¹H NMR results also suggest the formation of -S-CH₂-S- group compounds. This is consistent with previous findings (Campaigne 1946). Since ¹H NMR results only give consistent information with those given by GC-MS, the descriptions of ¹H NMR results are minimized in Tables 6.2 - 6.4.

Table 6.2 summarizes the investigations of the system of FeS / H₂S / H₂CO in pH 6 solution. The reaction of H₂S and H₂CO, with or without the presence of FeS, varying amounts of H₂CO and temperature, for reaction time of 4 days or 19 to 52 days, with titanium ion standard solution or titanium citrate or without titanium species were investigated.

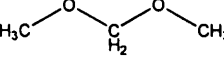
In addition to a spectrum of polymethylene sulfides, several advanced compound with C-C bond such as C₈H₁₆O and C₁₆H₂₀O were detected in exp. 0412061 and 0412064 by Agilent GC-MS. The appearance of these compounds does not seem to correlate to the presence of metal sulfide, reaction time and temperature. They were not detected by the Varian GC-MS.

Table 6.2 Experimental investigations of the FeS / H₂S / H₂CO system at pH 6.

Exp. No.	FeS (mmol)	H ₂ CO (mmol)	Ti citrate (mL)	Ti ion standard (mL)	H ₂ S (mmol)	Time (days)	T (°C)	XRPD	H ₂	GC-MS Varian	GC-MS Agilent
0412061	4.5	2.23	0	0	5	4	70	greigite	-	polymethylene sulfides	Polymethylene sulfides, several advanced compounds: C ₈ H ₁₆ O, C ₁₆ H ₂₀ O and C ₂₀ H ₂₈ O ₃ Possible: dimethoxymethane
0412063	0	2.25	0	0	5	4	70	-	no		Polysulfides, polymethylene sulfides and sulfur. Possible: dimethoxymethane
0412062	4.5	2.23	0	0	5	31	70	greigite	no		Polysulfides, polymethylene sulfides sulfur and unidentified compound. Possible: dimethoxymethane
0412064	0	2.23	0	0	5	31	70	-	no		polysulfides, polymethylene sulfides and C ₈ H ₁₆ O and

											unidentified comounds. Possible: dimethoxymethane
2112062	4.5	2.23	0	6	5	36	70	greigite	0.01%	polysulfide, polymethylene sulfides and sulfur	-
0211062	4.5	2.25	1	0	5	30	70	greigite	no	-	polymethylene sulfides, dimethoxymethane and alkenes such as C ₁₂ H ₂₄ , C ₁₈ H ₃₆
0211064	0	2.25	1	0	5	30	70	-	0.01%	-	-
2112063	4.5	0.58	1	0	5	36	70	greigite 60%; pyrite 40%	no	polysulfides and sulfur	-
0211061	4.5	2.25	1	0	5	19	70	-	-	polymethylene sulfides and some unidentified	polymethylene sulfides and alkanes such as C ₉ H ₂₀ , C ₁₉ H ₄₀ , and sulfur

									compounds		
0211063	0	2.25	1	0	5	21	70	-	0.02%	polymethylene sulfides	polymethylene sulfides, dimethoxymethane and alkenes such as C ₁₂ H ₂₄ and C ₁₈ H ₃₆
0512063	0	2.23	0	0	5	52	25	-	-	polymethylene sulfides and	polymethylene sulfides
0512061	4.5	2.23	1	0	5	44	25	mackinawite	0.02%	sulfur	polymethylene sulfides and dimethoxymethane
0512062	0	2.23	1	0	5	52	25	-	-	polymethylene sulfides	polysulfides and polymethylene sulfides

It is unlikely that the advanced C-C compounds were formed without catalyst under ambient conditions. Thus I think these compounds are likely to be from a contaminant source. The effect of FeS on the reaction of H₂CO and H₂S is not strong. The GC-MS results show that with the presence of FeS for reaction of 4 days, it shows more peaks with enhanced intensities for polymethylene sulfides and a compound could be probably assigned to dimethoxymethane,  the dimethyl acetal of H₂CO (exp. 0412061 and 0412063). However, this effect is not obvious for long time reactions for 31 days (exp. 0412062 and 0412064). In the long time reactions, S₈ was detected in two of the samples, one reacting for shorter time (4 days) without FeS, the other reacting for longer time (31 days) with FeS.

Pyrite formation is completely suppressed when the mole ratio of H₂CO:FeS was 0.5 in the reaction with H₂S at 70 °C (exp. 0412061, 0412062, 2112062 and 0211062). When the mole ratio of H₂CO:FeS was reduced to 0.25, pyrite formation was only partially suppressed and it was detected to coexist with greigite on XRPD analyses. The weight ratio estimated between pyrite and greigite by XRPD pattern is 2:3 (exp. 2112063). The enhanced temperature is necessary for the reaction since neither pyrite nor greigite was formed at room temperature (exp. 0512061) The formation of greigite as the only detected solid product in experiments 0412061-2 demonstrates that titanium citrate is not a necessity for greigite formation from the reaction of FeS, H₂S and H₂CO. The addition of titanium citrate only ensured a reducing environment and the effective total absence of molecular oxygen. The presence of titanium ion standard solution (used in ICP analysis) did not give rise to any difference in the products analysed by GC-MS (exp. 2112062).

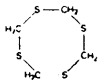
A series of alkenes (e.g. C₁₂H₂₄ and C₁₄H₂₈) were observed, together with the typical polymethylene sulfides and related compounds in experiments 0211061-3 in the presence of Ti(III) citrate in reactions between H₂CO and H₂S at 70 °C for about 20 days. The appearance of the alkenes is from a contaminant source. They showed up in another set of experiments when NiS was used instead of FeS (exp. 0205071-4, in Table 6.3), but they were not observed in a repeating set of experiments 0706071-4 in Table 6.3. The alkenes are thought to be a common contaminants brought in from the pump oil when the metal sulfide

samples were freeze dried.

The detection of hydrogen is very low and within the instrument error so is not taken into account.

Table 6.3 Experimental investigations of the FeS / NiS / trithiane system at pH 6.

Exp. No	Fe/Ni S (mmol)	Trithiane (mmol)	Temp. (°C)	Time (day)	Analyses
2404071	FeS: 4.5	0.74	70	2	¹ H NMR: -S-CH ₂ -S- group detected
2404072	-	0.74	70	2	
2404073	FeS: 4.5	0.74	25	2	
2404074	-	0.74	25	2	
2405072	FeS: 2	0.33	70	5	GC MS Agilent: polymethylene
2405073	FeS: 2	0.33	70	5	sulfide, trithiane and its fragments
0205071	NiS (pH 9): 2.71	0.33	70	4	GC MS Agilent: polymethylene
0205072	NiS (pH 7): 2.71	0.33	70	4	sulfide, polysulfides, trithiane and
0205073	NiS (pH 5): 2.71	0.33	70	4	its fragments and a series of
0205074	NiS (pH 3): 2.71	0.33	70	4	compounds such as C ₁₆ H ₃₂ , C ₁₄ H ₂₂ O and C ₁₅ H ₁₈ O ₂ .
2905071	NiS: 2.71	0.33	25	0	GC-MS Agilent: trithiane,
2905072	FeS: 2	0.33	25	0	tetrathiocane and their fragments
2905073	0	0.33	25	0	
0706071	NiS (pH3): 0.4	0	70	4	GC-MS Agilent: trithiane and its
0706072	NiS: 2.71	0.33	70	4	fragments
0706073	NiS (pH5): 2.71	0.087	70	4	
0706074	NiS: 2.71	0.33	70	4	
0706075	NiFeS: 2.71	0.33	70	4	GC-MS Agilent: trithiane,
0707076	NiFeS: 2.71	0.33	70	4	tetrathiocame and their fragments
030807	FeS: 4.5; H ₂ S: 5	2.25	70	12	XRPD: greigite and mackinawite

In Table 6.3, experiments done with trithiane instead of H₂CO (or H₂CO and H₂S) with presence of metal sulfides are summarized. The experimental conditions vary in terms of transition metal sulfides used, including FeS, NiS prepared in different pH environments, and FeNiS₂, in terms of the added amount of trithian, in terms of the reaction time and temperature in the fixed pH 6 solutions. The products in the liquid phase of the experiments using trithiane as reactant are very similar to those starting with H₂CO and H₂S as in Table 6.2. They are mainly trithiane and its fragments. Occasionally, condensation of trithiane to tetrathiocane occurs. No other  product was observed. When H₂S was added to the system of trithiane and FeS in experiment 030807, greigite was detected together with remnants of the reactant mackinawite. This result shows that trithiane functions similarly to H₂CO to catalyse the formation of greigite in the FeS and H₂S reaction.

A set of experiments were undertaken to investigate the pH effect on the reaction system of trithiane and metal sulfides at 70 °C (Table 6.4). No obvious change in the products was found at pH 7 and 9 compared with reactions at pH 6. GC-MS results show the presence of the original trithiane and its fragments. Fe/Ni sulfides remain as the original structure but in a better crystalline state as expected during the 7 days in solutions at 70 °C.

Table 6.4 Investigations of the pH effect on FeS or NiS / trithiane system.

Exp. No	Metal sulfides (mmol)	Trithiane (mmol)	pH buffer	Temp. (°C)	Time (days)	XRPD	GC-MS Agilent
2506071	FeS: 2	2	9	70	7	mackinawite	trithiane
2506072	FeS: 2	2	7	70	7	-	and its
2506073	NiS: 2	2	9	70	7	polydymite-like	fragments
2506074	NiS: 2	2	7	70	7	nanocrystalline material	

6.4 Discussion

Although the role of transition metal sulfide involved in protometabolism is widely discussed and several authors have reported its catalytic effect on carbon fixation from inorganic or simple organic substances (e.g. Cody 2004), no obvious evidence is found at low temperatures in this study. This is an interesting result since the conditions addressed in this experimentation are similar to those ambient temperatures in the modern Earth environment. Cody's (2000) experimentation, for example, was carried out at hydrothermal temperatures ($> 200\text{ }^{\circ}\text{C}$). In the light of suggestions of a warm early Earth ocean (Robert and Chaussidon 2006), it would be interesting to investigate the intervening temperature range more closely to establish if there is a zone where the temperatures of the early Earth ambient environment and relatively rapid reaction kinetics overlap.

The detection of S(0) in some systems reacting for no less than 19 days with or without presence of FeS is interesting since this suggests a redox reaction. The experimental conditions were designed to eliminate all possibility of oxidation through molecular oxygen. Thus the oxidation of sulfide to sulfur must be counterbalanced by a reduction reaction. However, this reduced product is not detected by GC-MS or ^1H NMR experiments. This appears to be a universal problem in the FeS system. Rickard and Luther (1997) proposed that H_2 was formed but could not detect stoichiometric amounts of the gas in the products. It is possible that H_2 is occluded in the solids. The possibility that the S(0) is an artefact caused through air oxidation is precluded by the careful elimination of O_2 and the sealed capsules. S(0) would initially react with H_2S to form polysulfides and ultimately pyrite. Greigite is not formed by this process (Rickard and Luther 2007).

The role of H_2CO in the formation of greigite from FeS and H_2S is becoming clear. Data in the present study show that at the mole ratio of $\text{H}_2\text{CO}:\text{FeS} = 0.25$, both pyrite and greigite are produced. If the ratio increases to 0.5, 100% greigite is formed. These figures are similar to those reported in Rickard et al. (2001). Although aldehydic carbonyl appears to catalyse greigite formation, it actually suppresses pyrite formation so that greigite is the end product

of the reaction. Aqueous FeS clusters are necessary intermediaries in pyrite formation in low temperature aqueous solutions (Rickard 1997), and Rickard et al. (2001) showed that aqueous FeS cluster formation was suppressed in the presence of aldehydic carbonyl. Cody (2000) noted that FeS-carbonyl clusters were formed in the presence of CO at elevated temperatures and it appears that the reaction at low temperatures with H₂CO also results in the formation of FeS-carbonyl clusters. These appear to be reaction inhibitors for pyrite formation.

Interestingly, trithiane is found to promote the formation of greigite (rather than pyrite) and it does not have a carbonyl group. Again the trithiane reaction appears to prevent the production of significant concentrations of simple aqueous FeS clusters necessary for pyrite formation. The result is that the reaction tends to form greigite. When H₂S is absent, the reaction does not occur. This demonstrates that H₂S is essential and is directly involved in the reaction. The extent of hydrolysis of trithiane to H₂CO is very small, because of the extra H₂S in the system which pushes the reaction (6.3) forward. The reaction is interesting since it suggests a further cause for the formation of greigite in sediments. Thio-organic compounds are common in sedimentary systems and their presence inhibits aqueous FeS cluster formation and, consequently, pyrite. The reaction may also explain why aqueous FeS clusters are not detected in some sediments: the clusters are liganded by organic moieties provided by the thio-organics. As stated in the introduction section, greigite formation is interesting due to some biochemical effect that fits into the origin-of-life hypothesis.

6.5 Conclusions

No direct evidence of the catalytic properties of iron and nickel sulfide precipitates for carbon fixation in the H₂CO and H₂S system was found in this experimentation in aqueous solutions at present-day Earth surface ambient temperatures. The appearance of a series of advanced C-C compounds is likely to be of contaminant source.

Reactions in the system of H₂CO and H₂S occasionally show the formation of S(0) which should be an oxidized product of the system and a reduced product is expected. However, the

reduced products are not detected out by the analytical means.

In addition to aldehydes, trithiane can also suppress the formation of pyrite and consequently results in greigite formation from reaction between FeS and H₂S at 70 °C. This provides a further cause for greigite formation in sedimentary systems and the reason why FeS clusters are not detected in some aqueous environment: they are complexed by thio-organics. Due to the biological potential of greigite, its formation in the presence of thio-organic compounds is interesting and provides additional information to the iron-sulfur world hypothesis for the origin of life.

Acknowledgements

I thank Joachim Rinna, Michael O'Reilly and Carsten Müller for their assistance on the TGA-MS experiments and helpful discussions, and David Knight and Damian Dunford for the help with the ¹H NMR analyses and helpful discussions.

Chapter 7

Catalytic Hydrogen Evolution in the Presence of Ni(II) and Cysteine in Sea Water

Figures

Figure 7.1 Structures of Ni-cysteine monocomplex and bicomplex.

Figure 7.2 A polarogram of the free Ni^{2+} in artificial sea water.

Figure 7.3 The near linear relationship between $[\text{Ni(II)}]$ and measured current.

Figure 7.4 A polarogram of free cysteine in artificial sea water.

Figure 7.5 The linear relationship between the added [cysteine] and remnant $[\text{Ni}^{2+}]$.

Figure 7.6 The polarogram of solution of $49.41 \mu\text{M Ni(II)}$ and $10.12 \mu\text{M}$ cysteine.

Figure 7.7 The current relationship among waves 2U and 4U, and peak 3U when cysteine is added to $50.48 [\text{Ni(II)}] \mu\text{M}$ solution.

Figure 7.8 The left shoulder of wave 2U increases with [cysteine] in Ni(II)-containing artificial sea water.

Figure 7.9 The current changes for peak 4U with increasing $[\text{Ni(II)}]$ or [cysteine].

Figure 7.10 Aging effects on the Ni-cysteine system in artificial sea water.

Figure 7.11 Proposed mechanism for catalytic hydrogen evolution in nickel-cysteine system in sea water.

Tables

Table 7.1 Lower detection limits for different voltammetric methods.

Table 7.2 Currents recorded for various species in the Ni-cysteine system at a concentration around $15 \mu\text{M}$.

Abstract

The Ni-cysteine system is studied in sea water by square wave voltammetry. It is found that nickel forms a monocomplex with cysteine when cysteine is titrated with Ni(II) solution. Evidence for the formation of multinuclear species of nickel and cysteine is also found. A catalytic hydrogen wave at -1.53 V is observed in the presence of Ni(II) and cysteine. The reaction is a modified Brdicka reaction. The reaction mechanism is proposed. The finding that nickel cysteine complex catalyses hydrogen reduction suggests that Ni-thiol substance could have played key roles in the emergence of life in the sea water environments. The appearance of the catalytic hydrogen wave could serve as a new route for electroanalytical detection of nickel and cysteine in natural water media.

7.1 Introduction

It is widely believed that the most probable circumstance for the origin of life was in the hydrosphere of the early Earth, when the oceans were dominated by sulfides (e.g. Anbar and Knoll 2002). The metal complexes with sulfides or organics, which still exist in the modern aqueous systems (Rickard et al. 1999; van den Berg 1995), facilitated the availability of metals to early organisms. The structure of iron sulfur clusters mimics the active centres of FeS proteins which occur in all living organisms (Rickard and Morse 2005). Ni and Co are considered to be the elements of the “remnant of early life” because they function in very primitive systems where the metabolism was based on CH₄ and H₂ in the period before the advent of dioxygen (Frausto da Silva and Williams 1991). The transition metal complexes, especially iron and nickel sulfides, are proposed to have played key roles in the origin of life four billion years ago in the Hadean sea (Russell and Hall 2006).

Ni is involved in an important type of hydrogenase enzyme that catalyses the interconversion of dihydrogen (Frey 2002). This is vital for anaerobic metabolism and its applications to chemical or biochemical production of hydrogen for clean fuel is obvious. In these enzymes, the nickel centre is connected to sulfur atoms and is believed to be directly involved in the hydrogen activation (Teixeira et al. 1989). Nickel possesses several structural possibilities for its complexes (Coyle and Stiefel 1988). Cysteine is an important source for sulfide in iron sulfide cluster and nitrogenase in human metabolism. Cysteine has a high capacity in its thiol group to oxidize and in the propensity of sulfur atoms to form polynuclear complexes. These

attributes explain the complexity in characterization of nickel complexes with cysteine. So far, it is generally accepted that the monocomplex has a five-membered ring with Ni binding with $-S^-$ and $-NH_2$ (Fig. 7.1a) (Srivasta et al. 1973) and the $Ni(Cys)_2$ complex is tetracoordinated in a square planar geometry where again Ni binds with $-S^-$ and $-NH_2$ (Fig. 7.1b) (Lenz and Martell, 1964). In addition, polynuclear species such as $Ni_2(Cys)_3$, $Ni_3(Cys)_4$, $Ni_4(Cys)_5$ (Perrin and Sayce 1968) and $Ni_3(Cys)_4$ and $Ni(Cys)_2$ (Kozłowski et al. 1987) have been reported spectrophotometrically or potentiometrically.

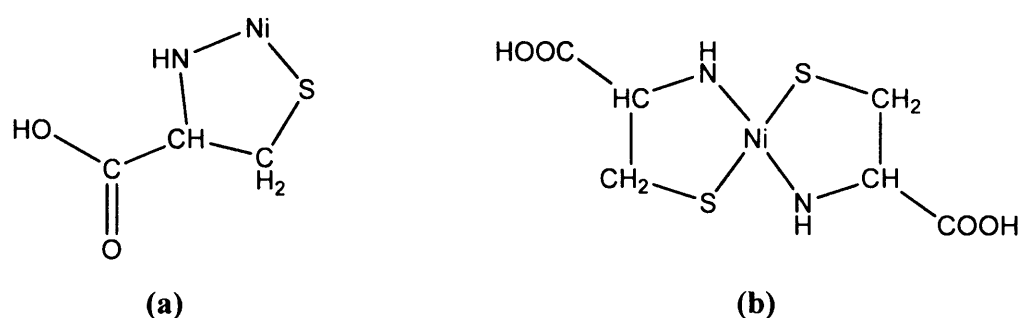


Figure 7.1 Structures of (a) Ni-cysteine monocomplex and (b) Ni-(cysteine)₂ dicomplex.

Electroanalysis is a powerful analytical tool for studying chemical reaction in a solution that involves electron transfer between the electrode and electrolyte. The potentiometric technique has been used to determine the stability constants of nickel cysteine complexes (Berthon 1995). It employs pH meters to measure hydrogen ion release while the protons dissociate from cysteine on the formation of metal complex. However, the stability constants determined in this way are not directly applicable to natural systems where the pH is buffered. Polarography, as one of the most common amperometric techniques, on the other hand, revealed the novel catalytic property of Ni complexes with thiol-containing amino acids or proteins. In a solution of nickel(II) (0.2 mM) and cysteine (0.3 mM) in acetate buffer at pH 6 under DC polarographic analysis, a catalytic hydrogen prewave (CHP) at around -1.3 V is observed before the diffusion wave of hydronium (Banica 1991). The mechanism of this reaction is proposed to be analogous to the bioproduction of hydrogen utilised by hydrogenase enzymes. At higher pH between 6 and 10, a closely related reaction is the Brdicka reaction which was observed by Brdicka in 1930s. He described the electrochemical catalytic hydrogen evolution in the thiol-containing proteins in ammonia buffered Co(III) or Ni(II) solution (Brdicka 1933).

Extensive electrochemical research on the hydrogen liberation by thiol-containing amino acids or proteins with presence of Ni or Co ions have been done by Banica and co-workers

mainly in the neutral to slightly acidic medium suited to physiological systems, or at higher pH in the $\text{NH}_4\text{Cl}/\text{NH}_3$ electrolyte solution as in the Brdicka reactions. So far, there are few reports concerning this reaction in sea water, except Lange and van den Berg (2000) who once reported catalytic hydrogen production brought about by rhodium selenide in natural water media.

Square wave voltammetry (SWV) is one of the most advanced and sensitive electroanalytical techniques. Compared with the other two pulse voltammetric techniques, “normal pulse” and “differential pulse”, square wave pulse voltammetry benefits its even higher sensitivity, thereby increased accuracy, higher scan rate and is well suited for quantitative determination of the electrode reaction (Mirceski et al. 2005). A comparison of lower electroanalytical detection limits between different voltammetric techniques is made in Table 7.1. SWV has been developed as a powerful technique for studying the cluster behaviour in solution such as stability constant determination (Luther et al. 1996). The present work reports a study of the nickel-cysteine system using the square wave voltammetry in sea water, in the context of an origin of life scenario.

Table 7.1 Lower detection limits for different voltammetric methods. (modified from Monk 2001 p.185)

<i>Voltammetric methods</i>	<i>Lower detection limit (mol/L)</i>
Normal polarography	5×10^{-3}
Cyclic voltammetry	1×10^{-5}
Sampled DC polarography	1×10^{-5}
Normal pulse polarography	$10^{-7} - 10^{-8}$
Differential pulse polarography	$10^{-8} - 5 \times 10^{-8}$
Square wave polarography	1×10^{-8}

7.2 Methods

An EG&G Princeton Applied Research Model 384B polarographic analyser and an Analytical Instrument Systems, Inc. (AIS) Model DLK-100 voltammetric analyser in conjunction with a Model 303A static dropping mercury electrode were used for the electrochemical work. Instrumental parameters for the square wave mode were based on the conditions that gave sufficient sensitivity to detect free nickel Ni (II). They were typically

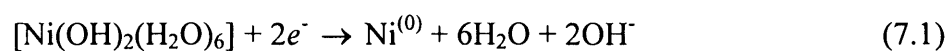
100 mV/s scan rate over the potential range -0.1 ~ -1.7 V, conditioned at -0.1 V for 2 s with equilibrium time 5 s and pulse height 50 mV. For the 384B system, artificial sea water was used as electrolyte solutions. It was made up from 0.55 M NaCl and 0.004 M NaHCO₃. For the DLK 100 system, natural sea water was used. The pH for both artificial sea water and natural sea water is 8.10. The end pH after titrations of nickel and cysteine in artificial sea water was within the range between 8.1 and 8.7.

Analytical grade NiSO₄·7H₂O, (NH₄)₂Fe(SO₄)·H₂O and Na₂S·9H₂O and L-cysteine (array > 99%) were used to make up starting solutions in deionised 18.2 MΩ cm (DW, MilliQ) (or distilled) water, which was deoxygenated by bubbling with oxygen-free N₂ or Ar for at least 45 minutes before making up the solutions. 10 mL distilled water was introduced in a cell and deoxygenated by bubbling with oxygen-free nitrogen for at least 10 minutes. Preliminary runs were made to confirm no oxygen detectable in the solution. A N₂-filled MBraun Labmaster 130 anoxic chamber maintained at O₂ < 2 ppm level was used for testing the stability of the Ni-cysteine complex.

7.3 Results

7.3.1 Basic electrochemical behavior of Ni²⁺ and cysteine

The free Ni²⁺ ion in aqueous solution occurs as the hexaqua Ni(II) species, Ni(H₂O)₆²⁺ which I refer to as Ni²⁺. The electrochemical characteristics of Ni²⁺ in artificial sea water were investigated with the 384B system by increasing the concentration of nickel [Ni(II)], in the cell solution. The result shows a single peak at c. -1.07 V which is the free hydrated Ni²⁺ oxidation peak (Fig. 7.2). The Ni(II) reaction at the Hg electrode follows:



In inorganic seawater, Ni(II) occurs dominantly as the free ion Ni²⁺ (Bruland and Lohan 2004). A near linear relation between the added [Ni(II)] and current collected at the electrode is established, as plotted in Fig. 7.3. It suggests that the current noted closely represents the [Ni(II)] in the cell solution in the range between 14.99 to 205.89 μM. Since [Ni(II)] closely approximates [Ni²⁺] in seawater solutions at constant ionic strength, Fig 7.3 shows that Ni(II) concentrations in the experimental solution can be measured by the peak current for the Ni²⁺ wave.

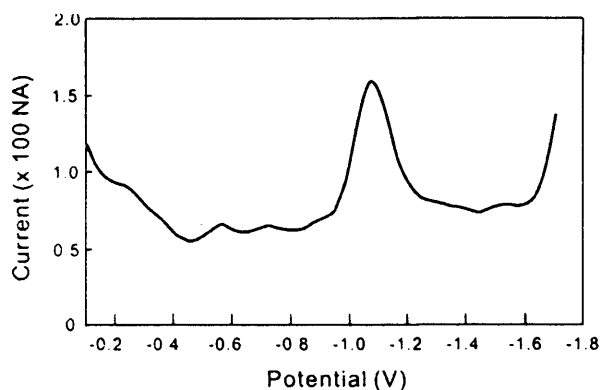


Figure 7.2 A polarogram of the free Ni^{2+} peak at c. -1.07 V in $49.04 \mu\text{M}$ nickel sulfate in artificial sea water.

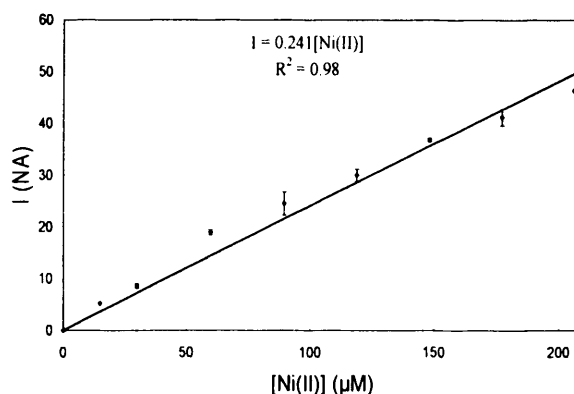


Figure 7.3 The near linear relationship between $[\text{Ni(II)}]$ and measured current.

Free cysteine was examined in a similar way in the artificial sea water. At pH 8 - 9, the protons of the carboxyl and amino groups of cysteine do not dissociate (Raspor 2001). A single free cysteine peak is observed at c. -0.5 V (Fig. 7.4). No other wave is observed in the scan range between -0.1 V and -1.7 V. A linear relation between the cysteine concentration, $[\text{cysteine}]$, and the current is also established. The cysteine reaction at the Hg electrode is the sulfur oxidation reaction



where $\text{R} = \text{HCOOCH}(\text{NH}_2)\text{CH}_2$. R-SH represents a cysteine molecule.

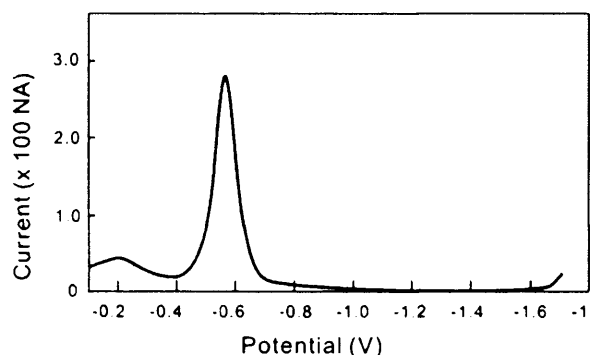


Figure 7.4 A polarogram of free cysteine peak at c. -0.5 V in $24.97 \mu\text{M}$ cysteine in artificial sea water.

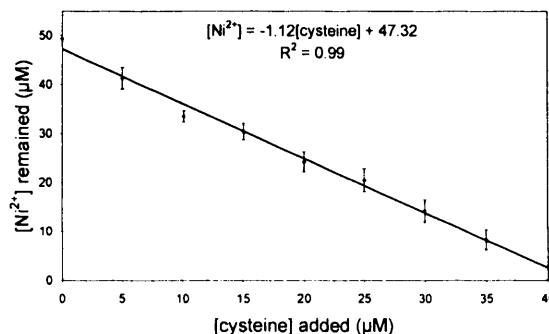
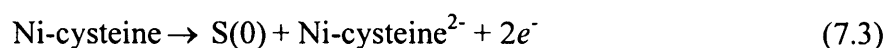


Figure 7.5 The linear relationship between the added $[\text{cysteine}]$ and remnant $[\text{Ni}^{2+}]$. Free Ni^{2+} current is monitored when cysteine is added to $50.48 \mu\text{M}$ Ni(II) in artificial sea water. It shows the formation of nickel monocomplex with cysteine.

Fig. 7.5 shows the decrease of $[\text{Ni}^{2+}]$ calculated from the recorded currents while cysteine ($5.02 - 39.92 \mu\text{M}$) was added to $49.41 \mu\text{M}$ Ni(II) in artificial sea water. The linear decrease of $[\text{Ni}^{2+}]$ with an approximate -1 slope indicates that a Ni-cysteine complex at 1:1 ratio was mainly formed during the course of titration.

7.3.2 Characteristic SWV patterns of Ni(II)-cysteine in sea water

Fig. 7.6 is a typical polarogram during the above titration when both cysteine and Ni(II) were present in the cell solution. Peak 1U at around -0.3 V represents the sulfur oxidation in complexed cysteine with nickel. The reaction occurs as:



As can be seen in Fig. 7.6, the oxidation peak of complexed cysteine is distorted and positively shifted relatively to the free cysteine peak with absence of Ni(II). This distorted oxidation peak appears in the solution when $[\text{Ni(II)}] \neq [\text{cysteine}]$. A similar distorted peak was reported by Banica (1994) in the solution of Ni(II) and cysteine in acetate buffer at pH 6. The distorted peak shape indicates the formation of multinuclear complexes such as $\text{Ni}_{(m)}\text{Cysteine}_{(n)}$ (m and n are integers). The formation of the multinuclear species prevents the use of the DeFord and Hume method for stability constant determination (Luther et al. 1996) of the formed Ni-cysteine complex in this system. When $[\text{Ni(II)}] = [\text{cysteine}]$, the peak shape tends to be symmetric, indicating the 1:1 nickel complex with cysteine was formed. Peak 3U is the uncomplexed Ni^{2+} reduction peak at -1.07 V occurring as reaction (7.1).

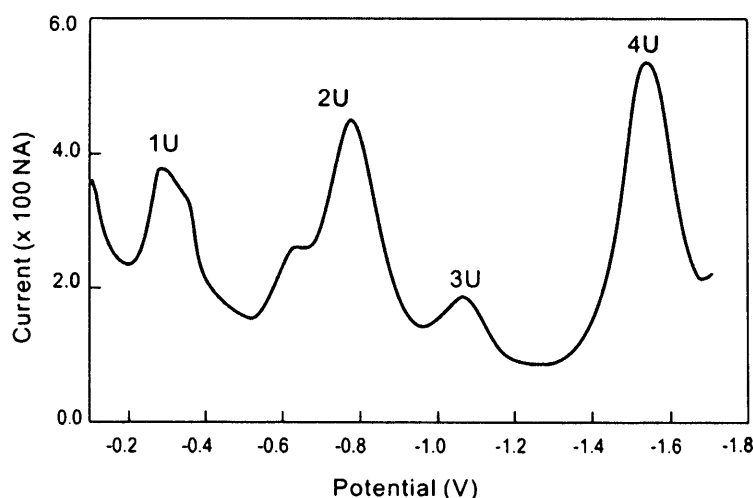


Figure 7.6 The polarogram of solution of $49.41 \mu\text{M}$ Ni(II) and $10.12 \mu\text{M}$ cysteine. 1U represents the oxidation peak for complexed cysteine; 2U, the catalytic nickel reduction prewave; 3U, the reduction peak of the hydrated uncomplexed Ni^{2+} ion; and 4U, the catalytic hydrogen wave.

A stable wave at -1.53 V (4U) and a double wave located between -0.6 V and -0.8 V (2U) were observed in Fig. 7.6. By analogy with the earlier polarographic findings (Banica and Calusaru 1983; Brdicka et al. 1965; Raspor 2001), 4U is ascribed to the catalytic hydrogen wave where hydrogen gas is liberated catalysed by Ni-cysteine complex; and 2U is ascribed to the catalytic nickel wave where complexed nickel is catalytically reduced at a potential positive to 3U. Evidence supporting this assertion is presented in the next section.

Titration between Ni(II) and cysteine from the opposite direction was carried out by adding nickel sulfate solution into cysteine solution. All the peaks appearing in Fig. 7.6 are observed in both directions of titrations. Similar results were also obtained in the DLK 100 system with natural sea water as electrolyte, although the peak positions were slightly shifted.

7.3.3 Characteristics of the catalytic nickel and hydrogen waves

Waves 2U and 4U only appear when both cysteine and nickel are present in the solution (Figs. 7.2, 7.4 and 7.6). Fig. 7.7 shows the change of currents of 2U, 3U and 4U on addition of cysteine to Ni(II) solution. The 2U current was measured as the sum of its two subwaves. It can be seen that the current values of 2U and 4U are much greater than that of 3U. The very high ratio of intensities of 2U and 4U to the diffusion nickel ion current (3U) is a

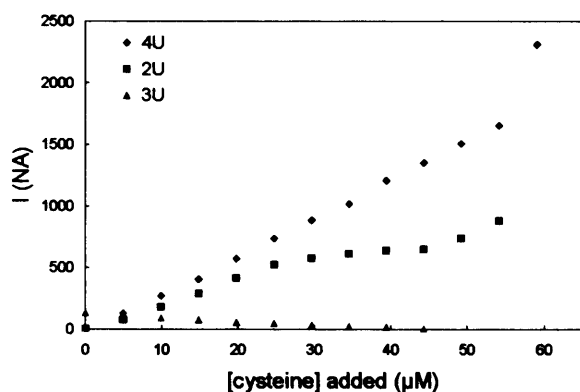


Figure 7.7 The current relationship among waves 2U and 4U, and peak 3U when cysteine is added to 50.48 $[\text{Ni(II)}]$ μM solution. 4U increases almost linearly when $[\text{cysteine}] = 4.96$ to 54.06 μM . 2U increases too but shows a step when $[\text{cysteine}] > 29.63$ μM .

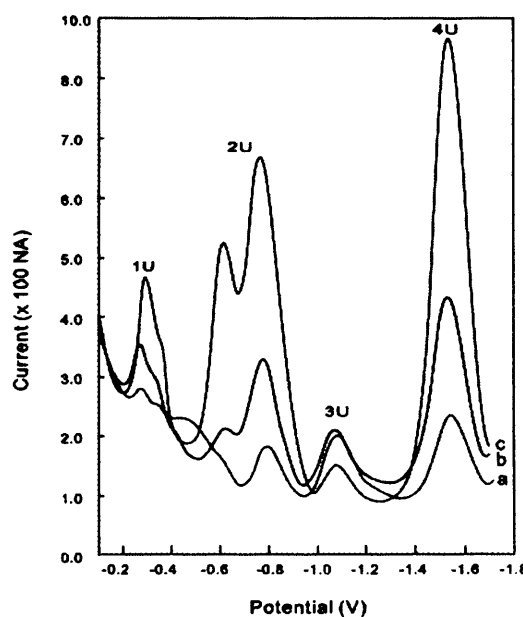


Figure 7.8 The left shoulder of wave 2U increases with $[\text{cysteine}]$ in Ni(II)-containing artificial sea water. $[\text{Ni(II)}]$: 50.48 μM , $[\text{cysteine}]$: (a) 4.96 , (b) 9.92 , (c) 24.72 μM .

decisive character of the catalytic waves (Banica and Ion 2000). On addition of cysteine, 3U dropped steadily while 2U almost grew linearly and 4U grew unevenly with a step between [cysteine] = 29.63 and 44.32 μM . The uneven increase of 2U is probably due to the measurement error when the left shoulder of 2U grew faster than its right side and this interfered with the intensity measurement (Fig. 7.8). The phenomenon of uneven growth of one side of 2U is consistent with the observance of Calusaru and Voicu (1973) who reported the catalytic hydrogen production by seleno-cystine with nickel. During the titration process, the free Ni^{2+} ion is consumed by the complexation with the added cysteine and the as-formed Ni-cysteine complex promoted the hydrogen gas production (4U) and the catalytic Ni(II) reduction (2U). The cyclic voltammetry experiment confirmed that 4U is irreversible, which agrees with the nature of hydrogen evolution.

Fig. 7.9 shows the current changes of wave 4U with increasing [Ni(II)] in constant [cysteine] solution and with increasing [cysteine] in constant [Ni(II)] solution. It can be seen that the wave intensity grew linearly with increasing [cysteine] between 5 to 49 μM in the solution containing 25.36 μM Ni(II). The linear increase of catalytic hydrogen current with the thiol concentration is a typical Brdicka reaction phenomenon when the Brdicka current is below 20% of its saturation value (Mader et al. 1982). On the other hand, when nickel ion was added to cysteine solution, the peak height levelled off after Ni(II) reached 10 μM in the solution containing 24.90 μM cysteine. This can be explained by that, nickel is the catalyst, and the reaction needs 10 μM to get it going. After that, the catalytic nickel is regenerated. Cysteine is the H provider.

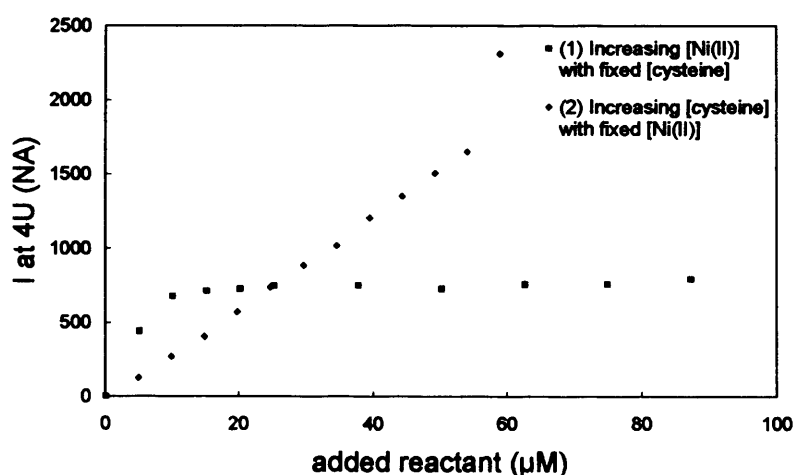


Figure 7.9 The current changes for peak 4U with increasing [Ni(II)] or [cysteine]. (1) was recorded by adding Ni(II) to 24.90 μM cysteine artificial sea water. (2) was recorded by adding cysteine to 25.36 μM [Ni(II)] artificial sea water. The current increases almost linearly with increasing [cysteine] but it remains unaffected with varying [Ni(II)].

Compared with Fig. 7.4, it is found that the shapes of 2U and 4U waves in Fig. 7.6 are less sharp as the free cysteine diffusion peak. This indicates the different nature of waves 2U and 4U from the free cysteine peak. The currents recorded for the free and complexed species in the Ni-cysteine system at concentration of about 15 μM in artificial sea water are compared in Table 7.2. It confirms that 2U and 4U are much stronger than the diffusion Ni^{2+} peak. In addition, at same concentration of added cysteine, 4U has similar currents with free cysteine peak. The difference between 4U and free cysteine peak in potential and the peak shape indicates that the two features are of different nature, but the two separate electrode reactions may have same number of electrons transferred per mole of cysteine present in the cell solution. According to formula (7.2), there are two electrons transferred for each free cysteine molecule reacting at the electrode. For the catalytic hydrogen production at -1.5 V in the presence of nickel, there are perhaps also two electrons transferred but from the electrode to cysteine that liberate the hydrogen ions from cysteine to dihydrogen.

Table 7.2 Currents recorded for various species in the Ni-cysteine system at a concentration around 15 μM .

<i>Species (conc. in μM)</i>	<i>Current (NA)</i>
[Ni (II)] = 14.99	$I_{\text{Ni}} = 5$
[cysteine] = 15.08	$I_{\text{cysteine}} = 407$
[cysteine] = 14.86 [Ni(II)] = 50.48	4U = 403 2U = 290
[cysteine] = 24.97 [Ni(II)] = 15.17	4U = 714 2U = 530

Peaks 2U and 4U appear simultaneously and instantly on the first addition of cysteine to Ni(II) solutions when [cysteine] = 1/5 [Ni(II)] = 1.91 μM and on the first addition of Ni(II) to cysteine solution when [Ni(II)] = 1/5 [cysteine] = 0.97 μM . Their occurrence on the low and non-stoichiometric ratio of concentrations of the two species present in the cell solution supports that the process is catalytic. The simultaneity is considered as a characteristic feature of the catalytic hydrogen production and it indicates that the two reactions at the electrode are correlated (Banica and Calusaru 1983). Following the idea developed above that nickel catalyses the liberation of hydrogen ion from cysteine, the 2U wave is reasonably ascribed to the catalytic nickel wave.

Changing the scan rate results in changes in the currents of waves 2U and 4U. When the scan rate increased from 100 mV/s to 200 mV/s, the currents of 2U and 4U were nearly doubled.

This disagrees with Ion et al. (1998)'s observation in their system of nickel complex with 6-mercaptopurine-9-D-ribose that the catalytic nickel reduction peak was independent of the scan rate while the free hydrated Ni^{2+} reduction was proportional to scan rate.

7.3.4 Occurrence of the catalytic waves

Fig. 7.10 shows the comparison of polarograms of fresh Ni-cysteine complex solution (a) and the one having been kept in a Teflon-capped cell in a N_2 -filled anoxic chamber for three days (b). The two electrochemical patterns show similar main features with all the four main peaks remained. The currents of the two waves 2U and 4U of the 3 days solution decreased 23% and 53% respectively compared with those of the fresh complex solution. The oxidation peak for complexed cysteine (1U) displays a better symmetric shape with slightly increased intensity after three days. No obvious change is observed for 3U, the free Ni^{2+} peak. This may indicate the loss of cysteine in the three days placement, as resulted in the reduction of the two catalytic waves. In the same time, the multinuclear species of nickel cysteine complex(es) underwent a transformation to the more stable nickel monocomplex.

Titration of Ni(II) and glycine were conducted in both directions in the natural sea water with the DLK 100 system. No catalytic prewaves were observed. Glycine is structurally similar to cysteine, but does not have a thiol group. This confirms the results of previous studies that the thiol group is essential for the catalytic liberation of hydrogen gas (e.g. Banica and Ion 2000).

Titration between Fe(II) and cysteine were conducted in both directions in filtered sea water and artificial sea water. No catalytic prewaves were observed either. This is consistent with the previous literature that only Co and Ni were found to have such a catalytic effect for hydrogen evolution.

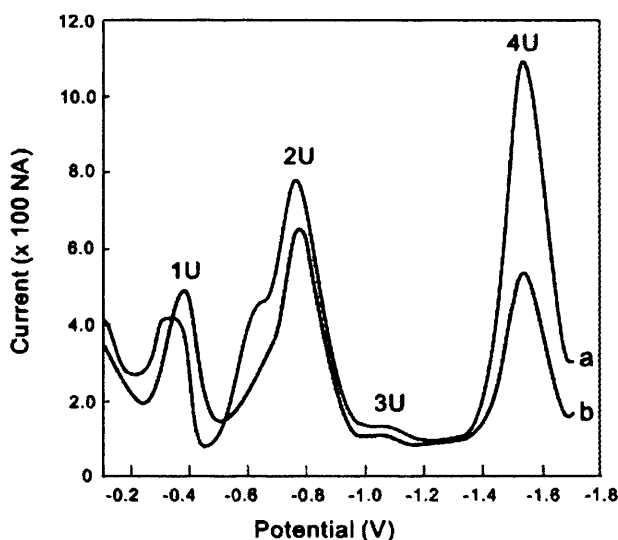
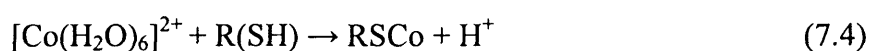


Figure 7.10 Aging effects on the Ni-cysteine system in artificial sea water. (a) Polarogram of fresh Ni-cysteine solution. (b) Polarogram of Ni-cysteine solution having been kept in the N_2 -filled anoxic chamber for 3 days.

7.4 Discussion

Catalytic dihydrogen production has been reported in three electrochemical systems: (1) the *presodium wave*, catalysed by cysteine-related proteins (Tomschik et al. 2000) or cysteine derivative compounds (Voicu and Calusaru 1973) without presence of metal; (2) The *Brdicka wave*, catalysed by cysteine-related proteins or its derivatives with presence of Co or Ni in ammonia buffer solutions in slightly alkaline conditions. Co appears to be more effective over Ni in the *Brdicka reaction* (Brdicka 1933; Brdicka et al. 1965); and (3) the *catalytic hydrogen prewave (CHP)*, catalysed again by cysteine-related proteins and its derivatives or even sulfide (Banica et al. 1997) in the presence of Ni (Banica 1991; Banica and Calusaru 1983; Banica et al. 1994) or Co in acetate or acetate phosphate buffer at strictly restrained pH around 6 and 7.

In my experiments, the necessity for the presence of both nickel and cysteine is obvious so it is not the case of *presodium wave* in (1). Banica (2000) differentiated between the Brdicka wave and the CHP by the different dihydrogen liberation potentials and the wave shapes. Two mechanisms are formulated for the above two reactions. The *Brdicka wave* is proposed to be produced by the reprotonation of deprotonated $R(S^-)$ (where $R(S^-)$ represents a deprotonated thiol-containing protein or amino acid) through the ammonia electrolyte from $NH_4^+ \rightarrow NH_3$. The catalytic dihydrogen is evolved via the reaction between protonated $R(SH)$ and $Co(II)$ following



then proton is reduced to molecular hydrogen at the catalytic potential (Raspor 2001). This hypothesis is supported by the fact that enhanced dihydrogen wave is obtained in high concentration of ammonia solutions. The mechanism for CHP proposed in Banica (1991) is relied on the $Ni(I)/Ni(0)$ state changes. The reaction is initiated by the electrochemical reduction of $Ni(II)$ -cysteine complex to $Ni(0)$ -cysteine where $Ni(0)$ acts as a strong Lewis base and is subsequently attached to H^+ from the proton donors in the solution. On further reduction at the electrode, the proton attached to $Ni(0)$ -cysteine complex is reduced to H^- and then reacts with another H^+ from the proton donors in the solution to form a molecular H_2 . This mechanism seems to be supported by the fact that the reaction is not observed in alkaline solutions but only in slightly acid solutions where sufficient proton donors are available.

The above two mechanisms for the *Brdicka reaction* and the *CHP reaction* are not relevant to the hydrogen evolution in the present study because neither ammonia species nor the slightly acid pH is present in the sea water system. The linear relation between the cysteine concentration and the current of the hydrogen wave, and the comparable currents between free cysteine peak and the catalytic hydrogen wave at same concentration of cysteine imply that cysteine is the proton provider at the electrode. The number of electrons transferred for catalytic hydrogen production per cysteine molecule is two, the same as the free cysteine oxidation reaction at the electrode. Thus I propose the mechanism of catalytic hydrogen reaction in the present study as follows: The complexed Ni(II)-RS is reduced to Ni(0)-RS at c. -0.7 V (2U). The zero valence nickel in the cysteine complex is a strong base and cause the hydrolysis of the amino- and thiol- groups in cysteine that connect to Ni(0). Thus one electron from the zero valence nickel moves to the protonated amino-group and another electron from nickel moves to the protonated thiol-group. At -1.53 V, two protons are liberated from the nickel cysteine complex to form a molecular H₂ and Ni(II)-RS is regenerated. The mechanism is depicted in Fig. 7.11.

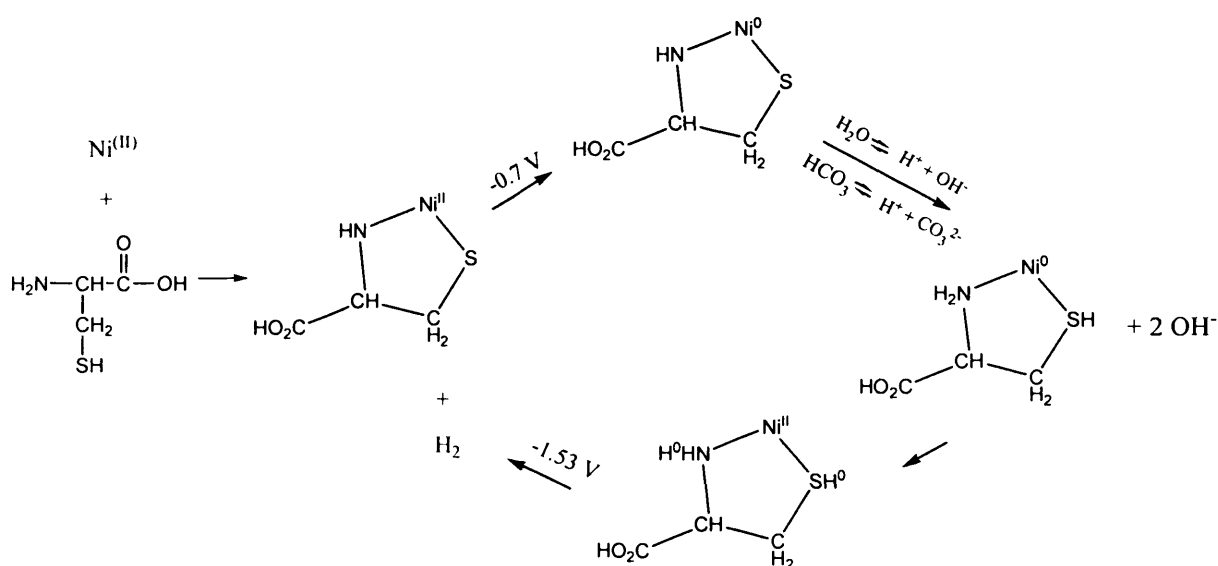


Figure 7.11 Proposed mechanism for catalytic hydrogen evolution in nickel-cysteine system in sea water. The complexed Ni(II)-RS is reduced to Ni(0)-RS at c. -0.7 V. The zero valence nickel is a strong base and causes the hydrolysis of the amino- and thiol-groups in cysteine that connect to Ni(0). Thus one electron from Ni(0) moves to the protonated amino-group and another electron from Ni(0) moves to the protonated thiol-group. At -1.53 V, two protons are liberated from the nickel cysteine complex to form a molecular H₂ and Ni(II)-RS is regenerated.

In this reaction, cysteine is the direct proton provider for molecular hydrogen production but the ionized hydrogen from bicarbonate ion or water is the ultimate hydrogen source. This is supported by the experiment done in NaCl solution at the same concentration but without adding bicarbonate. The catalytic hydrogen and nickel waves still appeared but in a much smaller scale. This indicates that the presence of bicarbonate facilitates the hydrolysis of Ni(0)-cysteine complex. This agrees with previous observations that the buffer composites influence the production of catalytic hydrogen (Mader et al. 1982). The different types of buffer used in the electrochemical experiments of catalytic hydrogen evolution may also explain the CHP observations described in much of Banica and his coworker's work (1991; 1994) that the catalytic hydrogen production is strictly restrained by a narrow range of pH.

The structural analogy between the abiotic nickel-cysteine complex and the Ni-centred enzyme with a cysteinyle residue as ligand in some hydrogenases is briefly discussed in Banica (Banica 1991). The present study shows that the catalytic function of Ni-thiol group not only happens in the physiological environments but also in the natural sea water system. At a potential near -0.6 V (Eh) at pH 8, water breaks down to molecular H₂ in an equilibrium system at 1 atm. However, there is a kinetic problem in this reaction. The water breakdown requires a considerable overpotential. The present study shows that Ni-cysteine complex is one of a series of catalysts that lower the overpotential of the reaction. The amount of hydrogen production decreases logarithmically as the potential increases. At high pressures, for example, in deep sea environments, the potential needed is more negative than that at 1 atm in this study. However, from a geochemical or biogeochemical point of view, the amount of hydrogen is still significant in the environments at equilibrium.

In this work, Ni(II) ion was detected at a concentration as low as 0.97 μM and cysteine was detected at a concentration of 1.91 μM with the characteristic appearance of the catalytic hydrogen and nickel waves. The lower detection limit for the two species by this technique should be lower than those two values by adding more of the other part of the reaction. This is particularly reasonable for Ni(II) detection with the fact that the height of 4U increases with [cysteine]. The finding in this work provides a route for detection of trace Ni(II) and cysteine-related compounds in natural water system via the electrochemical technique.

7.5 Conclusions

Catalytic hydrogen evolution in the presence of Ni(II) and cysteine happens not only in the physiological system but also in natural sea water. The thiol component is essential for this reaction to occur and Ni(II) cannot be replaced by Fe(II). The finding supports the critical role of nickel and thiol group that may have played in the process of emergence of life in sea water.

The reaction of hydrogen evolution in this study is a modified Brdicka reaction. It cannot be satisfactorily explained by the previously proposed mechanisms for Brdicka reaction or the CHP reaction because of the absence of ammonia species and the inconsistent pH range. The reaction mechanism in this study is proposed.

The main complex product during the titration between Ni(II) and cysteine in sea water is Ni mononuclear complex with cysteine. However, evidence is found for the formation of multinuclear nickel cysteine complexes.

The phenomenon of the catalytic hydrogen wave in the sea water solution of nickel and cysteine provides a new route for electroanalytical detection of Ni(II) and cysteine related compounds in this system.

Acknowledgements

I thank George Luther and Katherine Mullaugh for teaching me to do the voltammetric experiments at the University of Delaware, USA.

Chapter 8

Discussion and Conclusions

Tables

Table 8.1 The oxides, sulfides and hydroxide of Fe, Ni and Co.

Table 8.2 A summary of hydrothermal prebiotic syntheses in the presence of transition metal compounds.

8.1 Characterization of nanoparticulate NiS

8.1.1 Composition

Chapter 3 reports the chemical analysis of the nanoparticulate NiS precipitated at pH 9. It is found that the atomic ratio between Ni and S is close to 1. Ni might be in slight excess of about 7 at% to S atoms. The valence is balanced by the hydroxyl group due to the alkaline precipitation environment.

The material is hydrated. Water accounts for about 22 wt% of the material. The formulation of this material is consequently proposed as $\text{NiS}\cdot x\text{H}_2\text{O}$ where x approximates to 1.5. The hydrated nanoparticulate NiS is consistent with the classical core-mantle model in which a well-structured core closely approximating bulk phase structure and composition is surrounded by a hydrated mantle, which is limited in long-range structural ordering and whose composition is less well constrained.

The average NiS nanoparticle precipitated at pH 9 in aqueous solutions at low temperatures is about 4 nm in diameter and contains a 1 nm crystalline NiS (millerite) core surrounded by a highly defective and water-containing mantle phase. There are about 24 ± 3 H_2O molecules per nm^3 in the mantle layer of the nanoparticles. The water content is about 6 times as much as the surface water contained in ZnS nanoparticles described in Zhang et al. (2003). The water in NiS nanoparticles in this study is not surface water but they are incorporated in the mantle phase which is about 1.5 nm thickness, twice of that of the nanoparticulate ZnS in Zhang et al. (2003). The difference in water contents between the ZnS and NiS nanoparticles may be attributed to the different means of water addition to the two metal sulfides. In Zhang et al. (2003), anhydrous nanoparticulate ZnS was first precipitated in an organic solvent and water was added subsequently. The hydrated NiS nanoparticles in this study were prepared directly via aqueous precipitation where water strongly interacted with Ni and S ions in solution when they were initially bonded, thus resulting in a more severe effect on the structure.

Over time, the particles grow and the core becomes the dominant phase. The particle composition is thus expected to approach that of the bulk phase with time. The consequence of this process is that the nanoparticle composition will ultimately change with time. However, no significant change in water content was observed in NiS precipitated at pH 9

when the sample is stored in an N₂ filled anoxic chamber under standard conditions within 60 days. The loss of water on heating is demonstrated to be not kinetically controlled. The water content remains almost constant at 200 °C over 2 hours. This indicates that the metastable configuration of the material is quite robust and the water is bound in mantle structure and not adsorbed on the surface. In contrast, NiS precipitated at more acid pH values changed to the more stable structures, Ni₃S₄ (polydymite) and Ni₃S₂ (heazlewoodite) at rates dependent on the pH of the precipitation solution.

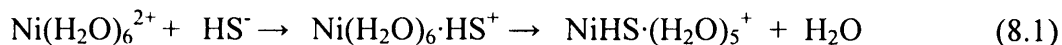
The incorporation of the hydroxyl group is the result of the competing reactions of formation of NiS and Ni(OH)₂ during the precipitation process. However, Ni(OH)₂ does not crystallize a discrete phase since it does not appear on XRPD results as Braggian peaks. The hydroxyl group is supposed to be only positioned in the mantle and thus the millerite-like NiS core is not affected and observed in XRPD, PDF, HRTEM and SAED data. Preliminary XPS and Infra-Red (IR) experiments suggested the existence of hydroxyl group. However, more XPS, IR or Raman spectroscopic experiments are required to verify the existence of H₂O.

8.1.2 Structure

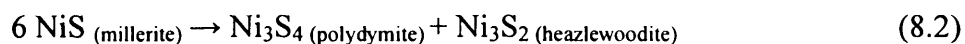
Chapter 4 and Chapter 5 report the structural characterization of the nanoparticulate NiS precipitates. Results from XRPD, PDF, HRTEM and SAED analyses indicate that the initial structure of the precipitate is millerite-like. The structural coherence estimated from the fall-off of amplitude of the PDF features and from Scherrer's formula according to the simulated XRPD patterns is about 1 nm for samples precipitated in neutral to alkaline conditions. This is the size of the crystalline NiS (millerite) core in the nanoparticles. Beyond the core range, the structure is highly defective and is affected by the water bonding, which contributes to the broadness in the XRPD, PDF and SAED patterns.

The process of nanoparticle growth is complicated by the tendency for the particle to change toward lower energy configurations, which means that particle development may be accompanied by phase changes as the least stable initial phase transforms to successively more stable configurations. In the NiS system in water at low temperatures, the first formed phase has a millerite-like structure at all pH ≤ 9. The precipitation of FeS under these conditions was shown to follow Eigen–Wilkins kinetics (Rickard 1995) where the rate is dependent on the rate of water exchange and approximately independent of the nature of the metal ion. This means that NiS precipitation follows a similar reaction process and the first formed phase is predicted to be a Ni monosulfide. The water content of the NiS precipitate is

consistent with the reaction mechanism, where the rate determining step is the replacement of water in the inner sphere complex of the hexaqua-Ni⁺² ion by sulfide. For example, the reaction with nucleophilic HS⁻ is



In the NiS system, the first-formed phase has a millerite-like structure and undergoes a series of transformations to more stable configurations. The results of this experimental program show that the nanoparticulate NiS transforms to a more crystalline Ni₃S₄ (polydymite) phase under standard conditions. This transformation occurs more readily in samples formed in acid solutions. It is accompanied by the Ni₃S₂ (heazlewoodite) formation:



The transformation is a solid state reaction. Heazlewoodite is an interesting material. Its non-classical stoichiometry has been explained in classical terms as a nickel sulfide phase with chains of Ni(0) atoms permeating the structure (Gibbs et al. 2005). In this system it appears that heazlewoodite is a by-product of the formation of polydymite, since the polydymite forms well-ordered and relatively large crystals during the transformation process. The heazlewoodite, by contrast, does not appear to display long coherence lengths in the product mixtures. Interestingly, the net Ni:S ratio of the mixed product remains close to 1:1.

The process occurs in solution at acid pH values where the solubility of NiS, and thus the rate of crystal growth, is optimized. However, it appears also to occur in dry conditions at low temperatures probably facilitated by the water in the nanoparticle NiS mantles. This would suggest that the mantle water contains hydrogen ions at concentrations which reflect the bulk pH of the precipitating medium. This in turn is a consequence of the rapid precipitation of the first-formed NiS phase. The transformation in the NiS system may be facilitated by the hydrogen bonding and polar water species, which are absent in the Fe counterpart (Rickard et al. 2006). The mantle water was demonstrated to strongly interact with Zn and S atoms in nanoparticulate ZnS (Zhang et al. 2003). The hydroxyl group, which is incorporated in samples formed in alkaline conditions, may not enhance rate of the transformation since it will not increase the solubility. This effect is demonstrated by the maintenance of very small nanoparticulate NiS in the pH 9 precipitates with a millerite

structure for the period of this experimentation (about 1 year) under standard conditions in the N₂-filled anoxic chamber.

The NiS → Ni₃S₄ transformation is apparently analogous to the FeS (mackinawite) → Fe₃S₄ (greigite) transformation in the FeS system. Transformation from mackinawite to greigite occurs under electron beam bombardment (Horiuchi 1971) or by heating (Lennie et al. 1995). The conversion is found to be facilitated by a structural congruence between mackinawite and greigite. The reduction product of the transformation in the FeS system is unknown (Rickard and Luther 2007) but it has been widely reported that the Fe:S ratio after the transformation is 1:1, which is similar to the NiS experience. The finding of the Ni₃S₂ formation accompanying with the NiS → Ni₃S₄ transformation in the NiS system suggests there might be a hitherto undetected Fe-rich sulfide phase formed as the reduction product accompanying the FeS → Fe₃S₄ transformation.

8.1.3 Structural comparison of sulfides of Fe, Co and Ni

Iron, cobalt and nickel are closely related transition metals. Their oxide, sulfide and hydroxide compounds share several common structures including the monosulfide in NiAs-type structure, monoxide in cubic structure, bisulfide in cubic structure, thiospinel and pentlandite structures, and hydroxide in hexagonal structure. Table 8.1 summarizes the structures of compounds of the three transition metals. Rosenqvist (1954) investigated the sulfides of the three elements thermochemically and showed that for NiAs-type monosulfides of the three metals, the entropies decrease in the sequence FeS through CoS to NiS while the heat of formation of the three phases from metal and hydrogen sulfide is similar. Besides the possibility that FeS have a higher vibrational frequency of the atoms, he suggested that the reason of higher entropy for NiAs-type FeS is because this phase possesses more disorder caused by lattice vacancies. In contrast, the entropies of the metal disulfides of the three metals increase from FeS through CoS to NiS with decreasing heat of formation in this sequence. This was explained by decreasing binding forces and increasing intrinsic disorder in the sequence.

Table 8. 1 The oxides, sulfides and hydroxide of Fe, Ni and Co.

Structure	Fe	Co	Ni
hexagonal R3m	-	-	NiS (millerite)
hexagonal P63/mmc	Fe _{1-x} S (pyrrhotite)	CoS (jaipurite)	NiAs-type NiS
tetragonal P4/nmm	FeS (mackinawite)	-	-
cubic Fm-3m	FeO (wuestite)	CoO	NiO (bunsenite)
cubic Fd3m	Fe ₃ S ₄ (greigite)	Co ₃ S ₄ (linnaeite)	Ni ₃ S ₄ (Polydymite)
Cubic Fd3-mz	Fe ₃ O ₄ (magnetite)	Co ₃ O ₄	-
hexagonal R3-CH	Fe ₂ O ₃ (hematite)	-	-
cubic Pa3	FeS ₂ (pyrite)	CoS ₂ (galtierite)	NiS ₂ (vaesite)
tetragonal C222	-	-	Ni ₉ S ₈ (godlevskite)
cubic Fm-3m	(Fe ₉ Ni)S ₈ (pentlandite)	Co ₉ S ₈ (cobaltpentlandite)	(Fe ₉ Ni)S ₈ (pentlandite)
hexagonal R32	-	-	Ni ₃ S ₂ (heazlewoodite)
P(-3)M1	Fe(OH) ₂	Ni(OH) ₂ (theophrastite)	Co(OH) ₂

However, the factors influencing the stability of phases in lower temperatures involving water species are not well understood. The nature of the first formed CoS phase remains unknown and is an obvious target for further experimentation. In the FeS and NiS system the first-formed phase is the least stable and it is expected that a similar product will be found in the CoS system, for the kinetic reasons described above. The first precipitated NiS and FeS phases from aqueous solutions at low temperatures are structurally and compositionally very different. Fresh FeS precipitate develops a tetragonal mackinawite structure and is anhydrous (Rickard and Luther 2007). The first NiS precipitate develops hexagonal millerite core but includes a hydrated mantle. There is no obvious reason for the difference in structure of the first-formed precipitate in the aqueous FeS and NiS systems. Although the electronic configurations are similar, the $3d^4$ Fe(II) configuration is geometrically sufficiently divergent from the $3d^6$ Ni(II) to result in different coordination geometries with sulfide. Luther and Rickard (2005) showed that, in the FeS, ZnS and CuS systems the structure of the first formed phase was similar to the solution moiety, in particular the form of the aqueous metal sulfide clusters which immediately precedes precipitation. The form – or existence – of similar aqueous NiS (and CoS) clusters has not been determined as yet, but it might hold the key to explaining the structural divergencies between the first-formed phases in these closely related systems.

8.2 Formaldehyde world

8.2.1 H_2CO carbon fixation reaction

Although formaldehyde (H_2CO) is a simple compound that is of great potential as a building block for the prebiotic synthesis of the living-essential compounds, no evidence was found for the formation of C-C bond from H_2CO with the presence of Fe/Ni sulfides and H_2S at ambient conditions (25 and 70 °C) in aqueous solutions for a period of about one month.

This result is interesting since the conditions addressed in this experimentation are similar to those ambient temperatures in the Earth environment. It has been suggested that a hot ancient seawater at 70 °C existed 3,500 million years ago and it changed to 20 °C 800 million years ago (Robert and Chaussidon 2006). H_2CO is also detected in the contemporary sea water system (Largiuni et al. 2005). It is therefore interesting to investigate this temperature range of the early Earth ambient environment where the reaction kinetics may overlap.

On the other hand, the origin-of-life theory in the iron-sulfur world is set at the hydrothermal vent at the deep ocean where the temperature could be as high as 403 °C (Vondamm et al. 1995) and with a depth of 3000 m in water. The high temperature (Huber and Wächtershauser 2006; Kaschke et al. 1994) and pressure (Cody et al. 2000) is proven to be positive for the yields of some organic products (See Table 8.2). So it would be also interesting to test the formaldehyde theory in the high temperature and pressure conditions, although experiments under these conditions have not been addressed in the thesis project.

In Table 8.2, a number of attempts of hydrothermal organosynthesis in the presence of transition metal compounds are summarized. Many of them (e.g. Huber and Wächtershauser 1997, 1998, 2006) used Fe/Ni sulfides prepared in the similar way as I prepared the NiS precipitates which was characterized in Chapter 3 to 5 and was used in the H₂CO experiments (Chapter 6). Among many successful organosynthesis demonstrated, negative results were also reported. For example, Keefe et al. (1995) did not detect any amino acid, purine or pyrimidine from carbon dioxide with presence of FeS at 100 °C for 122 days. The problem with hydrothermal syntheses is that although the initial yields may be significant, complex organics tend to have limited stability at high temperature.

During the course of my investigations of the H₂CO reactions, several advanced C-C compounds such as C₈H₁₆O₂ and C₁₆H₂₀O and a series of alkenes showed up a few times but failed to turn up again when the experiments were repeated. The appearance of these compounds cannot correlate to the experimental conditions such as the presence of catalyst, temperature and reaction time, which should be crucial for the organic synthesis. So I think they are contaminants. However in Feng et al. (2008), compounds such as C₈H₁₆O₂ were reported as the condensation products from H₂CO reactions under hydrothermal conditions. The repeatability of the experiments shown in Table 8.2 is unknown. It is very important to carefully eliminate contamination during organic syntheses.

Table 8.2 A summary of hydrothermal prebiotic syntheses in the presence of transition metal compounds.

Starting materials	Involved transition metal catalysts	pH	Conditions	Products	References
Nonyl thiol, formic acid	NiAs-type FeS (by elemental reaction) Particle size: 13.8 μm	-	250 °C, 50 – 200 mPa, 6 hrs	Organometallic compounds and pyruvic acid	Cody et al. (2000)
Formic acid, CO, H ₂ , H ₂ O, methylacrylic/itaconic acid	NiS (by elemental reaction)	-	250 °C, 200 mPa, 6 hrs	Carboxylated products	Cody et al. (2001)
Citric acid, H ₂ O	FeS (by elemental reaction)	-	200 °C, 50 – 200 mPa, 2 hrs	Hydroxyisobutyric, methylsuccinic and hydroaconitric acids	
CO, CH ₃ SH	NiS (by Na ₂ S + NiSO ₄)	< 2 or > 8	100 °C, 7 days	Acetic acid	Huber and Wächtershauser (1997)
CO, CH ₃ SH	Ni(OH) ₂	ca. 8		Acetic acid	
CO, CH ₃ SH	FeS+NiS (by Na ₂ S + metal salts)	6.5		Acetic acid	
CO, CH ₃ SH	NiS or FeS+NiS (by Na ₂ S + metal salts)	7		Methane	
CO, CH ₃ SH	NiS+CoS (by Na ₂ S + metal salts)	7.4		Acetic acid	
CO, CH ₃ SH	Nickel sulfate or FeS or CoS	-		Inactive	

CO, H ₂ S (or CH ₃ SH), amino acids	FeS+CoS (by Na ₂ S + metal salts)	alkaline	100 °C, 1-14 days	Short peptides	Huber and Wächtershauser (1998)
Dipeptide Phe-Phe	NiS 50%, FeS 50% (by Na ₂ S + metal salts)	9.8	100 °C, 40 hrs, 75 bar Co pressure	Degradation to α-amino acids	Huber et al. (2003)
CO, KCN, CH ₃ SNa,	Ni or Ni/Fe precipitates	> 12	80-120 °C,	α-hydroxy and α-amino acids	Huber and Wächtershauser (2006)
H ₂ S, nitrate, H ₂ O	FeS (99.99% pyrrhotite, Johnson Matthey)	4	3 days	NH ₃	Bloch et al. (1992)
Ethyne, acetaldehyde, mercapto compounds	FeS (Na ₂ S + FeSO ₄), filter, wash and dry	6	70 °C	Ethene	
Thioglycolic acid	FeS (99.99% pyrrhotite, Johnson Matthey)		160-250 °C, 4 weeks	Acetic acid	
Phenylpyruvate	FeS (Na ₂ S + FeSO ₄), filter, wash and dry		12 days	Cinnamate, phenylpropionate	
Amino acid, H ₂ S, mercaptoacetic acid	FeS (FeSO ₄ + Na ₂ S), filter, wash and dry	4.5	200 kPa, 100 °C, 2-4 days	Amide bonds	Keller et al. (1994)
Cyclohexanone, H ₂ S,	FeS (FeCl ₂ + H ₂ S		In methanol or DMF at 25 °C	cyclohexanethiol and dicyclohexydisulphide	Kaschke et al. (1994)

CO ₂ , H ₂ S/HCl	FeS (99.9%, Aldrich and Johnson Matthey)	3-4	or 100 °C 90 °C, around 5 days	H ₂ , thiols, CS ₂ and dimethyldisulfide	Heinen and Lauwers (1996)
COS, amino acids	Metal ions precipitated by COS	8.2-9.8	25 °C, 5 min to 32 hrs	Dipeptide and tripeptide	Leman et al. (2004)
CO ₂ , H ₂ , KCN, HCHO, NaHS, (HCl)	Pyrite, pyrrhotite, magnetite / illite	8.8	150 - 240 °C, 7 - 54 hrs	A series of amino acids	Hennet et al. (1992)
NH ₃ , CO ₂ , H ₂ S	FeS (1. FeSO ₄ + Na ₂ S; 2. Aldrich product treated at 560 °C. 3. Aldrich product without treatment)		100 °C, 122 days	No ammonia acid, purines, pyrimidines,	Keefe et al. (1995)
HCHO, H ₂ O	Fe powder (FCC phase, 10 - 20 μm)	5	120 °C, 9 days	Formic acid, acetic acid, propionic acid, methyl acetate, propyl propionate and propyl isobutyrate.	Feng et al. (2008)

8.2.2 Trithiane prebiotic reaction

Rickard et al. (2001) discovered that aldehydic carbonyl suppressed pyrite formation from the reaction between FeS and H₂S and greigite is hence resulted. Aldehydic carbonyls are thought to suppress the formation of the key aqueous FeS cluster intermediaries in pyrite formation, possibly through the development of carbonyl adducts. In Chapter 6, I reported that trithiane, the main product of the reaction between H₂CO and H₂S, has a similar function in promoting greigite formation in the system of FeS and H₂S. Trithiane is free of aldehydic carbonyl groups and the presence of H₂S in the reaction vessel discouraged the formation of aldehyde from trithiane in the system. Trithiane may have a similar role in suppressing aqueous FeS cluster formation.

A consequence of this experimentation is that C-S compounds may serve as another reason for greigite formation in sedimentary systems. The formation and preservation of greigite, which is metastable with respect to pyrite, in especially lacustrine environments and within microorganisms has remained a problem. The role of organic reactions in this process may be critical. Thus C-S compounds as well as aldehydic carbonyls, which are abundant in reduced sulfidic sediments, may play a key role in this process. Due to the structural analogy between greigite and the active centre of some enzymes and the basic component of ferredoxin proteins, the result provides additional information regarding the origin-of-life theory in the iron-sulfur world. In the formaldehyde world, for example, trithiane should be present in significant concentrations in sulfidic systems. The presence of such compounds will facilitate the formation and preservation of greigite rather than permitting the development of the extremely stable, end-member, pyrite.

8.3 Catalytic hydrogen evolution

In addition to the heterochemical reactions that may have led to the origin of life described in the previous reaction, the homogeneous cluster reactions should not be neglected – these may have played an equally important role as the heterochemical reactions, and may have been even more important in the oceanic environment.

Chapter 7 reports a novel catalytic hydrogen evolution by the nickel-cysteine cluster in sea water electrochemically. The overpotential for hydronium reduction is lowered by the

presence of nickel-cysteine complex to -1.53 V under ambient conditions. This phenomenon bridges the nickel-cysteine core functioning in hydrogenase enzymes with the abiotic nickel-cysteine complex in the natural aqueous environments, and thus supports the abiogenetic theory of origin of life from transition metal sulfur species in the ocean (Corliss et al. 1979; Russell and Hall 2006; Wächtershauser 2007).

Fe is another transition metal that is close to Ni and is more common in the Earth surface environments. However, catalytic hydrogen evolution is not observed for Fe-cysteine complexes. This is in accordance with the previous observations that this type of reactions were only found to happen with metals Ni and Co.

Titrations between nickel and cysteine revealed that the nickel monocomplex with cysteine is mainly formed in both titration directions. Evidence was also found for the formation of multinuclear nickel cysteine complexes. However, the characterization of the multinuclear nickel cysteine complex requires studies by other techniques. Mass spectrometry may be a good option for examining the stoichiometries of the multinuclear complexes.

Preliminary titrations between Fe and cysteine suggest that when Fe(II) is added into cysteine solution, Fe(cysteine)₃ complex was formed while when cysteine was added into Fe(II) solution, Fe(cysteine)₂ complex was formed. However, these experimental results need repeating to be confirmed.

8.4 List of conclusions

1. Nickel sulfide precipitates are hydrated and nanocrystalline. The nanoparticles may be modelled as a 4 nm nanosphere with a dehydrated NiS (millerite) crystalline core about 1 nm in size, surrounded by an outer layer which contains water species and exhibits considerate disorder. It is a fairly robust metastable configuration under ambient conditions. The material can be formulated as NiS·xH₂O, where x approximates to 1.5 and decreases on heating.
2. The hydrated NiS (millerite) nanoparticles transform to Ni₃S₄ (polydymite) in over time under standard conditions. This transformation is accompanied by Ni₃S₂ (heazlewoodite) formation and more readily to occur for materials precipitated in acidic conditions (i.e.,

pH 3). This transformation may be facilitated by hydrogen bonding and polar water contained in the mantle phase of the material.

3. No catalytic effect was observed for iron and nickel sulfides on catalysing carbon fixation from H_2CO and H_2S under ambient conditions over a period of about one month.
4. Trithiane, in addition to aldehydic carbonyl, also suppresses the pyrite formation and thus promotes greigite formation from the reaction between FeS and H_2S at 70°C .
5. A Ni-cysteine complex catalyses the hydrogen evolution in sea water electrochemically at -1.53 V under ambient conditions.
6. A Ni mono-cysteine complex is mainly formed during the course of titrations between Ni(II) and cysteine. Evidence of the formation of the multinuclear complexes of nickel and cysteine is also observed.

8.5 Future work

1. Raman spectroscopic experiments will help determine the status of water and hydroxyl groups in the hydrated nanoparticulate NiS materials. A Raman spectroscopic investigation has been initiated with K.D.M. Harris (Cardiff) and F. Guillaume (Bordeaux). A paper on the preliminary results on bulk millerite has been recently accepted (Guillaume et al. 2008). The studies of the nanoparticulate NiS are in progress. This may verify and improve the proposed core-mantle structural model for this material.
2. Further information on the nature of the NiS nanoparticles may be obtained through XPS analyses. A preliminary XPS analysis of nanoparticulate NiS (with D. Morgan and A. Carley, Cardiff) showed that the method works with these nanoparticles. The surface composition of the nanoparticles is accessible and it is possible to discriminate oxygen in oxide and hydroxide configurations. The results would provide important information on the nature of the mantle part of the nanoparticles.

3. Mass spectrometer experiments may be used to examine the multinuclear complexes of nickel and cysteine. The number of nickel and cysteine in the $\text{Ni}_{(n)}\text{Cysteine}_{(m)}$ molecules formed in solutions when $[\text{Ni}] \neq [\text{cysteine}]$ can be determined.
4. It would be interesting to investigate further whether Ni-S complex can catalyse the hydrogen evolution in sea water or how much it lowers the overpotential for the reduction of hydronium since bisulfide is supposed to be more commonly existed and more basic than cysteine to perform abiotic synthesis in the prebiotic hydrothermal environments. Molecular hydrogen formation in these environments is of interest both geochemically and in terms of microbiological metabolism in sedimentary systems and as a possible nutrient source for the deep Earth biosphere (Pace 1997).
5. The actual shape of the NiS nanoparticles has not been determined in this study. A SAX-WAX study with T. Wess (Cardiff) provided interesting preliminary results but these were limited by problems of discriminating individual nanoparticles and aggregates. The problem may be got around by acquiring more information from HRTEM. To do this, sufficient number of nanoparticles would need to be examined in different orientations.
6. It would be interesting to test the prebiotic H_2CO reactions with iron and nickel sulfides under high temperature and pressure which more closely mimics oceanic hydrothermal environments. Previous experiments show that the high temperature and pressure conditions enhance carbon fixation reactions. The approach of Feng et al. (2008) needs to be extended both for the effects of NiS catalysts and also to investigate the yields with decreasing temperature under contaminant-free conditions. It would be interesting to check the effects of simple organics on the properties of the precipitated nanoparticulate NiS in terms of the structure, particle size and surface characteristics. NiS precipitates formed in oceanic hydrothermal environments may have been influenced by the presence of simple organic molecules and show different catalytic properties in organosynthetic reactions. ^1H NMR studies of the products of the NiS catalysed organic reactions were attempted during this investigation but sufficient data are needed to better interpret the results. The method is very sensitive. ^1H and with ^{13}C NMR spectroscopy could be usefully employed to search for evidence for the development of C-C bonding in the H_2CO reaction at low temperatures. This has been described as the “Holy Grail” of organic syntheses in this context.

References

- Al-Farawati, R. and van den Berg, C. M. G. 1999. Metal-sulfide complexation in seawater. *Marine Chemistry* **63**:331-352.
- Alsen, N. 1925. Roentgenographische Untersuchungen der Kristallstrukturen von Magnetkies, Breithauptit, Pentlandit, Millerit und verwandten Verbindungen. *Geologiska Foereningens i Stockholm Foerhandlingar* **47**:19-73.
- An, C., Zhang, Z., Chen, X. and Liu, Y. 2006. Selective synthesis of Ni₃S₄ nanocrystallites with hollow structures through a solution-phase approach. *Materials Letters* **60**:3631-3634.
- Anbar, A. D. and Knoll, A. H. 2002. Proterozoic ocean chemistry and evolution: a bioinorganic bridge? *Science* **297**:1137-1142.
- Arita, M. 2006. Thermodynamics of the solid Ni-S system. *Metallurgical and Materials Transactions A-Physical Metallurgy and Materials Science* **37A**:3009-3022.
- Arnold, R. and Kullerud, G. 1956. The NiS-NiS₂ join. *Carnegie Institution Washington Year Book* **55**:178-179.
- Banica, F. G. 1991. Catalytic hydrogen evolution on the mercury electrode in the presence of nickel aminothiols complexes a tentative model process of hydrogenase-catalysed hydrogen bioproduction. *Bulletin de la Societe Chimique de France* **128**:697-703.
- Banica, F. G. and Calusaru, A. 1983. Catalytic prewaves of hydrogen and nickel in cysteine-containing acetate buffer. *Journal of Electroanalytical Chemistry* **145**:389-405.
- Banica, F. G. and Ion, A. 2000. Electrochemical investigations of the nickel(II)-penicillamine system. 3. A study of the catalytic hydrogen prewave in connection with structure of nickel(II)-penicillamine complexes. *Collection of Czechoslovak Chemical Communications* **65**:995-1013.
- Banica, F. G., Moreira, J. C. and Fogg, A. G. 1994. Application of catalytic stripping voltammetry for the determination of organic sulfur-compounds at a hanging mercury drop electrode - behavior of cysteine, cystine and N-acetylcysteine in the presence of nickel ion. *Analyst* **119**:309-318.
- Banica, F. G., Spataru, N. and Spataru, T. 1997. Catalytic hydrogen evolution in the presence of sulfide and cobalt ions. A study by cathodic stripping voltammetry on the hanging mercury drop electrode. *Electroanalysis* **9**:1341-1347.
- Barthelmy, E., Gorochoy, O. and McKenzie, H. 1973. The electrical and magnetic properties of the transition in nickel sulfide. *Materials Research Bulletin* **1973**:1401-1412.
- Bernal, J. D. 1949. The physical basis of life. *Proceedings of the Physical Society* **62**:597-618.

- Berthon, G. 1995. Critical evaluation of the stability-constants of metal-complexes of amino-acids with polar side-chains. *Pure and Applied Chemistry* **67**:1117-1240.
- Bezverkhyy, I., Danot, M. and Afanasiev, P. 2003. New low-temperature preparations of some simple and mixed Co and Ni dispersed sulfides and their chemical behavior in reducing atmosphere. *Inorganic Chemistry* **2003**:1764-1768.
- Biltz, V. 1936. Uber das System Nickelmonosulfid/Nickeldisulfid/Schwefel. *Zeitschrift fur anorganische und allgemeine chemie* **228**:275 - 296.
- Bishop, D. W., Thomas, P. S. and Ray, A. S. 1999. α - β phase re-transformation kinetics in nickel sulphide. *Journal of Thermal Analysis and Calorimetry* **56**:429-435.
- Bjorling, G. and Mulak, W. 1976. Kinetics of NiS leaching in nitric acid solution. *Transactions of the Institution of Mining and Metallurgy Section C* **85**:98-101.
- Black, S., Jefferson, D. and Henderson, P. 1984. An electron-optical study of nickel monosulfide. *Journal of Solid State Chemistry* **53**:76-86.
- Bloch, E., Keller, M., Wächtershauser, G. and Stetter, K. 1992. Reactions depending on iron sulfide and linking geochemistry with biochemistry. *Proceedings of the National Academy of Sciences* **89**:8117-8120.
- Borisenko, D., Dubinov, A., Kolesnikov, N., Kudasov, Y., Kulakov, M. and Shalynin, A. 2003. Composition, unit cell parameters, and Tc in hexagonal NiS. *Journal of Crystal Growth* **253**:307-313.
- Bortnikov, N. S. and Vikent'ev, I. V. 2005. Modern base metal sulfide mineral formation in the world ocean. *Geology of Ore Deposits* **47**:13-44.
- Brdicka, R. 1933. Polarographic studies with the dropping mercury cathode. - part XXXII. - activation of hydrogen in sulphhydryl group of some thio-acids in cobalt salt solutions. *Collection of Czechoslovak Chemical Communications* **5**:148-165.
- Brdicka, R., Brezina, M. and Kalous, V. 1965. Polarography of proteins and its analytical aspects. *Talanta* **12**:1149-1162.
- Bruland, K. W. and Lohan, M. C. 2004. Controls of trace metals in seawater. In: Elderfield, H. ed. *Treatise of Geochemistry*. Vol. 6. Elsevier. pp. 625:23-47.
- Cairns-Smith, A. G. 1982. *Genetic takeover and the mineral origins of life*. Cambridge, England: Cambridge University Press. pp. 477.
- Calusaru, A. and Voicu, V. 1973. Catalytic hydrogen prewave in presence of seleno-cystine and nickel. *Journal of Electroanalytical Chemistry* **43**:257-266.
- Campaigne, E. 1946. Thiones and thials. *Chemical Reviews* **39**:1-76.
- Carney, J. and Laitinen, H. 1970. Electrochemical study of exchange reactions of mercuric sulfide monolayers. *Analytical Chemistry* **42**:473-478.

- Chadwell, S. J., Rickard, D. and Luther, G. W. 1999. Electrochemical evidence for pentasulfide complexes with Mn^{2+} , Fe^{2+} , Co^{2+} , Ni^{2+} , Cu^{2+} and Zn^{2+} . *Aquatic Geochemistry* **5**:29-57.
- Chen, D., Gao, L. and Zhang, P. 2003. Synthesis of nickel sulfide via hydrothermal microemulsion process: nanosheet to nanoneedle. *Chemistry Letters* **32**:996-997.
- Chen, D. L. and Gao, L. 2004. Preparation of low-dimensional nickel sulfide nanocrystals via microemulsion-assisted hydrothermal method. *Chemical Journal of Chinese Universities* **25**:1407-1412.
- Chen, N., Zhang, W. Q., Yu, W. C. and Qian, Y. T. 2002. Synthesis of nanocrystalline NiS with different morphologies. *Materials Letters* **55**:230-233.
- Cleaves, H. J., Chalmers, J. H., Lazcano, A., Miller, S. L. and Bada, J. L. 2008. A reassessment of prebiotic organic synthesis in neutral planetary atmospheres. *Origins of Life and Evolution of Biospheres* **38**:105-115.
- Cody, G. 2004. Transition metal sulfides and the origins of metabolism. *Annual Review of Earth and Planetary Sciences* **32**:569-599.
- Cody, G., Bocter, N., Brandes, J. A., Filley, T., Hazen, R. and Yoder, H. 2004. Assaying the catalytic potential of transition metal sulfides from abiotic carbon fixation. *Geochimica et Cosmochimica Acta* **68**:2185-2196.
- Cody, G. D., Boctor, N. Z., Filley, T. R., Hazen, R. M., Scott, J. H., Sharma, A. and Yoder, H. S. 2000. Primordial carbonylated iron-sulfur compounds and the synthesis of pyruvate. *Science* **289**:1337-1340.
- Cody, G. D., Boctor, N. Z., Hazen, R. M., Brandes, J. A., Morowitz, H. J. and Yoder, H. S. 2001. Geochemical roots of autotrophic carbon fixation: hydrothermal experiments in the system citric acid, H_2O -(+/-FeS)-(+/-NiS). *Geochimica et Cosmochimica Acta* **65**:3557-3576.
- Collin, G. and Chavant, C. 1983. Structure and planar faults in the defective NiAs-type compound $\text{Ni}_{17}\text{S}_{18}$. *Acta Crystallographica B* **39**:289-296.
- Cooper, D. C. and Morse, J. W. 1998. Extractability of metal sulfide minerals in acidic solutions: Application to environmental studies of trace metal contamination within anoxic sediments. *Environmental Science and Technology* **32**:1076-1078.
- Corliss, J. B., Dymond, J., Gordon, L. I., Edmond, J. M., Herzen, R. P. V., Ballard, R. D., Green, K., Williams, D., Bainbridge, A., Crane, K. and Vanandel, T. H. 1979. Submarine thermal springs on the Galapagos rift. *Science* **203**:1073-1083.
- Cotton, F., Wilkinson, G., Murillo, C. and Bochman, M. 1999. *Advanced Inorganic Chemistry*. 6th ed. John Wiley. pp. 1376
- Coucovanis, D., Patil, P. R., Kanatzidis, M. G., Detering, B. and Baenziger, N. C. 1985. Synthesis and reactions of binary metal sulfides. Structural characterization of the $[(\text{S}_4)_2\text{Zn}]^{2-}$, $[(\text{S}_4)_2\text{Ni}]^{2-}$, $[(\text{S}_5)\text{Mn}(\text{S}_6)]^{2-}$, and $[(\text{CS}_4)_2\text{Ni}]^{2-}$ anions. *Inorganic Chemistry* **24**:24-31.

- Cowley, J. M. 2004. Applications of electron nanodiffraction. *Micron* **35**:345-360.
- Coyle, C. L. and Stiefel, E. I. 1988. The coordination chemistry of nickel: an introductory survey. In: Lancaster, J.R. ed. *The Bioinorganic Chemistry of Nickel*. VCH Publishers. pp. 337:1-28.
- Davison, W., Phillips, N. and Tabner, B. 1999. Soluble iron sulfide species in natural waters: reappraisal of their stoichiometry and stability constants. *Aquatic Sciences* **61**:23-43.
- de Jong, W. F. and Willems, H. W. V. 1927. Existenz und Struktur der Disulfide NiS₂ und CoS₂. *Zeitschrift fuer Anorganische und Allgemeine Chemie* **560160**:185-189.
- Deduve, C. and Miller, S. L. 1991. 2-dimensional life. *Proceedings of the National Academy of Sciences of the United States of America* **88**:10014-10017.
- Donges, E. 1947. Saureloslichkeit von gefalltem Kobalt- und Nickelsulfid. *Zeitschrift fur Anorganische und Allgemeine Chemie* **253**:345-351.
- Dyrssen, D. and Kremling, K. 1990. Increasing hydrogen sulfide concentration and trace metal behavior in the anoxic Baltic waters. *Marine Chemistry* **30**:193-204.
- Egami, T. and Billinge, S. J. L. 2003. *Underneath The Bragg Peaks: Structural Analysis of Complex Materials*. Cambridge: Pergamon. pp. 404.
- Elliott, N. 1960. Interatomic distances in FeS₂, CoS₂ and NiS₂. *Journal of Physics and Chemistry of Solids* **33**:903-905.
- Emerson, S., Jacobs, L. and Tebo, B. 1983. The behavior of trace metals in marine anoxic waters: solubilities at the oxygen-hydrogen sulfide interface In: Wong, E. and Boyle, K. and Bruland, K. and Burton, J. and Goldberg, G. eds. *Trace Metals in Sea Water*. 1 ed. New York: Plenum Press. pp. 920.
- Farrow, C., Juhas, P., Liu, J., Bryndin, D., Bozin, E., Bloch, J., Proffen, T. and Billinge, S. 2007a. PDFfit2 and PDFgui: Computer programs for studying nanostructure in crystals. *Journal of Physics: Condensed Matter* **19**:335219-335226.
- Farrow, C. L., Juhas, P., Liu, J. W., Bryndin, D., Bozin, E. S., Bloch, J., Proffen, T. and Billinge, S. J. L. 2007b. PDFgui user guide 1.0 Beta. 29
- Feng, S. H., Tian, G., He, C., Yuan, H. M., Mu, Y., Wang, Y. W. and Wang, L. 2008. Hydrothermal biochemistry: from formaldehyde to oligopeptides. *Journal of Materials Science* **43**:2418-2425.
- Fernandez, A., M, Nair, M., T, S and Nair, P., K 1993. Chemically deposited ZnS-NiS-CuS optical filters with wide range solar control characteristics. *Materials and Manufacture Processing* **8**:535-548.
- Ferris, F. G., Fyfe, W. S. and Beveridge, T. J. 1987. Bacteria as nucleation sites for authigenic minerals in a metal-contaminated lake sediment. *Chemical Geology* **63**:225-232.

- Ferris, J. P. 2006. Montmorillonite-catalysed formation of RNA oligomers: the possible role of catalysis in the origins of life. *Philosophical Transactions of the Royal Society B - Biological Sciences* **361**:1777-1786.
- Fleet, M. 1987. Structure of godlevskite, Ni₉S₈. *Acta Crystallographica Section C: Crystal Structure Communications* **43**:2255-2257.
- Fleet, M. 1988. Stoichiometry, structure and twinning of godlevskite and synthetic low-temperature Ni-excess nickel sulfide. *Canadian Mineralogist* **26**:283-291.
- Fleet, M. E. 1977. The crystal structure of heazlewoodite, and metallic bonds in sulfide minerals. *American Mineralogist* **62**:341-345.
- Fletcher, D. A., McMeeking, R. F. and Parkin, D. 1996. The United Kingdom Chemical Database Service. *Journal of Chemical Information and Computer Sciences* **36**:746-749.
- Frausto da Silva, J. J. R. and Williams, R. J. P. 1991. *The Biological Chemistry of the Elements. The Inorganic Chemistry of Life*. Oxford: Oxford University Press. pp. 561.
- Frey, M. 2002. Hydrogenases: hydrogen-activating enzymes. *Chembiochem* **3**:153-160.
- Fujii, T., Tanaka, K., Marumo, F. and Noda, Y. 1987. Structural behaviour of NiS₂ up to 54 Kbar. *Mineralogical Journal* **13**:448-454.
- Fukuta, T., Ito, T., Sawada, K., Kojima, Y., Matsuda, H. and Yagishita, K. 2003. Improvement of nickel-precipitation from aqueous nickel solution by sulfuration with sodium sulfides. *Journal of Chemical Engineering of Japan* **36**:493-498.
- Furuseth, S. and Kjekshus, A. 1969. On the magnetic properties of CoSe₂, NiS₂, and NiSe₂. *Acta Chemica Scandinavica* **23**:2325-2334.
- Gamsjager, H., Bugajski, J., Gajda, T., Lemire, R. J. and Preis, W. 2005. Chemical Thermodynamics of Nickel. In: Mompean, F.J. ed. *Chemical Thermodynamics Series*. Vol. 6. Elsevier. pp. 648.
- Genin, J. S. and Ibers, J. A. 1998. Solid state transition metal sulphides - some aspects of structure and physical properties. In: Weber, T., Prins, R. and Santen, R.A. eds. *Transition Metal Sulphides: Chemistry and Catalysis*. Vol. 60. Kluwer Academic Publishers. pp. 355:1-35.
- Ghali, E. L. and Girard, B. 1978. La Lixiviation de concentrés de sulfures de nickel par le chlorure ferrique. *Hydrometallurgy* **3**:355-371.
- Ghezelbash, A. and Korgel, B. A. 2005. Nickel sulfide and copper sulfide nanocrystal synthesis and polymorphism. *Langmuir* **21**:9451-9456.
- Gibbs, G. V., Downs, R. T., Prewitt, C. T., Rosso, K. M., Ross, N. L. and Cox, D. F. 2005. Electron density distributions calculated for the nickel sulfides millerite, vaesite, and heazlewoodite and nickel metal: a case for the importance of Ni-Ni bond paths for electron transport. *Journal of Physical Chemistry B* **109**:21788-21795.

- Goh, S., Buckley, A., Lamb, R., Skinner, W., Pring, A., Wang, H., Fan, L.-J., Jang, L.-Y., Lai, L.-J. and Yang, Y.-w. 2006. Sulfur electronic environments in α -NiS and β -NiS: examination of the relationship between coordination number and core electron binding energies. *Physics and Chemistry of Minerals* **33**:98-105.
- Grice, J. D. and Ferguson, R. B. 1974. Crystal structure refinement of millerite (β -NiS). *The Canadian Mineralogist* **12**:248-252.
- Grønvold, F. and Stolen, S. 1995. Heat capacity and thermodynamic properties of millerite from 298.15 to 660 K and NiAs-type nickel(II) sulfide from 260 to 1000 K. thermodynamics of the NiAs-type to millerite transition. *Thermochimica Acta* **266**:213-229.
- Guillaume, F., Huang, S., Harris, K. D. M., Couzi, M. and Talaga, D. 2008. Optical phonons in millerite (NiS) from single-crystal polarized Raman spectroscopy. *Journal of Raman Spectroscopy* (in the press).
- Haldane, J. B. S. 1929. The origin of life. *Rationalist Annual* **3**:148-153.
- Hatton, B. 2007. *The emergence of nucleic acids in an iron sulphur world*. Cardiff University.
- Heinen, W. and Lauwers, A. M. 1996. Organic sulfur compounds resulting from the interaction of iron sulfide, hydrogen sulfide and carbon dioxide in an anaerobic aqueous environment. *Origins of Life and Evolution of the Biosphere* **26**:131-150.
- Hennet, R. J. C., Holm, N. G. and Engel, M. H. 1992. Abiotic synthesis of amino-acids under hydrothermal conditions and the origin of life - a perpetual phenomenon. *Naturwissenschaften* **79**:361-365.
- Horiuchi, S. 1971. Electron beam heating transformation of mackinawite (FeS) to greigite (Fe₃S₄). *Zeitschrift für Anorganische und Allgemeine Chemie* **386**:196-200.
- Hu, Y., Chen, J. F., Chen, W. M., Lin, X. H. and Li, X. L. 2003. Synthesis of novel nickel sulfide submicrometer hollow spheres. *Advanced Materials* **15**:726-729.
- Huang, S., Ohfuji, H., Lammie, D., Wess, T., Bell, A. M. T., Vaughan, D., Oldroyd, A. and Rickard, D. 2006. Nanoparticulate nickel sulfides formed in low temperature aqueous solutions. *Geochimica et Cosmochimica Acta* **70**:A271.
- Huber, C., Eisenreich, W., Hecht, S. and Wächtershauser, G. 2003. A possible primordial peptide cycle. *Science* **301**:938-940.
- Huber, C. and Wächtershauser, G. 1997. Activated acetic acid by carbon fixation on (Fe,Ni)S under primordial conditions. *Science* **276**:245-247.
- Huber, C. and Wächtershauser, G. 1998. Peptides by activation of amino acids with CO on (Fe, Ni)S surfaces: implications for the origin of life. *Science* **281**:670-672.
- Huber, C. and Wächtershauser, G. 2006. α -hydroxy and α -amino acids under possible Hadean, volcanic origin-of-life conditions. *Science* **314**:630-632.

- Hubli, R. C., Mukherjee, T. K., Venkatachalam, S., Bautista, R. G. and Gupta, C. K. 1995. Kinetics of millerite dissolution in cupric chloride solutions. *Hydrometallurgy* **38**:149-159.
- Huerta-Diaz, M. A., Tessier, A. and Carignan, R. 1998. Geochemistry of trace metals associated with reduced sulfur in freshwater sediments. *Applied Geochemistry* **13**:213-233.
- Ion, A., Banica, F. G. and Luca, C. 1998. Ligand-catalysed metal ion reduction. Voltammetric determination of rate and formation constants for the nickel complex with 6-mercaptopurine-9-D-riboside. *Journal of Electroanalytical Chemistry* **444**:11-18.
- Jacobs, L. and Emerson, S. 1982. Trace metal solubility in an anoxic fjord. *Earth and Planetary Science Letters* **60**:237-252.
- Jaramillo, A. and Sonnenfeld, G. 1989. Effects of amorphous and crystalline nickel sulfide on induction of interferons- α/β and - γ and interleukin-2. *Environmental Research* **48**:275-286.
- Jeong, Y. U. and Manthiram, A. 2001. Synthesis of nickel sulfides in aqueous solutions using sodium dithionite. *Inorganic Chemistry* **40**:73-77.
- Jiang, X. C., Xie, Y., Lu, J., Zhu, L. Y., He, W. and Qian, Y. T. 2001. Synthesis of novel nickel sulfide layer-rolled structures. *Advanced Materials* **13**:1278-1281.
- Joris, S. 1969. La cinétique de précipitation des sulfures de cobalt et de nickel par l'hydrogène sulfure. *Bulletin des Sociétés Chimiques Belges* **78**:607-619.
- Kaschke, M., Russell, M. J. and Cole, W. J. 1994. [FeS/FeS₂] - a redox system for the origin of life - (some experiments on the pyrite-hypothesis). *Origins of Life and Evolution of the Biosphere* **24**:43-56.
- Keefe, A., Miller, S. L., McDonald, G. and Bada, J. 1995. Investigation of the prebiotic synthesis of amino acids and RNA bases from CO₂ using FeS/H₂S as a reducing agent. *Proceedings of the National Academy of Sciences* **92**:11904-11906.
- Keller, M., Blochl, E., Wächterschauser, G. and Stetter, K. 1994. Formation of amide bonds without a condensation agent and implications for origin of life. *Nature* **368**:836-838.
- Kerr, P. 1945. Cattierite and vaesite: new Co-Ni minerals from the Belgian Congo. *American Mineralogist* **30**:483-497.
- Kesler, Y. A., Smirnov, S. G., Pokholok, K. V. and Viting, B. N. 1991. Peculiarities of the electronic structure of Co, Ni-thiospinel. *Izvestiya Akademii Nauk SSSR, Neorganicheskie Materialy* **27**:977-980.
- Khiew, P. S., Huang, N. M., Radiman, S. and Ahmad, M. S. 2004. Synthesis of NiS nanoparticles using a sugar-ester nonionic water-in-oil microemulsion. *Materials Letters* **58**:762-767.
- Kirkpatrick, W. 1951. Nickel sulfide catalysts. *Advances in Catalysis* **3**:329-339.

- Kolkmeijer, N. H. and Moesveld, A. L. T. 1931. Ueber die Dichte und Struktur des Millerits (rhomboedrischen Nickelsulfids). *Zeitschrift fuer Kristallographie, Kristallgeometrie, Kristallphysik, Kristallchemie* **80**:91-102.
- Kolthoff, I. 1931. The solubilities and solubility products of metallic sulfides in water. *Journal of Physical Chemistry* **35**:2711-2721.
- Kozlowski, H., Decocklereverend, B., Ficheux, D., Loucheux, C. and Sovago, I. 1987. Nickel(II) complexes with sulfhydryl containing peptides - potentiometric and spectroscopic studies. *Journal of Inorganic Biochemistry* **29**:187-197.
- Krishnakumar, S. R., Shanthi, N. and Sarma, D. D. 2002. Electronic structure of millerite NiS. *Physical Review B* **66**:115105.
- Kullerud, G. and Yund, R. A. 1962. The Ni-S System and Related Minerals. *Journal of Petrology* **3**:126-175.
- Lambert, J. F. 2008. Adsorption and polymerization of amino acids on mineral surfaces: A review. *Origins of Life and Evolution of Biospheres* **38**:211-242.
- Lange, B. and van den Berg, C. M. G. 2000. Determination of selenium by catalytic cathodic stripping voltammetry. *Analytica Chimica Acta* **418**:33-42.
- Largiuni, O., Becagli, S., Innocenti, M., Stortini, A. M., Traversi, R. and Udisti, R. 2005. Formaldehyde determination in seawater. Preliminary application to coastal samples at Terra Nova Bay (Antarctica). *Journal of Environmental Monitoring* **7**:1299-1304.
- Larson, A. and Von Dreele, R. 2004. General structure analysis system. Los Alamos National Laboratory Report LAUR 86-748.
- Legrand, D. L., Nesbitt, H. W. and Bancroft, G. M. 1998. X-ray photoelectron spectroscopic study of a pristine millerite (NiS) surface and the effect of air and water oxidation. *American Mineralogist* **83**:1256-1265.
- Leman, L., Orgel, L. E. and Ghadiri, M. 2004. Carbonyl sulfide-mediated prebiotic formation of peptides. *Science* **306**:283-286.
- Lennie, A., Redfern, A., Champness, P., Stoddart, C., Schofield, P. and Vaughan, D. 1997. Transformation of mackinawite to greigite: An in situ X-ray powder diffraction and transmission electron microscope study. *American Mineralogist* **82**:302-309.
- Lennie, A. R., Redfern, S. A. T., Schofield, P. F. and Vaughan, D. J. 1995. Synthesis and rietveld crystal structure refinement of mackinawite, tetragonal FeS. *Mineralogical Magazine* **59**:677-683.
- Levi, D. and Baroni, A. 1935. Struttura de alterazioni di struttura di NiS e di NiSe. *Zeitschrift fuer Kristallographie* **228**:275 - 296.
- Levine, J. S., Augustsson, T. R. and Natarajan, M. 1982. The prebiological paleoatmosphere - stability and composition. *Origins of Life and Evolution of the Biosphere* **12**:245-259.

- Li, H. B., Chai, L. L., Wang, X. Q., Wu, X. Y., Xi, G. C., Liu, Y. K. and Qian, Y. T. 2007. Hydrothermal growth and morphology modification of β -NiS three-dimensional flowerlike architectures. *Crystal Growth & Design* **7**:1918-1922.
- Licht, S. 1988. Aqueous solubilities, solubility products and standard oxidation-reduction potentials of the metal sulfides. *Journal of the Electrochemical Society* **135**:2971-2975.
- Licht, S., Hodes, G., Tenne, R. and Manassen, J. 1987. A light-variation insensitive high efficiency solar cell. *Nature* **326**:863-864.
- Line, G. and Huber, M. 1963. Etude radiocristallographique a haute temperature de la phase non stoechiometrique $\text{Ni}_{3+\chi}\text{S}_2$. *Comptes Rendus Hebdomadaires des Seances de l'Academie des Sciences* **256**:3118-3120.
- Lioutas, C. B., Manolikas, C., Vantendeloo, G. and Vanlanduyt, J. 1993. A 2a2a3c superstructure in hexagonal $\text{Ni}_{1-\chi}\text{S}$ - a study by means of electron-diffraction and HRTEM. *Journal of Crystal Growth* **126**:457-465.
- Lu, Z. W., Klein, B. M. and Singh, D. J. 1996. Electronic structure of heazlewoodite Ni_3S_2 . *Physical Review B* **54**:13542-13545.
- Lundqvist, D. 1947. X-ray studies on the binary system Ni-S. *Arkiv foer Kemi, Mineralogi och Geologi, A* **24**:1-12.
- Luo, Y., Zhang, J. C., Shen, Y., Jiang, S. T. and Liu, G. Y. 2007. Synthesis and characterization of nickel nanorods transferred from hydrotherally decomposed rod-like NiS. *Journal of Materials Science and Technology* **23**:587-590.
- Luther, G. and Rickard, D. 2005. Metal sulfide cluster complexes and their biogeochemical importance in the environment. *Journal of Nanoparticle Research* **7**:389-407.
- Luther, G., Theberge, S. and Rickard, D. 1999. Evidence for aqueous clusters as intermediates during zinc sulfide formation. *Geochimica et Cosmochimica Acta* **63**:3159-3169.
- Luther, G. W., Rickard, D. T., Theberge, S. and Olroyd, A. 1996. Determination of metal (bi)sulfide stability constants of Mn^{2+} , Fe^{2+} , Co^{2+} , Ni^{2+} , Cu^{2+} , and Zn^{2+} by Voltammetric Methods. *Environmental Science and Technology* **30**:671-679.
- Mader, P., Kolthoff, I. M. and Vesel, V. 1982. Catalytic hydrogen activity of the low-molecular weight thiols: kinetic control of the Brdicka catalytic current. *Electrochimica Acta* **27**:1393-1401.
- Makovicky, E. 2006. Crystal structures of sulfides and other chalcogenides. In: Vaughan, D. ed. *Sulfide Mineralogy and Geochemistry*. Reviews in Mineralogy and Geochemistry. Vol. 61. The Mineralogical Society of America. pp. 714:7-125.
- Malm, J. O. and O'Keefe, M. A. 1997. Deceptive "lattice spacings" in high-resolution micrographs of metal nanoparticles. *Ultramicroscopy* **68**:13-23.

- Macrae, C. F., Edgington, P. R., McCabe, P., Pidcock, E., Shields, G. P., Taylor, R., Towler, M. and van De Streek, J. 2006. Mercury: visualization and analysis of crystal structures. *Journal of Applied Crystallography* **39**:453-457.
- McWhan, D. B., Marezio, M., Remeika, J. P. and Dernier, P. D. 1972. Pressure-temperature phase diagram and crystal structure of NiS. *Physical Review, Serie 3. B - Solid State* **5**:2552-2555.
- Mellor, J. W. 1936. Nickel. In: Parkes, G.D. ed. *A comprehensive treatise on inorganic and theoretical chemistry*. 1 ed., Vol. XV. Longmans. pp, 816:1-497.
- Menzer, G. 1926. Über die Kristallstruktur von Linneit, einschließlich Polydymite und Sychnodymit. *Zeitschrift für Kristallographie* **64**:506-507.
- Metcalf, P. A., Crooker, B. C., McElfresh, M., Kakol, Z. and Honig, J. M. 1994. Low-temperature electronic and magnetic properties of single-crystal Ni₃S₂. *Physical Review B* **50**:2055-2060.
- Michel, F. M., Antao, S. M., Chupas, P. J., Lee, P. L., Parise, J. B. and Schoonen, M. A. A. 2005. Short- to medium-range atomic order and crystallite size of the initial FeS precipitate from pair distribution function analysis. *Chemistry of Materials* **17**:6246-6255.
- Miller, S. L. 1953. A production of amino acids under possible primitive Earth conditions. *Science* **117**:528-529.
- Mirceski, V., Skrzypek, S., Ciesielski, W. and Sokolowski, A. 2005. Theoretical and experimental study of the catalytic hydrogen evolution reaction in the presence of an adsorbed catalyst by means of square-wave voltammetry. *Journal of Electroanalytical Chemistry* **585**:97-104.
- Monk, P. M. S. 2001. *Fundamentals of electroanalytical chemistry*. Chichester, New York: Wiley. pp. 361.
- Morooka, S., Wakai, C., Matubayasi, N. and Nakahara, M. 2005. Hydrothermal carbon-carbon bond formation and disproportionations of C1 aldehydes: Formaldehyde and formic acid. *Journal of Physical Chemistry A* **109**:6610-6619.
- Mulak, W. 1983. Kinetics of dissolution of synthetic millerite (β -NiS) in acidic potassium dichromate solutions. *Hydrometallurgy* **11**:79-89.
- Mulak, W. 1985. Kinetics of dissolution of synthetic heazlewoodite (Ni₃S₂) in nitric acid solutions. *Hydrometallurgy* **14**:67-81.
- Mulak, W. 1987a. The catalytic action of cupric and ferric ions in nitric acid leaching of Ni₃S₂. *Hydrometallurgy* **17**:201-214.
- Mulak, W. 1987b. Silver ion catalysis in nitric acid dissolution of Ni₃S₂. *Hydrometallurgy* **18**:195-205.
- Mulak, W., Balaz, P. and Chojnacka, M. 2002. Chemical and morphological changes of millerite by mechanical activation. *International Journal of Mineral Processing* **66**:233-240.

- Mulak, W., Chojnacka, M. and Wawrzak, D. 2001. Mechanism of catalytic action of cupric ions in ferric salts leaching of millerite. *Physicochemical Problems of Mineral Processing* **35**:67-72.
- Nesbitt, H. and Reinke, M. 1999. Properties of As and S at NiAs, NiS and Fe_{1-x}S surfaces, and reactivity of niccolite in air and water. *American Mineralogist* **84**:639-649.
- Nicholls, D. 1973. Nickel. In: Trotman-Dickenson ed. *Comprehensive Inorganic Chemistry*. Vol. 3. Pergamon. Pp. 1387:1109-1161.
- Noda, Y., Ohtomo, S., Igaki, K. and Holser, W. 1979. Defect control of nickel sulfide by heat-treatment in sulfur atmosphere. *Transitions of the Japn Institute of Metals* **20**:89-99.
- Nowack, E., Schwarzenbach, D., Gonschorek, W. and Hahn, T. 1989. Deformationsdichten in CoS₂ und NiS₂ mit Pyritstruktur. *Zeitschrift fuer Kristallographie* **186**:213-215.
- Nowack, E., Schwarzenbach, D. and Hahn, T. 1991. Charge densities in CoS₂ and NiS₂ (pyrite structure). *Acta Crystallographica B* **47**:650-659.
- NTP 1996. *NTP Toxicology and carcinogenesis studies of nickel subsulfide (CAS No. 12035-72-2) in F344 rats and B6C3F1 mice (inhalation studies)*. National Toxicology Program.
- Ohfuji, H. and Rickard, D. 2006. High resolution transmission electron microscopic study of synthetic nanocrystalline mackinawite. *Earth and Planetary Science Letters* **241**:227-233.
- Olivas, A., Cruz-Reyes, J., Avalos, M., Petranovskii, V. and Fuentes, S. 1999. Influence of preparation conditions on formation of crystalline phases of nickel sulfide. *Materials Letters* **38**:141-144.
- Olivas, A., Cruz-Reyes, J., Petranovskii, V., Avalos, M. and Fuentes, S. 1998. Synthesis and characterization of nickel sulfide catalysts. *Journal of Vacuum Science and Technology A* **16**:3515-3520.
- Oparin, A. I. 1953. *The Origin of Life*. New York: Dover. pp. 270.
- Pace, N. R. 1997. A molecularview of microbial diversity and the biosphere. *Science* **276**:734-740.
- Parise, J. 1980. Structure of heazlewoodite (Ni₃S₂). *Acta Crystallographica Section B-Structural Science* **B36**:1179-1180.
- Peacock, M. 1947. On heazlewoodite and artificial compound Ni₃S₂. *University of Toronto Studies, Geological Series* **51**:59-69.
- Pearson, F., Berner, J. and Hummer, W. 1992. *Nagra Thermochemical Database II. Supplemental Data 05/92*. Nagra, Wettingen, Switzerland.
- Perrin, D. and Sayce, I. 1968. Complex formation by nickel and zinc with penicillamine and cysteine. *Journal of the American Chemical Society A- Inorganic Physical Theoretical* **1968**:53-57.

- Pinto, J., Gladstone, G. and Yung, Y. 1980. Photochemical production of formaldehyde in earth's primitive atmosphere. *Science* **210**:183-185.
- Putnis, A. 1976. Observations of transformation behaviour in Ni₇S₆ by transmission electron microscopy. *American Mineralogist* **61**:322-325.
- Rajamani, V. and Prewitt, C., T 1974. The crystal structure of millerite. *The Canadian Mineralogist* **12**:253-257.
- Rajamani, V. and Prewitt, C. T. 1975. Refinement of the structure of Co₉S₈. *Canadian Mineralogist* **13**:75-78.
- Ramesh, T. N., Kamath, P. V. and Shivakumara, C. 2006. Classification of stacking faults and their stepwise elimination during the disorder - order transformation of nickel hydroxide. *Acta Crystallographica Section B-Structural Science* **62**:530-536.
- Raspor, B. 2001. Elucidation of the mechanism of the Brdicka reaction. *Journal of Electroanalytical Chemistry* **503**:159-162.
- Rau, H. 1975. Range of homogeneity and defect interaction in high temperature nickel sulfide Ni_{1-x}S. *Journal of Physics and Chemistry of Solids* **36**:1199-1204.
- Rickard, D. 1969. The chemistry of iron sulfide formation at low temperatures. *Stockholm Contributions in Geology* **20**:67-95.
- Rickard, D. 1995. Kinetics of FeS precipitation: part 1. Competing reaction mechanisms. *Geochimica et Cosmochimica Acta* **59**:4367-4379.
- Rickard, D. 1997. Kinetics of pyrite formation by the H₂S oxidation of iron (II) monosulfide in aqueous solution between 25 and 125 °C: the rate equation. *Geochimica et Cosmochimica Acta* **61**:115-134.
- Rickard, D., Butler, I. B. and Oldroyd, A. 2001. A novel iron sulphide mineral switch and its implications for Earth and planetary science. *Earth and Planetary Science Letters* **189**:85-91.
- Rickard, D., Griffith, A., Oldroyd, A., Butler, I. B., Lopez-Capel, E., Manning, D. A. C. and Apperley, D. C. 2006. The composition of nanoparticulate mackinawite, tetragonal iron(II) monosulfide. *Chemical Geology* **235**:286-298.
- Rickard, D. and Luther, G. 2006. Metal sulfide complexes and clusters. *Sulfide Mineralogy and Geochemistry*. Reviews in Mineralogy and Geochemistry. Vol. 61. The Mineralogical Society of America. pp. 714:421-504.
- Rickard, D. and Luther, G. W. 2007. Chemistry of iron sulfides. *Chemical Reviews* **107**:514-562.
- Rickard, D. and Morse, J. 2005. Acid volatile sulfide. *Marine Chemistry* **97**:141-197.
- Rickard, D., Oldroyd, A. and Cramp, A. 1999. Voltammetric evidence for soluble FeS complexes in anoxic estuarine muds. *Estuaries* **22**:693-701.

Robert, F. and Chaussidon, M. 2006. A palaeotemperature curve for the Precambrian oceans based on silicon isotopes in cherts. *Nature* **443**:969-972.

Robie, R., Hemingway, B. and Fisher, J. 1978. Thermodynamic properties of minerals and related substances at 198.15K and 1 bar (10^5 pascals) pressure and at higher temperatures. *Bulletin of the United States Geological Survey* 1452.

Rosenqvist, T. 1954. A thermodynamic study of the iron, cobalt, and nickel sulphide. *Journal of the Iron and Steel Institute* **176**:37-57.

Russell, M. J. 2003. The importance of being alkaline. *Science* **302**:580-581.

Russell, M. J., Daia, D. E. and Hall, A. J. 1998. The emergence of life from FeS bubbles at alkaline hot spring in an acid ocean. In: Weigel, J. and Adams, M.W. eds. *Thermophiles: The keys to molecular evolution and the origin of life?* London: Taylor and Francis. pp. 346:77-126.

Russell, M. J. and Hall, A. 1997. The emergence of life from iron monosulphide bubbles at a submarine hydrothermal redox and pH front. *Journal of Geological Society* **154**:377-402.

Russell, M. J. and Hall, A. 2006. The onset and early evolution of life. *Geological society of America Memoir* **198**:1-32.

Russell, M. J., Hall, A., Boyce, A. and Fallick, A. 2005. On hydrothermal convection systems and the emergence of life. *Economic Geology* **100**:419-438.

Russell, M. J. and Martin, W. 2004. The rocky roots of the acetyl-CoA pathway. *Trends in Biochemical Sciences* **29**:358-363.

Saito, M. A., Sigman, D. M. and Morel, F. M. M. 2003. The bioinorganic chemistry of the ancient ocean: the co-evolution of cyanobacterial metal requirements and biogeochemical cycles at the Archean-Proterozoic boundary? *Inorganica Chimica Acta* **356**:308-318.

Schoonen, M., Smirnov, A. and Cohn, C. 2004. A perspective on the role of minerals in prebiotic synthesis. *Ambio* **33**:539-551.

Schoonen, M., Xu, Y. and Bebie, J. 1999. Energetics and kinetics of the prebiotic synthesis of simple organic acids and amino acids with the FeS-H₂S/FeS₂ redox couple as reductant. *Origins of Life and Evolution of the Biosphere* **29**:5-32.

Schopf, J. W. 1999. *Cradle of life: the discovery of Earth's earliest fossils*. Princeton: Princeton University Press. pp. 367.

Schulte, M. D. and Shock, E. L. 1993. Aldehydes in hydrothermal solution: Standard partial molal thermodynamic properties and relative stabilities at high temperatures and pressures. *Geochimica et Cosmochimica Acta* **57**:3835-3846.

Seidell, A. 1950. *Solubilities of Inorganic and Metal Organic Compounds: A Compilation of Quantitative Solubility Data from the Periodical Literature*. 3 ed. New York: Von Nostrand. pp. 1698.

- Sillen, L. G. 1965. Oxidation state of Earth's ocean and atmosphere. I. A model calculation on earlier states. Myth of prebiotic soup. *Arkiv For Kemi* **24**:431.
- Smith, R. and Martell, A. 1976. *Critical Stability Constants, Volume 4: Inorganic Complexes*. New York: Plenum Press. pp. 469.
- Sowa, H., Ahsbahr, H. and Schmitz, W. 2004. X-ray diffraction studies of millerite NiS under non-ambient conditions. *Physics and Chemistry of Minerals* **31**:321-327.
- Speight, J. G. 2005. *Lange's Handbook of Chemistry*. New York: McGraw-Hill. pp. 1000.
- Spence, J. C. H. 1988. *Experimental High-Resolution Electron Microscopy*. 2 ed. Oxford University Press. pp. 427.
- Srivasta, S. K., Raju, E. V. and Mathur, H. B. 1973. Thermodynamics of interaction of Ni(II) ion with cysteine. *Journal of Inorganic and Nuclear Chemistry* **35**:253-259.
- Steeds, J. W. and Morniroli, J.-P. 1992. Electron diffraction-SAED & CBED. In: Buseck, P. ed. *Minerals and Reactions at the Atomic Scale: Transmission Electron Microscopy*. Reviews in Mineralogy. Vol. 27. Mineralogical Society of America. pp. 508:37-84.
- Stiefel, E. and Matsumoto, K. 1996. *Transition Metal Sulfur Chemistry: Biological and Industrial Significance*. Washington, DC: American Chemical Society. pp. 358.
- Sun, X. 2003. Microstructure studies on hexagonal layered Ni-S nanocrystals. *Applied Surface Science* **217**:23-27.
- Teixeira, M., Moura, I., Xavier, A. V., Moura, J. J. G., Legall, J., Dervartanian, D. V., Peck, H. D. and Huynh, B. H. 1989. Redox intermediates of desulfovibrio-gigas [Nife] hydrogenase generated under hydrogen - Mössbauer and EPR characterization of the metal centers. *Journal of Biological Chemistry* **264**:16435-16450.
- Thiel, A. and Gessner, H. 1914. Über nickelsulfid und kobaltsulfid. I. Die scheinbare Anomalie im Verhalten des Nickelsulfids gegen. *Zeitschrift für Anorganische Chemie* **86**:1-57.
- Thoenen, T. 1999. Pitfalls in the use of solubility limits for radioactive waste disposal: The case of nickel in sulfidic groundwaters. *Nuclear Technology* **126**:75-87.
- Thomas, J. M. and Midgley, P. A. 2004. High-resolution transmission electron microscopy: The ultimate nanoanalytical technique. *Chemical Communications* **2004**:1253-1267.
- Tomschik, M., Ludek, H., Palecek, E. and Heyrovsky, M. 2000. The presodium catalysis of electroreduction of hydrogen ions on mercury electrodes by metallothionein. An investigation by constant current derivative stripping chronopotentiometry. *Electroanalysis* **12**:274-279.
- Topsoe, H., Clausen, B. and Massoth, F. 1996. *Hydrotreating Catalysis*. Springer. pp. 310.
- Trahan, J., Goodrich, R. G. and Watkins, S. F. 1970. X-ray diffraction measurements on metallic and semiconducting hexagonal NiS. *Physical Review B* **2**:2859-2863.

- Tsen, S. C. Y., Crozier, P. A. and Liu, J. 2003. Lattice measurement and alloy compositions in metal and bimetallic nanoparticles. *Ultramicroscopy* **98**:63-72.
- Usov, V. A., Timokhina, L. V. and Voronkov, M. G. 1990. The synthesis and properties of thioaldehydes. *Russian Chemical Reviews* **54**:378-395.
- van den Berg, C. M. G. 1995. Evidence for organic complexation of iron in seawater. *Marine Chemistry* **50**:139-157.
- Vaughan, D. J. and Craig, J. R. 1985. The crystal chemistry of iron-nickel thiospinels. *American Mineralogist* **70**:1036-1043.
- Voicu, V. and Calusaru, A. 1973. A polarographic study of the pre-sodium type catalytic hydrogen wave exhibited by selenocystine. *Talanta* **20**:659-666.
- Vondamm, K. L., Oosting, S. E., Kozlowski, R., Buttermore, L. G., Colodner, D. C., Edmonds, H. N., Edmond, J. M. and Grebmeier, J. M. 1995. Evolution of east Pacific rise hydrothermal vent fluids following a volcanic-eruption. *Nature* **375**:47-50.
- Vuorelainen, Y., Huhma, A. and Hakli, A. 1964. Sederholmite, wilkmanite, kullerudite, makinenite and trustedtite, five new nickel selenide minerals. *Bulletin de la Commission Géologique de Finlande* **215**:113-126.
- Wächtershauser, G. 1988a. Before enzymes and templates: theory of surface metabolism. *Microbiological Reviews* **52**:452-484.
- Wächtershauser, G. 1988b. Pyrite formation, the first energy source for life: a hypothesis. *Systematic and Applied Microbiology* **10**:207-210.
- Wächtershauser, G. 1990. Evolution of the first metabolic cycles. *Proceedings of the National Academy of Sciences* **87**:200-204.
- Wächtershauser, G. 1991. Biomolecules: the origin of their optical activity. *Medical Hypotheses* **36**:307-311.
- Wächtershauser, G. 1992. Groundworks for an evolutionary biochemistry: the iron-sulphur world. *Progress in Biophysics and Molecular Biology* **58**:58-201.
- Wächtershauser, G. 1993. The cradle chemistry of life: on the origin of natural products in a pyrite-pulled chemoautotrophic origin of life. *Pure and Applied Chemistry* **65**:1343-1348.
- Wächtershauser, G. 2000. Origin of life: life as we don't know it. *Science* **289**:1307-1308.
- Wächtershauser, G. 2007. On the chemistry and evolution of the pioneer organism. *Chemistry & Biodiversity* **4**:584-602.
- Waldner, P. and Pelton, A. D. 2004. Thermodynamic modelling of the Ni-S system. *Zeitschrift Fur Metallkunde* **95**:672-681.
- Wang, H. 2005. Decomposition and phase transition of NiS/Ni_{1-x}S in the temperature range 323-973 K. *Journal of Sulfur Chemistry* **26**:233-243.

- Wang, L., Schultz, M. and Matijevic, E. 1997. Preparation and properties of uniform amorphous and crystalline colloidal nickel sulfide. *Colloid and Polymer Science* **275**:593-598.
- Waychunas, G. A. 2001. Structure, aggregation and characterization of nanoparticles. In: Banfield, J.F. and Navrotsky, A. eds. *Nanoparticles and the Environment*. Reviews in Mineralogy and Geochemistry. Vol.44. Mineralogical Society of America. pp. 349:105-166.
- Will, G., Lauterjung, J., Schmitz, H. and Hinze, E. 1984. The bulk moduli of 3d-transition element pyrites measured with synchrotron radiation in a new belt type apparatus. *Materials Research Society Symposia Proceedings* **22**:49-52.
- Wolthers, M., Gaast, S. and Rickard, D. 2003. The structure of disordered mackinawite. *American Mineralogist* **88**:2007-2015.
- Ycas, M. 1955. A note on the origin of life. *Proceedings of the National Academy of Sciences* **41**:714-716.
- Zehnder, A. and Wuhrmann, K. 1976. Titanium(III) citrate as a nontoxic oxidation-reduction buffering system for the culture of obligate anaerobes. *Science* **194**:1165-1166.
- Zhang, B., Ye, X., Dai, W., Hou, W. and Xie, Y. 2006. Biomolecule-assisted synthesis and electrochemical hydrogen storage of porous spongelike Ni₃S₂ nanostructures grown directly on nickel foils. *Chemistry - A European Journal* **12**:2337-2342.
- Zhang, H., Gilbert, B., Huang, F. and Banfield, J. F. 2003. Water-driven structure transformation in nanoparticles at room temperature. *Nature* **424**:1025-1029.
- Zhang, J. Z. and Millero, F. J. 1994. Investigation of metal sulfide complexes in sea water using cathodic stripping square wave voltammetry. *Analytica Chimica Acta* **284**:497-504.
- Zhang, X. M., Wang, C., Xie, Y. and Qian, Y. T. 1999. Preparation and characterization of nanocrystalline nickel monosulfide(h) via the ethanol-thermal reducing process. *Materials Research Bulletin* **34**:1967-1972.
- Zhang, Y. H., Guo, L., He, L., Liu, K., Chen, C. P., Zhang, Q. and Wu, Z. Y. 2007. Controlled synthesis of high-quality nickel sulfide chain-like tubes and echinus-like nanostructures by a solution chemical route. *Nanotechnology* **18**:1-8.
- Zubay, G. 1996. Studies on the lead-catalysed synthesis of aldopentoses. *Origins of life and evolution of the biosphere* **28**:13-26.
- Zubay, G. 2000. *Origins of Life on the Earth and in the Cosmos*. 2 ed. Academic Press. pp. 564.

